University of Southampton

Faculty of Engineering and Physical Sciences

Institute of Sound and Vibration Research

Control of Biofouling in Water Pipes using Guided Waves

by

Austen Stone

Thesis for the degree of Doctor of Philosophy

September 2024

University of Southampton

Abstract

Faculty of Engineering and Physical Sciences

Institute of Sound and Vibration Research

Doctor of Philosophy

Control of Biofouling in Water Pipes using Guided Waves

Austen Stone

Biofouling of invasive Zebra and Quagga mussels presents an ongoing problem in industries which draw freshwater from infested sources. In particular, many intake pipes used in the water and power industries are now inhabited by rapidly growing mussel colonies, which are well suited to infiltrate and settle on pipe walls. Left untreated, mussel fouling can cause substantial reductions in flow, blockages, and damage to downstream equipment, incurring significant economic costs. Many potential treatments have been considered but as of yet, no consensus has been reached on a comprehensive antifouling strategy. A growing body of research suggests that zebra mussels are sensitive to sound and vibration. Lab experiments have demonstrated the ability to inhibit the settlement of mussels or even induce mortality with high enough sound amplitudes.

This project explores the feasibility of using sound and vibration to control mussel fouling in long-range water pipelines. Specifically, the dispersive properties of guided waves in pipes are utilized to achieve high response amplitudes at targeted locations, with time reversal focusing employed to maximise the response. The work begins by analysing a rigid duct model, neglecting pipe wall dynamics to study the acoustic system in isolation. The effectiveness of time reversal focusing is assessed. Next, the Wave Finite Element method is used to model fluid-structure interaction, with a focus on energy distribution, long-range power transfer, and optimal excitation frequencies.

Finally, a numerical experiment is performed with a model of a commercial inertial actuator coupled to the pipe. Results are compared with the literature on mussel antifouling. The model suggests that inhibitory levels of sound and vibration can be attained at significant distances from the source by using time reversal focussing. To conclude, implications of the work are discussed for the feasibility of mussel antifouling with sound and vibration.

Declaration of Authorship

I, Austen Stone, declare that the thesis entitled *Control of Biofouling in Water Pipes using Guided Waves* and the work presented in it are both my own, and have been generated by me as the result of my own original research. I confirm that:

1. This work was done wholly or mainly while in candidature for a research degree at this University;
2. Where any part of this thesis has previously been submitted for a degree or any other qualification at this University or any other institution, this has been clearly stated;
3. Where I have consulted the published work of others, this is always clearly attributed;
4. Where I have quoted from the work of others, the source is always given. With the exception of such quotations, this thesis is entirely my own work;
5. I have acknowledged all main sources of help;
6. Where the thesis is based on work done by myself jointly with others, I have made clear exactly what was done by others and what I have contributed myself;
7. None of this work has been published before submission;

Signature: _____ **Date:** _____

Acknowledgements

I would like to sincerely thank my supervisors, Tim Waters, Michał Kalkowski and Jen Muggleton for their help, encouragement and endless patience whilst guiding me through this research project. Their insight and support have been invaluable to my academic progress. I also extend my thanks to members of my internal review panel, Prof. Neil Ferguson and Prof. Phillip Joseph for their thorough feedback and suggestions, as well as all those at the ISVR who have helped and supported me with their advice and teaching.

I would like to show gratitude to UK Research and Innovation for providing their financial support for this project.

Finally, I would like to thank all members of my family, and the many others besides who have acted as such, for helping me reach this point.

Contents

Abstract i
Declaration of Authorship ii
Acknowledgements iii
Table of Contents iv

1 Introduction **1**
1.1 Biofouling and Invasive Mussels 1
1.1.1 Zebra Mussels & Associated Problems 1
1.1.2 Concluding Remarks 5
1.2 Wave Propagation in Pipes 5
1.2.1 Bulk vs Guided Waves 5
1.2.2 Simple One-Dimensional Models 7
1.2.3 Plate Theories 10
1.2.4 Thin Cylindrical Shell Theories 10
1.2.5 Exact Theories 11
1.2.6 Numerical Models 12
1.3 Energy Focussing and Time Reversal 14
1.3.1 Phased Array 14
1.3.2 Dispersion Compensation 15
1.3.3 Time Reversal 16
1.4 Aims of the Thesis 18
1.5 Outline of the Thesis 18
1.6 Contributions of the Thesis 19

2 Acoustic Focussing in a Rigid Walled Duct **20**
2.1 Analytical Formulation 20
2.1.1 Damping 24
2.1.2 Monopole Source Expansion 27
2.2 Harmonic Response 28
2.3 Time Domain Response 30
2.4 Time Reversal 31
2.4.1 Application 32
2.4.2 Performance vs Harmonic 35
2.4.3 Pulse Frequency Modulation 37
2.5 Discussion and Conclusions 39

3 Axisymmetric Wave Propagation and Focussing in a Fluid-Filled Pipe **41**
3.1 Introduction 41

3.2 Numerical Modelling & Validation . . . 42
3.2.1 Conventional FE Model . . . 43
3.2.2 WFE Model . . . 44
3.3 Free Wave Propagation . . . 44
3.3.1 Dispersion . . . 46
3.3.2 Attenuation . . . 48
3.3.3 Energy Distribution . . . 49
3.4 Forced Response . . . 50
3.4.1 Input Power Distribution . . . 51
3.4.2 Transferred Power & Distribution . . . 52
3.4.3 Rigid Duct Comparison . . . 54
3.5 Time Reversal Focussing . . . 57
3.5.1 Application . . . 57
3.5.2 Performance vs Harmonic . . . 60
3.6 Conclusions . . . 63
3.6.1 Discussion . . . 63
3.6.2 Conclusion . . . 64

4 Higher-Order Wave Propagation and Focussing in a Fluid-Filled Pipe 66
4.1 Introduction . . . 66
4.2 Numerical Modelling . . . 66
4.3 Analysis of Higher Order Modes . . . 67
4.3.1 Free Waves . . . 67
4.3.2 Forced Waves and Focussing . . . 70
4.4 Point Excitation . . . 75
4.4.1 Formulation . . . 76
4.4.2 Harmonic Power Flow . . . 79
4.4.3 Time Reversal and Spatial Focussing . . . 80
4.4.4 Influence of Bandwidth . . . 83
4.5 Conclusion . . . 84

5 Application of Guided Waves for Zebra Mussel Antifouling 85
5.1 Quantitative Benchmarking of Mussel Antifouling Studies . . . 85
5.1.1 Acoustic Pressure . . . 86
5.1.2 Structural Vibration . . . 87
5.2 Structural Excitation with Inertial Actuator . . . 90
5.2.1 Inertial Actuator Model . . . 90
5.2.2 Pressure Response . . . 92
5.2.3 Acceleration Response . . . 93
5.2.4 Axial Coverage . . . 94
5.3 Conclusions . . . 98

6 Conclusions 99
6.1 Summary of Present Work . . . 99
6.2 Implications for Antifouling and Suggestions for Future Work . . . 100

Appendices **115**

A One Dimensional Theories **116**
A.1 Equations of Motion 116
A.1.1 Fluid Plane Wave 116
A.1.2 Simple Rod 116
A.1.3 Simple Shaft 117
A.1.4 Euler-Bernoulli Beam 117
A.1.5 Timoshenko Beam 117
A.2 Dispersion Relations 118

B Thin Cylindrical Shell Theory **120**
B.1 In Vacuo 120
B.2 Fluid Coupled 122

C The WFE Method **123**
C.1 Formulation of Eigenproblem 123
C.2 Eigensolutions 125
C.3 Forced Response 125
C.4 Python Implementation Code 126

1. Introduction

1.1 Biofouling and Invasive Mussels

Biofouling or biological fouling is the unwanted accumulation of organisms on engineering structures, particularly those submerged in water. In addition to the build-up of bacteria, algae and other smaller organisms (microfouling), larger creatures such as barnacles and mussels attach themselves to underwater surfaces (macrofouling) [1]. Both types of biofouling are associated with a range of problems for the affected structures which may include ships, navigation buoys and underwater sound equipment [2]. For example, in the shipping industry much emphasis is placed on reducing fouling on the hull of vessels due to the resulting increased hydrodynamic drag, which can have a large impact on fuel efficiency and thus incur considerable economic costs [3, 4].

In the water and energy industries, biofouling in piping systems presents a significant problem. Exposure of water intake pipes to macrofouling can result in large reductions in flow. If left untreated, organic matter will be carried farther into the system where it interferes with downstream equipment such as filters and pumps. In recent decades, this issue has received increased attention due to the introduction of invasive mussels into freshwater lakes worldwide. Zebra mussels (and their close cousin quagga mussels) are a small species of mussel native to Eastern Europe with the ability to form dense, multilayer colonies on hard substrates. Where they have been accidentally dispersed into bodies of freshwater, these bivalves can rapidly surpass densities of 1000 per square meter [5], affecting ecosystems and industries alike. Water intake pipes are one of the structures most affected by invasive mussel fouling, the prevention of which is the focus of this research project.

1.1.1 Zebra Mussels & Associated Problems

Biology The zebra mussel (*Dreissena Polymorpha*) is a freshwater bivalve originating from the Caspian Sea region. After external fertilisation, these animals begin their lifecycle as planktonic larvae known as veligers and are dispersed mainly by water currents. Some time later (around 10 days) the veliger grows a small foot allowing locomotion on surfaces [6] and becomes known as a pediveliger. At this stage the pediveliger begins its search for a suitable substrate on which to settle and, once found, secretes proteins called byssal threads which attach it firmly to the chosen surface. After settling, the mussels begin filter feeding and grow into juveniles and eventually adults, during which time they develop their characteristic hard shell. In total, the lifecycle typically lasts around 3-5 years depending on

temperature [7].

The closely related quagga mussel (*Dreissena rostriformis*) shares many of the characteristics of the zebra mussel. It is slightly larger and, unlike zebra mussels, able to colonise soft substrates such as those found at the bottom of lakes. Zebra mussels are better able to resist dislodgement in high velocity water flows [8] and it is for this reason that they are the main focus when discussing the fouling of water intake pipes. Often both species are referred to collectively as zebra mussels.

Proliferation Zebra mussels are an invasive species in many parts of the world. Most notable has been their rapid spread throughout the Great Lakes in North America, where they apparently arrived via a ship water ballast in the mid 1980's [7]. Since then the population of zebra mussels in these lakes has exploded [9]. For example, densities of over 30,000 individuals per square meter have been found in Lake Erie a mere decade since their introduction [10]. Zebra mussels were first introduced in Britain (along with much of Western Europe) around 1820 and it is thought that after the initial spread, their numbers remained steady for over a century [11]. In recent years however, the creatures have begun spreading again on the island, likely due to increasing water quality following the decline in the use of chemical treatments at water intakes [12, 13]. Quagga mussels were first discovered in Britain in 2014. The spread continues, with quagga mussels being found in Rutland Water as recently as 2020 [14]. Elsewhere in Europe zebra mussels have spread to Sweden (1920), Ireland (1997) and Spain (2001) [15, 16].

Physical Impact The build-up of invasive mussels on the inside of pipes can have serious consequences for industries drawing freshwater from infested sources. The planktonic larvae of the mussels allows them to disperse into waterways quickly, easily passing into the piping systems of industrial plants. Once settled, the pipe provides an ideal habitat [7]. Free from predators and with a constant flow of water bringing food and removing waste, large colonies grow fast. Even once the pipe walls are completely coated, new layers form over the old, creating a thick crust of biomass (see Figure 1.1). Besides the reduction in flow rate, problems occur when living or dead mussels are washed farther into piping system. In 2005, a study documented the increasing effects of zebra mussels on water installations in England [12]. The problems reported at waterworks included blockage of intake pipes, microfilters, filter beds, ozone tanks and narrow sampling pipes. It was noted that these problems often follow a large change of flow through the pipeline, presumably dislodging large numbers of mussels from the pipe wall.

Economic Impact The economic impacts have received much attention in the Great Lakes, where early estimates of the cost of zebra mussels were over $3 billion to power companies alone between 1993-1999 [17]. One later estimate put the total cost at $1-1.5 billion in the years 1989-2007 with the energy and water industries paying one half and one third of this amount respectively. Since then, the cost estimates have been more modest, likely owing to the increased readiness of the affected industries to implement mitigation strategies. Still, a 2007 study estimated the Great Lakes invasion to have cost hundreds of millions in a similar period [18]. In Britain, where zebra mussels are less novel, aggregate figures on their cost are more difficult to assess. There are nevertheless ongoing costs of preventative and reactive procedures associated with the pests at many facilities [12].

Figure 1.1: Extent of zebra mussel colonisation of intake pipe

Current Treatments At present, a wide range of techniques have been used to control invasive mussels with varying success. A recent (2018) review by the US Department of the Interior (USDOI) [19] has identified some methods used so far, many of which appear in an earlier report prepared for the Canadian Government in 1989 [20]. Among these are chemical treatments, heat, dessication, electric/magnetic fields, UV irradiation, sound, vibration, predation and manual removal.

Chemical techniques have been preferred in industry with chlorination being perhaps the most popular [20]. Whilst effective, the treatment is non-specific and may have dangerous consequences for the surrounding environment, particularly where the water is returned to the source. Another control chemical is potassium salts, which has been notably used in the only documented eradication of a zebra mussel infestation in open water [21]. There is some concern however that potassium salts are also toxic to native species of mussel, limiting its use as a control technique. Anti-fouling paints have traditionally been used in the maritime industry, however these are difficult to apply in a pipeline and not without their own environmental risks.

More recent developments in chemical mussel treatment have yielded BioBullets [22] and Zequanox [23]. BioBullets were developed by researchers from Cambridge University and involve concentrated doses of potassium chloride, encapsulated in, and disguised as a food source to zebra mussels. This treatment has been shown to be highly effective and specific, and was commercialised in 2000. Zequanox is the trade name of a pesticide which is derived from a strain of bacteria (*Pseudomonas fluorescens*). This bacteria is deadly to the mussels when ingested but not recognised as such by the creatures themselves. Studies have suggested that Zequanox is also highly effective and specific.

Many of the non-chemical techniques tried have had mixed results, or difficulties in their practical implementation. For example heat treatment will only work at a plant specifically designed for it. Dessication and manual removal both require temporary shutdown.

Acoustic and Vibrational Techniques Some of the non-chemical control techniques tested so far have attempted to utilise sound and vibration to discourage or eliminate biofouling. A broad review of the literature in 2015 by Legg et al. [24] details some of the studies conducted in this area. Among the more common techniques employed for zebra mussels in pipes are acoustic sparkers. These devices rapidly discharge a capacitor between two electrodes underwater, creating a shock wave which can damage and kill the mussels. A study by Mackie [25] showed the technology was effective in preventing attachment to intake pipes 4 m long. A later study by Schaefer et al. [26] quantified and related the acoustic energy with mussel mortality. It was determined that the sparker's effective range was 1.5 m to kill, and 23 m to discourage mussel settlement. Sparkers appear to have already been deployed in some installations. Schaefer et al. notes one case in which a 550 m pipe has been kept free of fouling for over four years [27]. A project by the environmental protection agency also reports similar success using sparkers in removing mussels and preventing attachment over time [28]. There appears to have been no new research conducted on the use of sparkers since 2010.

In 1997 Donskoy [29] investigated the effects of sound and vibration on zebra mussels. It was remarked that these treatments were first studied in the USSR but discontinued after the success of chemical controls. A literature review divides the methods tested previously into cavitation, sound, and vibration. Donskoy then conducts his own investigation into the effects of these techniques on zebra mussels in various configurations. The experiments most relevant to this project studied the effects of vibration on veligers, as well as sound on veligers, adults and eggs. It was found that low frequency (< 20 kHz) vibration of the substrate can cause 100% mortality in veligers, where the lowest acceleration level tested was 0.1 $\mathrm{m\,s^{-2}}$. It appears that the effectiveness of the treatment diminishes at higher frequencies. Aside from vibration of the substrate, the use of low frequency sound was shown to significantly inhibit translocation and settlement of juvenile and adult mussels in Donksoy's studies. The attachment was also observed to be weaker in mussels treated with sound. One experiment demonstrated a 97% reduction in mussel attachment to surfaces when treated with 170 dB[1] of sound at 60 Hz over 24 hours. Donskoy also demonstrated that low frequency sound disrupts fertilisation and destroys zebra mussel eggs.

In 2015 researchers from the University of Hull demonstrated the sensitivity of the blue (common) mussel (*Mytilus edulis*) to vibration [30]. Excitation frequencies between 5-410 Hz were used, with the mussels showing behavioural changes (valve closure) at acceleration thresholds of 0.06-0.55 $\mathrm{m\,s^{-2}}$. Again, as with the work done by Donskoy, it appears that the sensitivity to vibration decreases with frequency.

More recently, in 2022, Kusku et al. performed a long term study using sound to treat zebra mussels. Frequencies of 500, 1000, and 5000 Hz were applied at relatively low pressures of 83-87 dB to zebra mussels in a tank over 100 days. The study determined that sound at these levels was sufficient to kill a significant portion of zebra mussels over the time frame of the experiment. For the three frequencies studied, the mortality rates after 100 days were 33, 37, and 45% respectively. Further to this, it was found that the average weight of the mussels which survived the sound treatment had decreased slightly, whereas the weight of mussels in the control tank had grown. The authors suggest that previous studies, which concluded sound did not induce mortality in zebra mussels, did not allow sufficient time to observe the long term effects of sound treatment.

[1] with respect to 1µPa of underwater sound pressure.

1.1.2 Concluding Remarks

An introduction to the problem of invasive mussel fouling in freshwater intake pipes has been presented in this section. A broad range of traditional treatment methods have been discussed with little indication of a single 'best' approach to combatting the issue. It has been shown that vibration of the substrate, at low frequencies and at high enough intensities, can cause mortality of zebra mussel velligers. It has also been shown that sound pressure in the surrounding fluid can discourage settlement and translocation of mussels, and may also induce mortality given the treatment time is long enough. In the case of water intake pipes, the substrate is the inner pipe wall, and the surrounding fluid is the water contained within. It is therefore the objective of this project to explore the means by which acoustic and vibrational energy may be applied to large sections of a fluid-filled pipe, with the aim of disturbing or discouraging the settlement of mussels inside.

1.2 Wave Propagation in Pipes

In this section, wave propagation in pipes is discussed through a summary of analytical and numerical models. A brief introduction to guided waves and their general characteristics is given, before a review of various analytical theories applicable to a pipe, both fluid-filled and *in vacuo*. After this, the popular modern numerical techniques used to tackle the problem are then summarized. The relative merits of each model is discussed whilst giving special consideration to the systems and frequency range deemed most relevant to this project.

1.2.1 Bulk vs Guided Waves

Bulk The problem of wave propagation in infinite homogeneous isotropic media is relatively straightforward. In a fluid, the acoustic wave equation governs and yields, for example, harmonic plane wave solutions travelling at a velocity which is constant and characteristic of the medium. These waves are purely longitudinal and describe the propagating compression and rarefaction of the fluid.

In an infinite solid, similar compressional waves exist. However, unlike fluids, solids resist shear deformation. This results in an additional type of wave, with displacement transverse to the direction of propagation and completely independent of the longitudinal motion.

Common to all of these waves, known as bulk waves, is the fact that their dispersion relation is linear. That is, the relationship between wavenumber k and angular frequency ω is given by a simple constant, which is the phase velocity of the wave c_p.

$$c_p = \frac{\omega}{k} \tag{1.1}$$

In addition, the group velocity c_g, which for a perfectly elastic medium is the speed of energy propagation, is given by

$$c_g = \frac{d\omega}{dk}. \tag{1.2}$$

Waves with a linear dispersion relation are known as non-dispersive waves. This is because the phase and group velocities are equal and independent of frequency. As a consequence, a pulse of arbitrary shape (and frequency content) will propagate

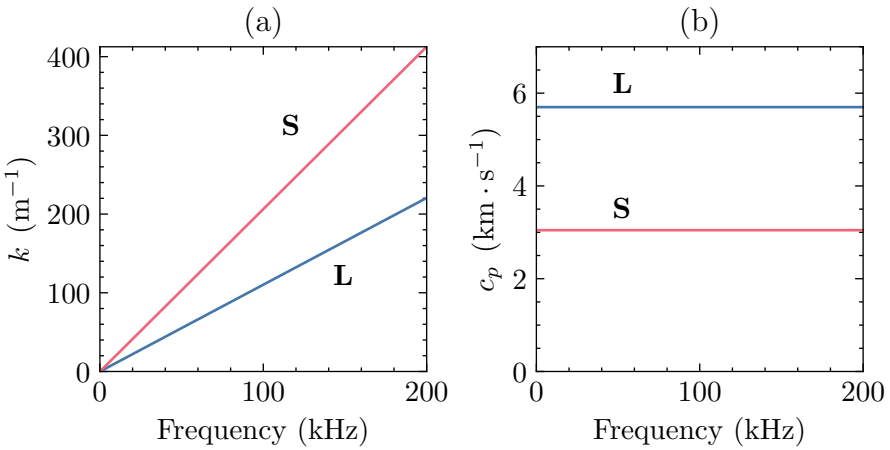

Figure 1.2: (a) The dispersion relation and (b) phase velocity of **L**ongitudinal and **S**hear bulk waves in steel. These waves show no dispersion and have a speed independent of frequency.

undistorted in the direction of travel. The dispersion relation gives pairs of k and ω which may propagate in the medium (Figure 1.2)[2].

Guided By contrast, for a medium with finite geometry in one or more of its three dimensions, the boundary conditions which then require satisfying often add much complexity to the wave solutions. For example, in an infinite plate, the bulk compressional and shear waves reflect and convert between one another at the two traction-free boundaries. The resulting superposition gives rise to waves which travel along the plate, parallel to and 'guided' by the boundaries. These waves, known as Lamb waves, behave quite unlike the bulk waves which produce them. Instead of two wave types with unique velocities, there are a doubly infinite number of wave types with increasing frequency, known as 'modes' that travel at velocities dependent on frequency and the plate thickness. Furthermore, most of these modes only propagate above a particular frequency, known as the 'cut-on frequency'. Those waves which are propagating down to 0 Hz are known as 'fundamental' waves. Figure 1.3 shows some dispersion and phase velocity curves for a typical plate.

Each branch of the dispersion curve is associated with a particular mode with a characteristic cross-sectional displacement field, known as the 'mode shape'. For Lamb waves the branches are commonly divided into symmetric and antisymmetric modes, referring to the symmetry of the displacement about the mean surface of the plate. This example demonstrates many of the general characteristics of guided waves. For practical purposes, perhaps the most useful property of guided waves is their ability to travel significant distances along a structure with relatively little attenuation, which would arise in an infinite medium due to geometric spreading. This is something which has been exploited in the fields of non-destructive testing (NDT) and structural health monitoring (SHM), where guided waves can be used to probe large structures for defects [32]. However, before guided waves can be utilised practically, the multitude of propagating modes must first be untangled and understood. In this section, the aim is to review the theory of guided waves in water pipes, starting from the most elementary models.

[2]All plots in this thesis were formatted using the SciencePlots package for Matplotlib. [31]

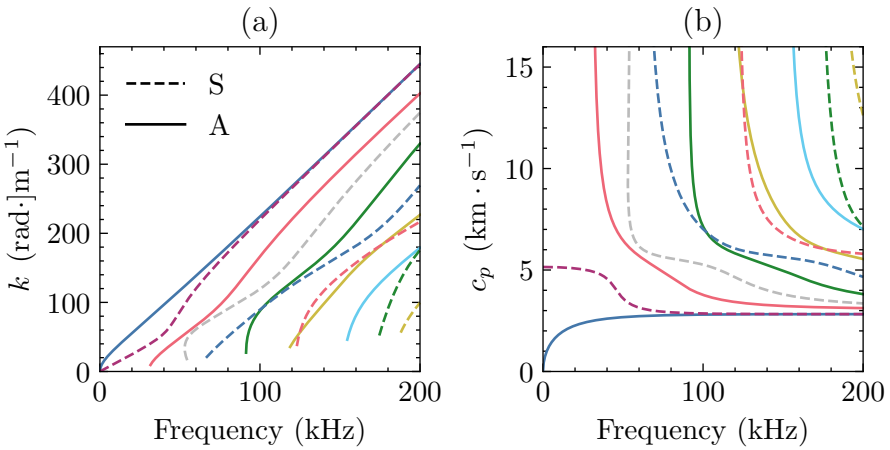

Figure 1.3: (a) Dispersion relation and (b) phase velocity of **S**ymmetric and **A**nti-symmetric Lamb waves in steel plate. A large number of dispersive modes are present.

1.2.2 Simple One-Dimensional Models

We begin with the simplest interpretations of the dynamic behaviour of an infinite pipe. The following one-dimensional theories give a basic understanding of wave propagation at the low frequency limit. The theories are divided loosely into the type of motion that they describe, namely acoustic, longitudinal, torsional and flexural. The mathematical formulation of these theories is provided in Appendix A.

Acoustic Waves The lowest order theory of acoustic wave propagation in a pipe describes a plane wave which is functionally identical to those which propagate in free space. In this case, the system is often referred to as a 'duct' and the pipe walls are assumed to be rigid. The pressure field is uniform over the cross-section of the pipe and the wave propagation is non-dispersive. In contrast to its free-space counterpart, the fundamental acoustic mode in a duct is confined to propagate in one dimension only, and is therefore not attenuated by geometric spreading. The low attenuation and non-dispersive behaviour of this wave is widely exploited in the field of leak detection, where low frequency perturbations can be detected at significant distances from the source. Development of the plane wave theory is attributed to Lord Rayleigh [33].

In a water pipe, the plane wave is the only acoustic mode which is fundamental and propagates at zero frequency. The theory is accurate in a pipe with rigid walls when the wavelength is much longer than the pipe radius. When the wavelength becomes shorter than the radius, additional modes begin to propagate which are described with higher-order theories. In the case where the pipe walls are considered to be flexible, a model which includes the fluid-structure interaction must be used to accurately describe the wave motion.

Longitudinal Considering the longitudinal wave motion in the structure at low frequency (Figure 1.4a), a pipe can be considered as a thin rod. The elementary theory is provided in many textbooks, for example those by Graff [34], Cremer [35], and Junger and Feit [36]. The assumptions inherent to the theory are that the

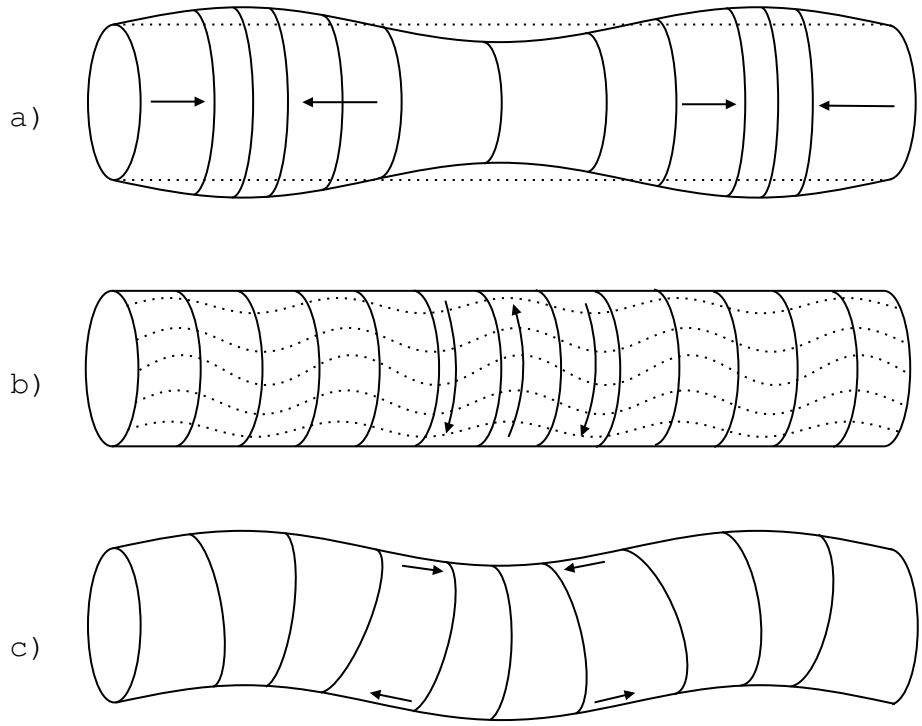

Figure 1.4: Three types of motion in the pipe structure described by elementary theories. a) Longitudinal b) Torsional c) Flexural motion.

rod is 'thin' so that the wavelength is much longer than the radius, the stress is uniform along the cross-sections which remain plane and parallel, the stress is uniaxial and lateral strains carry no inertia.

The equation of motion is a simple, non-dispersive wave equation. The model predicts a single mode which travels at a constant velocity independent of frequency. Qualitatively the solution is very similar to the bulk compressional waves discussed in Section 1.2.1, with the only difference being the wave speed, which is about 10% slower in the case of a metallic rod. Physically, this is explained by the lateral expansions occurring in the rod due the Poisson effect. Since this means that displacement is not purely longitudinal these waves are often called 'quasi-longitudinal' [35].

This elementary theory is extremely limited by frequency range and its practical use for a pipe does not go much beyond the prediction of longitudinal wave speed near zero frequency. For a rod theory that is applicable to a higher frequency range, Love [37] included the effects of lateral inertia due to the Poisson expansions. By including this, the equation of motion is of the fourth order and the resulting wave is dispersive, with both phase and group velocities decreasing with frequency. This behaviour is also seen for the fundamental longitudinal mode in a pipe. Higher order rod theories will not feature in this project since they do not account for behaviour specific to a pipe.

Torsional The torsional (Figure 1.4b) waves in an infinite rod (often called a shaft in this case) are described in the most basic theory by the 1D wave equation, presented in textbooks by Graff [34] and Cremer [35]. The resulting non-dispersive wave has a velocity which is dependent on the cross-sectional shape of the rod. For cylindrical rods, including hollow cylinders, the velocity is that of the shear wave

speed in infinite media. This is understood through the fact that the motion in this geometry is purely torsional, uncoupled from motion in any other direction, and so the restoring force is provided only by the shear rigidity between adjacent cross-sections.

One might expect this elementary theory to break down at higher frequencies, as with the longitudinal theory. However, for cylindrical geometries, this model describes the exceptional case where an elementary theory is valid at all frequencies. The fundamental torsional mode of any cylindrical bar or rod is expected to be a simple non-dispersive wave travelling at the shear wave speed of the material.

Flexural Flexural (also called bending) waves are unlike the primarily shear or longitudinal waves discussed so far. Although the largest component of displacement is transverse to the direction of propagation (Figure 1.4c), the strains that dominate the potential energy are in the longitudinal direction [35]. An infinite number of bending modes are present in a pipe, however only one is nascent down to zero frequency, known as the 'beam bending' mode. The name naturally derives from analogy with flexural waves in a beam, for which there are a few basic one-dimensional theories.

The Euler-Bernoulli beam theory (EBBT) is the simplest beam bending theory, often called classical beam theory or engineers beam theory. Developed around 1750 [38], the model has been in use for centuries to solve statics problems where the deflection is small, or dynamics problems where the frequency is low.

The central assumptions are as follows. Firstly, deflections must be small, so that the curvature of the beam may be approximated by the second derivative of the transverse deflection. Secondly, cross-sectional planes which are perpendicular to the neutral axis remain perpendicular after bending, and the neutral axis runs through the centroid of the beam's cross-section. Lastly, the effects of rotational inertia are neglected, an assumption similar to neglecting lateral inertia in the case of longitudinal waves in a rod.

The dynamic equation of motion for the EBBT is given by a fourth order partial differential equation. Substitution of a harmonic wave solution into the governing equation reveals a wavenumber which increases with square root of angular frequency. Similarly the phase and group velocities increase in the same manner, with the group velocity being twice that of the phase velocity.

Although accurate at low frequencies, the EBBT has an unbounded wave speed with frequency, which is obviously unphysical. This is particularly troublesome when studying transient problems. Finite wavespeed was achieved by Raleigh's addition of rotational inertia [33] and later Timoshenko included the effects of shear deformation [39]. Timoshenko's correction lead to a beam theory which, as remarked by Graff, [34] shows a very close agreement with results obtained from the exact equations of linear elasticity.

For the purpose of modelling free wave propagation in a pipe, both the Euler-Bernoulli and Timoshenko beam theories may be used at the very lowest frequencies to model the beam bending mode, with the EBBT having the obvious advantage of reduced complexity where it is accurate. Timoshenko's theory may be used at frequencies higher than the range of validity of the EBBT. A rule of thumb is that the lateral dimension of the beam should be less than one-tenth of the wavelength. Both theories will eventually diverge from the behaviour of the beam bending mode in a pipe however. This is because the analogy of the pipe as a beam is imperfect, and behaviour specific to the pipe will begin to dominate at

higher frequencies.

1.2.3 Plate Theories

The elementary one-dimensional models reviewed so far approximate the dynamics of the pipe in the low frequency limit, where the wavelength is much longer than the pipe radius. Conversely, when the wavelength is much smaller than the radius, the pipe wall dynamics are well approximated by considering the system as a plate.

The lowest order plate theories have many similarities with their one-dimensional counterparts. The longitudinal motion is similar to that in a rod, with a slightly higher wave velocity [40]. The transverse, or bending waves are described in the simplest case with either the Kirchhoff-Love or Mindlin plate theories. These are analogous to, and derived from the same assumptions as the Euler-Bernoulli and Timoshenko theories respectively. Like the beam theories, they are only accurate when the wavelength is long compared to the thickness of the plate.

Exact plate theories are derived using the equations of linear elasticity, considering the interaction of bulk and shear waves with the traction-free boundaries. The bulk waves are separated into longitudinal compressional waves, (sometimes known as P-waves) and shear waves. Shear waves are further grouped into those which consist of transverse motion in and out of plane, known as shear-horizontal (SH) and shear-vertical (SV) respectively. SH waves are uncoupled from other types of motion and the fundamental SH mode is non-dispersive at all frequencies, similar to the torsional wave in a shaft. The remaining P and SV waves combined give rise to the Lamb wave solutions [41], which are widely used for non-destructive testing in plate-like structures such as aeroplane fuselages or boat hulls.

The frequency range for which the plate theories are applicable is above that considered by this project. Nevertheless the theories have been reviewed here for completeness.

1.2.4 Thin Cylindrical Shell Theories

Until now, all theories discussed have dealt with idealised systems which do not account for the geometry unique to a pipe. These models are only accurate in the narrow wavelength regime where the pipe behaves approximately like another system. Thin cylindrical shell theories formulate the dynamic behaviour of a pipe in terms of stresses and strains of the mean radius, which occur in the axial, tangential and radial directions of a cylindrical coordinate system. The curvature effects, which couple stresses in, for instance, the radial and tangential directions are accounted for as well as the continuity condition around the circumference of the pipe. By including these effects the behaviour which is characteristic of pipe systems specifically is seen.

The continuity condition necessitates solutions with harmonically varying displacements in the circumferential direction. This allows modes to be classified by the number of wavelengths n around the circumference, known as the circumferential mode order. Where $n = 0$ there is no variation in displacement around the circumference of the pipe and for this reason these modes are known as axisymmetric modes. Axisymmetric modes include all longitudinal modes and the fundamental torsional mode.

There is a large number of different shell theories which can be found in the literature. Although very similar for most practical purposes, each may be de-

rived with sightly different approximations or assumptions on the kinematics of deformation. An extensive review of various shell theories and their differences has been performed by Leissa [42]. The first shell theory for cylinders was produced by Love [37] and since then many modifications have been made by, for example, Donnell [43], Flügge [44] and Kennard [45]. Each of these theories is governed by three coupled partial differential equations which can be solved with harmonic solutions for each displacement component. The dispersion relation is in the form of an 8th order polynomial for the case of *in vacuo* shells.

Central to the assumptions of these theories are that the shell wall is thin, i.e the thickness to radius ratio is very small. This assumption requires only the displacements of the middle surface to be considered and essentially neglects effects associated with transverse shearing or rotary inertia of the shell walls. These assumptions are shown to give results which agree well with the exact theory for a considerable range of frequencies, as shown by Greenspon [46].

Shell theories have been used to great effect in theoretical investigations of wave propagation in an infinite pipe, both *in vacuo* and fluid-filled. Smith [47] analysed the dispersion relations and displacement characteristics of free waves *in vacuo* using Kennards theory, separating the modes into three distinct classes. Lin and Morgan [48] presented phase velocity curves for a shell coupled to an internal fluid. Later the coupled system was also solved and analysed by Fuller and Fahy, [49] who gave expressions for the energy distribution between fluid and structure. These analyses have since been reproduced in works by De Jong [50] and Brevart [51] for the purpose of studying vibration in piping systems. Notable work using shell theory has also been done by Fuller [52–55] and Pavić [56, 57].

For the purpose of this project, shell theories can be useful in predicting dispersion curves and displacement profiles for a considerable range of frequencies. One particularly important frequency, known as the 'ring frequency', occurs when the wavelength of the longitudinal wave in the shell wall is equal to the circumference [40]. This transitional frequency marks the boundary between two different types of shell behaviour. With this, it is seen that the models discussed before now were only applicable well below the ring frequency (rods/beams) or well above (plates). The thin shell theory gives a model which is much more complete in its description of the pipe dynamics below, at and above the ring frequency, provided the relevant assumptions hold. The mathematical formulation for the Flügge model is provided in Appendix B.

1.2.5 Exact Theories

By using the exact equations of linear elasticity, and formulating the wave propagation in a structure by considering the superposition of bulk waves subject to the boundary conditions, so-called 'exact' theories may be developed for the simplest geometries. These theories are accurate at all frequencies for any sized system. Naturally with the increase in accuracy comes considerable complexity in the solutions. In fact, many of these theories were developed before the computational means were readily available to solve them. These theories thus conclude the discussion of analytical models and a brief review thereof is given for the sake of completeness.

The full frequency equation for an infinite solid rod was first given by Pochhammer [58] and Chree [59], although solutions were not sought for quite some time. In a similar way, Lamb developed the characteristic equations for the infinite plate [41]

which were only solved years later. The problem of hollow cylinders was presented and solved by Gazis [60, 61] and his approach was followed by Meeker & Meitlzer [62] who solved the problem of solid cylinders and plates. Further analysis on hollow cylinders was performed by McNiven et al. [63, 64] and the case of fluid-filled cylinders was investigated extensively by Kumar [65–67] and Del Grosso [68]. A modern implementation of the exact theory for hollow cylinders has been given in a textbook by Rose [69].

For the purpose of this project these exact theories bring unneeded complexity when analysing thin cylindrical hollow cylinders over a fairly narrow frequency range. Solutions are only available for a few restricted geometries and require robust complex root finding algorithms. Because of this, there is little reason to pursue solutions for such theories over simpler analytical models or more general numerical methods.

1.2.6 Numerical Models

In this section, an overview of the popular numerical methods for modelling guided waves in pipes is given, with specific considerations given to their implementation, including freely or commercially available software packages. As mentioned before, analytical models are limited in their generality. For complex geometries and external/internal couplings analytical solutions are unlikely to exist, and where they do, require numerical methods to fully solve in any case. It is for this reason that numerical techniques are increasingly popular for the purposes of modelling guided waves.

Matrix Methods One of the first modelling methods was developed for multi-layer waveguides and is known as the 'Transfer Matrix Method'. Introduced initially by Thomson [70] and corrected by Haskell [71], the technique formulates the stresses and displacements at each layer in terms of matrices which are then coupled together to create a single transfer matrix. The numerical instability of this method at high frequencies led to the development of the 'Global Matrix Method' by Knopoff [72] which is comparatively slower but does not suffer from such instabilities. Once the matrices are assembled, both methods require complex root searching to obtain the dispersion curves which is one of the main disadvantages. A summary of both matrix techniques is given by Lowe [73]. Both matrix methods work fundamentally by considering the superposition of bulk waves according to the equations of linear elasticity. De Jong used the transfer matrix method to model wave propagation through a fluid-filled pipe elbow [50]. Barshinger & Rose used the global matrix method to study a hollow cylinder with a viscoelastic coating [74]. Paviakovic and Lowe developed the popular software DISPERSE, now over 30 years old, [75] which uses the global matrix method and is capable of modelling hollow cylinders [76] and plates. Much more recently, Huber developed a free software DispersionCalculator for isotropic and anisotropic plates [77]. The software uses a stable reformulation of the transfer matrix method known as the stiffness matrix method [78, 79].

Finite Element Method Perhaps one of the most popular methods of numerical modelling for a range of problems in linear elasticity is the finite element method (FEM). This technique involves subdividing a physical domain into a large

number of small parts (known as a meshing) governed by relatively simple equations. These elements are then reassembled to solve for the whole system. The FEM is very powerful when modelling complex geometries, due to the ability to mesh a domain with elements of variable size. Finite element models may be used to perform analysis of the static, time domain, or frequency domain behaviour of a given system. Frequency domain simulations can give insight into the modal characteristics of the system whereas time domain simulations allow analysis of transient forcing.

The FEM has been used to model time domain behaviour in pipes. For example the interaction of guided waves with defects [80, 81] or the focusing of waves with multiple radially attached transducers [82,83]. The main disadvantage of the method, generally speaking, is the computation time naturally increases with the number of elements and the size of the system. When attempting to model the behaviour of an infinite waveguide, obvious complications arise. In the time domain, a very large system must be modelled and then truncated before reflections can interfere with the results. In the frequency domain, perfectly matched layers (PML) [84] may be used at the ends of a sufficiently long waveguide to terminate any incident waves.

Fortunately, the drawbacks of using a 'full' FEM can often be avoided using techniques which only model a small section of the waveguide. The semi-analytical finite element (SAFE) method is one such technique which requires only the cross-section of the waveguide to be meshed. The technique dates back to 1973 [85, 86] but was popularised by Gavri [87], who used it to study wave propagation in a rail. The ability to model a waveguide of arbitrary cross-section has seen SAFE used in a wide range of different problems, a selection of which can be found in Ref. [88]. The basic assumption of the technique is that the displacement field in the axial direction takes the analytical form of a harmonic wave, effectively reducing the number of dimensions of the problem. For axisymmetric waveguides just one dimension requires meshing [89]. With SAFE, obtaining the dispersion relation reduces to an eigenproblem which can be solved with any of the available methods. In addition to arbitrary geometries, SAFE is also able to model waveguides coupled to an infinite surrounding medium [90, 91].

In recent years, some work has been done simplifying the use of SAFE by implementing the technique in commercially available FEM packages, avoiding the need for researchers to write their own finite element code [92]. Predoi et al. presented a formulation of SAFE which can be implemented with PDE solvers in many commercial FEM packages [93]. This was used by Thakare et al. to model wave propagation in bones using COMSOL's coefficient form PDE solver [94] but requires manual input of a large number of stiffness coefficients. Recently, a native implementation of SAFE was added to COMSOL's structural mechanics module, where one may solve for the 'out-of-plane wavenumber' [95] of the 2D domain using a modal analysis study (page 312 of Ref. [96]). In 2011, Bocchini et al. presented their free software Graphical User Interface for Guided Ultrasonic waves (GUIGUW) [97] which uses the SAFE. The software is capable of modelling plates and cylinders as well as arbitrary cross-sections.

Another method similar qualitatively to SAFE, is the wave finite element (WFE) method. Developed much more recently [98, 99], the WFE method models a small segment of the waveguide using conventional finite elements and then imposes periodicity in the direction of wave propagation. This method can be used to predict transmission through defects by coupling damaged and undamaged waveg-

uides as shown by Zhou & Ichchou [100]. The WFE method has been used in many of the same contexts as SAFE, and has also been extended to 2D structures [101]. Comparisons between SAFE and the WFE method were also given by Zhou [102]

Finite element methods are one of the most popular, effective and robust numerical techniques for modelling guided waves. With FEM, one may perform a wide range of analyses on waveguides such as pipes, including fluid-filled pipes with surrounding media. Studies in the frequency domain allow modal characteristics, including dispersion relations and displacement fields to be obtained, and the semi-analytical techniques such as SAFE and WFE allow this to be done with relatively minimal computational overhead. In this project, the WFE method is used extensively to study the vibro-acoustic behaviour of water filled steel pipes. Details of the WFE method and its implementation as an open source package in the Python programming language are given in Appendix C.

1.3 Energy Focussing and Time Reversal

For the application of antifouling, two broad objectives of this project can be considered:

- To maximise some vibrational/acoustic quantity (velocity, acceleration, pressure etc.) at a targeted problem location in the waveguide (pipe).
- To maximise the length of the waveguide over which some vibrational quantity may be maintained above a minimum threshold.

It is for this reason that techniques for energy focusing will be reviewed in this section. Energy focusing allows for amplification of guided waves and can help mitigate the attenuation due to losses in the waveguide. Two main techniques have been identified, namely those which converge energy from multiple separate transducers (phased array) and those utilising mode dispersion to spatially/temporally compress waveforms (dispersion compensation). Finally time reversal is discussed as a special method of realising both of the aforementioned techniques.

1.3.1 Phased Array

One of the most conceptually straightforward methods of focusing energy at a given target is to utilise multiple transducers. Provided two or more excited waveforms meet in phase, an increase in amplitude can be achieved through superposition. By using a large array of transducers, each with programmable time delays, a beam may be formed to converge at a chosen target.

This technology has seen a fair amount of discussion in the NDT literature, with the goal of enhancing defect detection. The phased array allows a larger concentration of energy to impinge on a target area, with a larger, better localised echo resulting from any potential defect. Furthermore the focusing allows inspection to be performed at a larger range by overcoming attenuation. Broadly speaking, much of the published literature in this area is mostly concerned with increasing the signal-to-noise ratio (SNR) of existing detection techniques. This is important to keep in mind, since 'noise' has comparatively little meaning in the context of this project.

In plates, phased arrays have been used with Lamb waves to create a steerable beam, allowing targeted inspection of the whole structure. Such technology has

been presented in a number of papers [103–105] and for a variety of different array topologies possible on a 2D surface [106]. The same techniques have also been used at high frequency in a pipe, where the pipe system behaves approximately like a flat plate with periodic boundary conditions at the edges [107].

For phased array technology developed exclusively for pipes, most notable contributions have been made by researchers at Pennsylvania State University. Li & Rose [108] first described the circumferential displacement distribution resulting from a non-axisymmetric partial loading of a hollow cylinder using the normal mode expansion technique (NME) [109]. They found that this displacement distribution, named the 'angular profile', varies with frequency of excitation and axial propagation distance. These results were used in a follow-up paper to predict the angular profile of an array of circumferentially mounted transducers. With this, an algorithm was presented to tune the amplitudes and phase of each individual transducer to achieve maximum energy focusing at a desired axial and angular position [110]. The study was experimentally validated using excitation frequencies of around 300kHz. In a later study [111], Hayashi et al. verified the technique using the SAFE method with similar excitation frequencies. Zhang et al. [112] investigated the ability of the phased array to focus beyond axisymmetric welds in pipelines. A 35kHz excitation was used and it was found that the welds had little effect on the efficacy of the focusing technique. Luo & Rose [82] tested phased arrays in a cylinder with a viscoelastic coating which similarly had little effect on focusing. At an axial distance of 1.5m, it was shown that phased array focusing with 8 transducers could produce 5× the peak energy of a comparable axisymmetric wave at a target location. Subsequent work has been concentrated on defect location/sizing and can be found in Refs. [113, 114]. Recently a similar method was applied to irregular waveguides [115].

Although it has been mentioned, it is important to emphasise that these developments have occurred with the objective of defect detection, and thus do not align exactly with the aims of this project. However, it stands to reason that the use of a phased array of N transducers will achieve at most an amplification of $N\times$ the amplitude of a single transducer. This concludes the discussion of phased arrays for energy focusing.

1.3.2 Dispersion Compensation

It is well established that the dispersion of guided waves causes waveforms with mixed frequency content to spatially and temporally broaden as they propagate. This is due to the frequency dependent wave speed, which causes the various spectral components of an excitation to separate along the direction of travel. The extent to which this effect is present depends on the bandwidth of excitation and the amount of mode dispersion present over this bandwidth.

Traditionally, this phenomenon is avoided in the field of non-destructive testing, where it can interfere with SNR and spatial resolution [116]. However, as many researchers have noticed, this effect may be controlled for with accurate knowledge of the waveguide dispersion curves. By assuming the distance of propagation, a received signal which is heavily dispersed may be 'compensated' thereby removing the effects of dispersion. Similarly, a temporally long, broadband excitation may be designed such that all frequency components converge at a specified distance from the transmitter, resulting in a large peak amplitude at the focal point. This latter possibility is critical, since it presents the ability to focus energy from a

single transducer along a one-dimensional waveguide. A review is thus given on the techniques used for compensating dispersion. As with the phased array, most of the literature in this area has been concentrated on NDT, with an emphasis on increasing spatial resolution and SNR.

Alleyene et al. proposed a method of dispersion pre-compensation for Lamb waves [117]. It was suggested that a compensated waveform would be much more sensitive to defects along the propagation path. A similar technique was applied to a steel wire by Yamasaki et al. [118], who applied appropriate phase shifts to each Fourier component of a square pulse, such that dispersion was compensated for a given propagation distance after transmission. Wilcox devised an algorithm to compensate for an assumed propagation distance of received signals post-acquisition [119]. He also investigated how inaccuracies in the dispersion relation affected the results. Compensation was used to separate overlapping Lamb modes by Xu et al. [120]. Dion et al. presented a method of generating large amplitude shock waves in water using a solid cylindrical (60cm long) waveguide to focus energy [121], which was subsequently patented [122]. A frequency dispersion pre-compensation method for Lamb waves was presented by Zeng et al. [123] who later expanded the technique to compensate for the excitation amplitude dependence on frequency [124]. An iterative time-of-flight extraction method was developed by Ycel et al. [125]. The technique involved transmitting a waveform with a delta-like autocorrelation function, and compensating the received echo for different propagation distances until a maximum autocorrelation peak was achieved. Autocorrelating transmitted and received signals to achieve higher SNR is sometimes known as pulse compression (PuC) [126]. Legg et al. used pulse compression and dispersion compensation to inspect overhead transmission line cables at distances of up to 130m. A chirp excitation designed using the dispersion relation for an Euler-Bernoulli beam was analytically and experimentally tested by Waters for the purpose of creating a large amplitude shock at a desired focal point [127]. It was shown that the level of amplification in the undamped case increased approximately in proportion to the square root of focal point distance, but in practice the peak response was heavily affected by damping as well as the the frequency response of the actuator. Van Gemmern et al. used a Timoshenko beam model to focus energy in a 1.5m long glass beam [128]. Dispersion compensation with multiple reflections were utilised to achieve an amplification factor of 20, resulting in fracture of the beam within 5mm of the focal point. A similar square root relation between amplification and distance was seen.

This concludes the discussion on dispersion compensation. It is clear from this short review that the cases in which compensation has been utilised to specifically maximise the peak response amplitude are relatively rare. Nevertheless the technique shows promise for the purposes of increasing the peak response at a focal point, as well as overcoming attenuation.

1.3.3 Time Reversal

Time reversal (TR) is a process whereby the response of some distant excitation is measured by one or more transducers. Assuming that the transducers are reciprocal and linear, and the medium is lossless, then the response can be made to reconverge back on the original source by temporally reversing and retransmitting from the measurement point(s). This is mathematically equivalent to reversing time, and works due to the time-symmetry of the wave equation. Popularisation

of TR techniques in acoustics is widely attributed to Mathias Fink, who has performed a great deal of work on the topic with colleagues since the early 1990s. An introduction to time reversal with examples may be found in Refs. [129, 130]. The main advantage of time reversal is that no prior theoretical knowledge is required of the wave propagation between source and receiver in order to focus energy.

In acoustics, time reversal is often performed with a large array of transducers known as a time reversal mirror (TRM). The TRM allows the acoustic pressure field to be sampled over a large area, allowing a higher level of spatial recompression upon reversal and transmission. In this way the TRM performs essentially the same function as a phased array. However, in this case, no manual tuning of phase delays or amplitudes are required, since all of the information needed is contained in the measured waveforms. Time reversal is also capable of undoing the effect of dispersion in one-dimensional waveguides. For example, measuring, reversing and transmitting the impulse response in such a waveguide will automatically recombine all frequency components into an impulse at the original source. In this way the time reversal method can be used for dispersion compensation without any prior knowledge of the waveguide dispersion curves.

Time reversal has been used in a large number of focusing studies in the past few decades. Derode et al. used a TRM to recompress the response of an acoustic point source propagated through a highly heterogeneous medium, in this case, 2000 steel rods immersed in water [131]. The high order scattering broadened the 1µs pulse into a response of over 200µs, which was then successfully refocused back at the source. Derode et al. later used the same experimental setup to investigate 1-bit time reversal [132]. It was found that digitising the measured response over 1-bit led to a larger peak upon reversal, and in some cases improved SNR. This is due to the 1-bit waveform having a much higher signal power whilst preserving most of the phase information. The 1-bit TR concept was employed by Montaldo et al. [133] for the purpose of creating large pressure pulses in water. A solid waveguide was used to compress energy through dispersion and multiple reflections. Applications to lithotripsy were considered in a later paper [134]. The researchers suggested that the 1-bit digitised impulse response leads to the largest time reversed peak at the source. The broader idea of using an 'ergodic' or 'chaotic' cavity for time reversal has been discussed by several authors [135–139] and optimal cavity design was considered by Arnal et al. [140]. Willardson et al. investigated high amplitude time reversal focusing in a reverberation chamber [141]. In addition to 1-bit digitisation, the authors experimented with three other ways in which the impulse response can be processed to achieve larger peak amplitudes or better focal quality. It was found that clipping the impulse response above a certain threshold resulted in the largest amplitude. This technique has been used in a plate to generate very large focal amplitudes [142]. Time reversal techniques have been applied to a pipe mostly in the context of non-destructive testing [143–146], although others have considered energy harvesting and blockage removal as possibilities [147].

The main disadvantage of time reversal is that both a source and receiver are typically required in order to refocus energy. However, given the wave propagation in a system can be accurately predicted, then the subsequent calculation of the system's impulse response at any point can allow the application of time reversal without a direct measurement. Since 1-bit TR theoretically yields the maximum response for a specific point in any system, the technique features heavily in this thesis as a means to maximise the amplitude of sound/vibration in a fluid-filled pipe system for application of antifouling.

1.4 Aims of the Thesis

The aims of this thesis are the following:

- Compile and analyse the current body of research concerning acoustic/vibrational control of zebra mussel fouling.
- Assess the means by which sound and vibration amplitudes can be maximised in a water intake pipe system for the purpose of antifouling.
- Model and analyse wave propagation in fluid-filled pipes, to inform the development of a prospective acoustic/vibration based antifouling strategy.
- Compare the modelled response in the pipe to the existing biofouling research in order to draw some early conclusions for the feasibility of the proposed technique.

1.5 Outline of the Thesis

In Chapter 1, the problem of invasive mussel fouling in water intake pipes is presented with a summary of the techniques both currently used and experimentally tested for antifouling. Sound and vibration is identified as a potential treatment method. A literature review is thus given on wave propagation in fluid-filled pipes along with techniques for energy focussing and maximising the response for antifouling purposes.

Chapter 2 then presents a simplified model of the system which considers only the waves in the fluid. The response to a monopole source is investigated and the time reversal method is introduced to maximise the pressure at targeted positions. Comparisons are made between a steady state harmonic excitation and the time reversal technique. It is shown that time reversal can significantly amplify the pressure response at a given point.

In Chapter 3, the problem is modelled in a fully-coupled system for the axisymmetric waves only. The Wave Finite Element (WFE) method is validated and used to study the free and forced wave propagation under some idealised assumptions. The time reversal method is once again applied to show the potential to increase the response at long distances from the source.

Chapter 4 extends the analysis of the fluid-filled pipe to all higher order waves. The different classes of wavemodes are analysed and the system is driven with a point force to demonstrate focussing with a phased array.

Finally, the analysis of a fluid-filled pipe concludes in Chapter 5 by modelling the system as driven by a commercially available actuator. The pressure and acceleration response is studied and compared to the existing research on acoustic/vibrational antifouling, with some tentative conclusions drawn about the feasibility of this technique.

To finish, the work in this thesis is summarised and some early conclusions are drawn in Chapter 6. Suggestions for future work are given. In the appendix, details of the WFE method are given and the Python model extensively used in this project is provided.

1.6 Contributions of the Thesis

- The thesis compiles and systematically analyses existing research on acoustic and vibrational control of zebra mussel fouling. Potential methods for energy focussing in a water pipe are summarised.
- The 1-bit time reversal method is applied to a simplified duct system as a means of demonstrating the the ability to amplify the peak response at a given point.
- The WFE method is used to analyse a fully-coupled fluid-filled pipe, with emphasis on the optimal bandwidth and excitation for long range power transfer. The harmonic and transient responses are compared with the aim of maximising the response.
- A numerical experiment is performed by coupling the WFE model to an inertial actuator. The levels of pressure and acceleration obtained through both harmonic and time reversal excitations are compared to the existing mussel antifouling literature. Early conclusions are drawn on the feasibility of the technique.

2. Acoustic Focussing in a Rigid Walled Duct

In this chapter, the acoustic wave propagation in a pipe is modelled by considering the system to be a rigid walled infinite duct. The normal mode expansion technique is used to obtain the wave solutions which are described in terms of their free-wave characteristics. The forced response is subsequently assessed using a monopole source expansion. In the interests of anti-fouling, the means by which the pressure can be maximised at the wall of the duct is presented. Firstly using a harmonic excitation, the pressure is found to peak at varying frequencies, mostly associated with the cut-on of higher-order modes. After this, the time-domain response to a transient excitation is studied. Here, the time reversal method is introduced, and modified with the aim of producing the maximum instantaneous pressure response at a targeted distance. The time reversal technique is shown to produce pressures much greater than is possible with a harmonic excitation at the same point, albeit with a lower average input power.

2.1 Analytical Formulation

The higher-order theory of acoustic waves in a duct is well established [148, 149]. The problem is briefly derived beginning with the acoustic wave equation in three-dimensions, which describes pressure field over space and time coordinates $p(\mathbf{r}, t)$

$$\nabla^2 p = \frac{1}{c_0^2}\frac{\partial^2 p}{\partial t^2} \tag{2.1}$$

where c_0 is the sound speed in the medium. The spatial and temporal variations in pressure are assumed to be independent such that $p(\mathbf{r}, t) = P(\mathbf{r})T(t)$, which leads to the following separation of variables

$$\frac{\nabla^2 P}{P} = \frac{1}{c_0^2 T}\frac{\mathrm{d}^2 T}{\mathrm{d}t^2} \tag{2.2}$$

Non-trivial solutions exist only if each side of equation is equal to the same constant, yielding two independent ODEs.

$$\frac{\nabla^2 P}{P} = -k^2 \quad \frac{1}{c_0^2 T}\frac{\mathrm{d}^2 T}{\mathrm{d}t^2} = -k^2. \tag{2.3}$$

The constant is chosen for convenience with a priori knowledge that k is the acoustic wavenumber in free-space defined as $k = \omega/c_0$, where ω is the angular

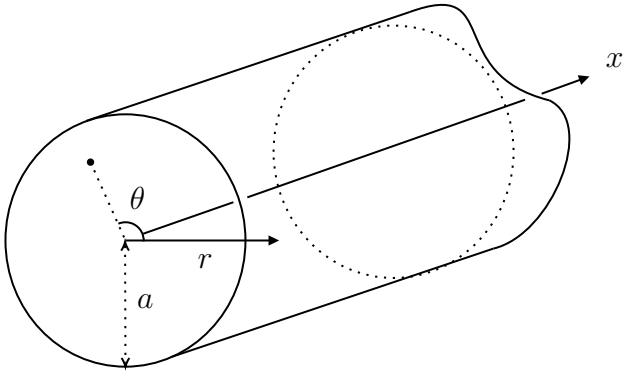

Figure 2.1: Duct coordinate system. The waveguide is infinite in the axial dimension.

frequency. The time variation can be conveniently expressed with the harmonic solution $T(t) = e^{j\omega t}$. What remains is known as the Helmholtz equation, which describes pressure field in the frequency domain

$$\nabla^2 P = -k^2 P \tag{2.4}$$

In the cylindrical coordinate system illustrated in Figure 2.1, $\mathbf{r} = (x, r, \theta)$ and the ∇ operator is given by

$$\nabla^2 = \frac{1}{r}\frac{\partial}{\partial r}\left(r\frac{\partial}{\partial r}\right) + \frac{1}{r^2}\frac{\partial^2}{\partial \theta^2} + \frac{\partial^2}{\partial x^2}. \tag{2.5}$$

The Helmholtz equation can then be solved in cylindrical coordinates with further separation of spatial variables $P(x, r, \theta) = X(x)R(r)\Theta(\theta)$. Substitution of this into equation 2.4 and dividing by r^2/P gives

$$\left(\frac{r^2}{R}\frac{\mathrm{d}^2 R}{\mathrm{d}r^2} + \frac{r}{R}\frac{\mathrm{d}R}{\mathrm{d}r}\right) + \frac{1}{\Theta}\frac{\mathrm{d}^2\Theta}{\mathrm{d}\theta^2} + \frac{r^2}{Z}\frac{\mathrm{d}^2 X}{\mathrm{d}x^2} + k^2 r^2 = 0 \tag{2.6}$$

The full derivation is bypassed by leveraging known solutions. Waves propagating axially in the positive x-direction are expressed as a progressive plane-wave $X(x) = e^{-jk_x x}$ where k_x is the axial wavenumber. Furthermore, periodicity in the azimuthal direction admits solutions of the form

$$\Theta(\theta) = e^{-jn\theta} \quad \text{or} \quad \Theta(\theta) = \cos(n\theta), \quad n = 0, 1, 2... \tag{2.7}$$

Here the first solution represents a helical wave which spirals around the x-axis, with the phase changing according to $(n\theta + k_x x)$. Two such waves spiralling in opposite senses combine to create the latter solution, which represents a standing wave around the circumference [149]. Here, the cosine solution is chosen to represent the θ dependence. Substitution of $X(x)$ and $\Theta(\theta)$ leads to the final ODE describing the radial variation in pressure.

$$\frac{\mathrm{d}^2 R}{dr^2} + \frac{1}{r}\frac{\mathrm{d}R}{dr} + \left((k^2 - k_x^2) - \frac{n^2}{r^2}\right) R = 0. \tag{2.8}$$

This is a modified form of Bessel's equation, which has the solutions

$$R(r) = B_n J_n(k_r R) + C_n N_n(k_r R) \tag{2.9}$$

the latter of which is undefined at $r = 0$ and can be discarded. The solution J_n is the n^{th} order Bessel function of the first kind [150]. The arbitrary amplitude B_n is retained and combined with the circumferential solution to define the transverse 'eigenfunction'

$$\Phi_n(r, \theta) = B_n J_n(k_r r) \cos(n\theta) \tag{2.10}$$

and the pressure field for a single wavemode is expressed as

$$P_n(x, r, \theta) = \Phi_n(r, \theta) e^{-jk_x x} \tag{2.11}$$

Wall Boundary Condition To complete the description of the waves in the system, the radial wavenumber k_r is calculated by considering the boundary conditions at the wall. The axial wavenumber k_x is subsequently solved with the relation

$$k^2 = k_x^2 + k_r^2 \tag{2.12}$$

where k can readily be found at any frequency.

The wall impedance is represented by the dimensionless quantity $\zeta = Z_{\text{wall}}/\rho_0 c_0$, where ρ_0 is the density of the medium. At $r = a$ the no-slip condition is applied, leading to the following relation between pressure and radial acoustic velocity V_r

$$P = \rho_0 c_0 \zeta V_r, \quad V_r = \frac{-1}{jk\rho_0 c_0} \frac{\partial P}{\partial R}. \tag{2.13}$$

where V_r has been expressed with Euler's equation in the frequency domain. Substitution of the solution for the pressure field in Equation 2.11 into the above leads to the characteristic equation

$$J_n(k_r a) - \frac{i\zeta k_r}{k} J_n'(k_r a) = 0 \tag{2.14}$$

which, in general, must be solved numerically at each frequency to find the roots $(k_r a)$ for arbitrary ζ. Two special cases can be identified where the wall impedance is either infinite or zero, which represent the case of a rigid or pressure-release boundary respectively. From either equation 2.14 or 2.13, when $\zeta = 0$ the pressure must vanish at the wall, which is satisfied when $J_n(k_r a) = 0$. For a hard wall, the radial velocity is zero at the wall, requiring that the radial pressure gradient is zero $J_n'(k_r a) = 0$. In each of these cases the roots of the equation are frequency independent, purely real and do not require numerical methods to solve.

When considering the acoustic propagation in a pipe, the wall impedance will be $0 < \zeta < \infty$ and depend on the stiffness of the pipe wall. To properly account for this, a complete model of the structural dynamics of the system, along with the two-way coupling between fluid and structure is required. The fully-coupled system is left to be modelled with finite element methods in later chapters and for now it is assumed that the pipe wall is rigid with $\zeta = \infty$. The validity of this assumption depends foremost on the relative impedances of the fluid and structure. This in turn a function of the material properties, pipe thickness-to-radius ratio and also frequency. In a very thick steel pipe (or borehole), for example, the degree of coupling can be crudely gauged by comparing the ratio of specific acoustic impedances between the fluid and pipe materials, for air, this is 140,000 suggesting that the wall can practically be considered as rigid. For water, this quantity is much lower at 32, indicating that the rigid assumption is less ideal.

With the characteristic equation for rigid walls given by $J_n'(k_r a) = 0$, the (purely real) roots are thus found at the extrema of the given Bessel function, of

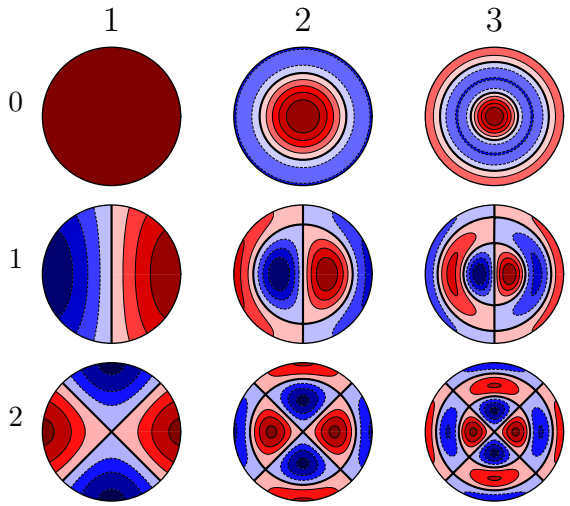

Figure 2.2: Pressure mode shapes of a rigid walled duct, labelled by their mode numbers, n (rows) and m (columns).

which there an infinite number for each n. We denote the m^{th} root of the n^{th} order Bessel function with with

$$\eta_{n,m} = k_r a \quad m = 1, 2, 3... \tag{2.15}$$

The roots are then commonly found by consulting pre-calculated tables or through the use of preferred software routines. In this case, the SciPy package for Python provides the roots. The transverse eigenfunction is now defined for a single mode by the two mode numbers (n, m) such that

$$\Phi_{n,m}(r, \theta) = B_{n,m} J_n(k_r r) \cos(n\theta) \qquad k_r = \frac{\eta_{n,m}}{a} \tag{2.16}$$

Some of the lowest-order transverse mode shapes are plotted in Figure 2.2. The (0, 1) mode stands out as having uniform pressure distribution. This is because the first root of J'_n is zero, leading to $k_r = 0$. This is known as the plane wave and it is functionally identical to its free-space counterpart.

With the solution of the radial wavenumbers, the axial propagation can be considered. Guided waves propagate with the axial wavenumber k_z expressed with

$$k_x = \sqrt{k^2 - k_r^2}. \tag{2.17}$$

When $k > k_r$, the axial wavenumber is purely real and the wave propagates down the x-axis without dissipation. Conversely, where $k < k_r$ the axial wavenumber becomes purely imaginary, and the wave is instead represented by a decaying exponential pressure in the near-field which oscillates time harmonically. This is known as an evanescent wave, which does not transfer energy down the axis and instead is confined near the source which generated it. In the case when $k = k_r$, the axial wavenumber is zero, implying the axial wavelength is infinite, and the mode takes the form of a standing wave in (r, θ) spanning the entire waveguide axis. The frequency at which this occurs is known as the 'cut-on' or 'cut-off' frequency and can be found with

$$\omega_{\text{cut}} = \frac{\mu_{n,m} c_0}{a} \tag{2.18}$$

above which the wave is propagating and below which the wave is evanescent. The cut-on frequency is seen to depend on the mode number, sound speed and radius

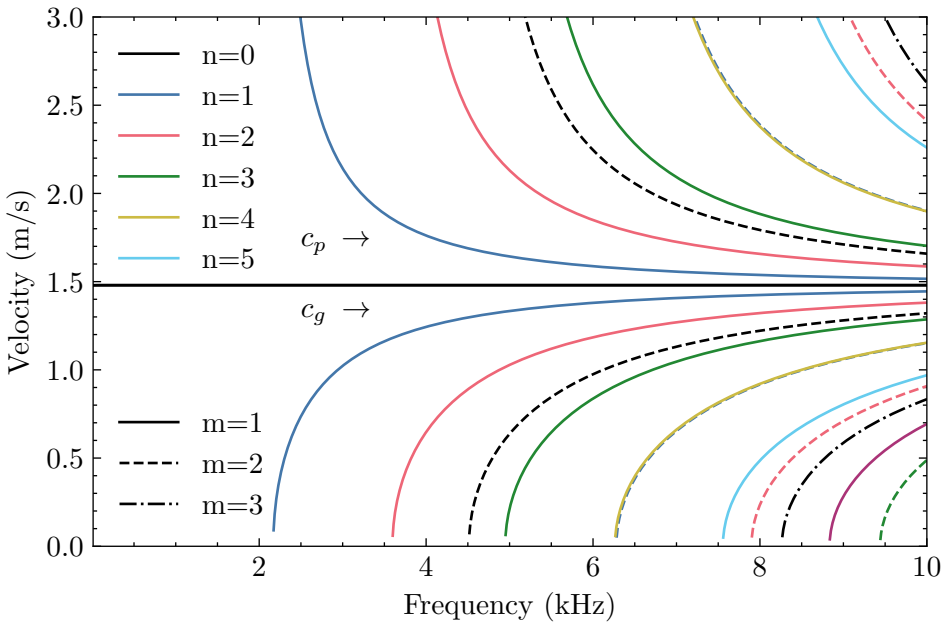

Figure 2.3: Phase and group velocities for a water-filled duct, $a = 0.2$ m

of the duct. For the plane wave the cut-on frequency is zero, indicating that it propagates at all frequencies.

The relationship between the axial wavenumber and frequency is known as the dispersion relation, and is written explicitly for each mode with

$$k_z(\omega) = \sqrt{\left(\frac{\omega}{c_0}\right)^2 - \left(\frac{\eta_{n,m}}{a}\right)^2} \tag{2.19}$$

along with the phase and group velocities given by their respective definitions $c_p = \omega/k_x$ and $c_g = \mathrm{d}\omega/\mathrm{d}k$

$$c_p(\omega) = \omega\left[\left(\frac{\omega}{c_0}\right)^2 - \left(\frac{\eta_{n,m}}{a}\right)^2\right]^{-\frac{1}{2}} \qquad c_g(\omega) = c_0\left[1 - \left(\frac{c_0\eta_{n,m}}{\omega a}\right)^2\right]^{\frac{1}{2}} \tag{2.20}$$

For the plane wave, $\eta_{0,1} = 0$ and so the phase and group velocities reduce to c_0. All higher order modes are dispersive. The phase and group velocities are plotted in Figure 2.3 for a 0.2 m radius water-filled duct. Higher order modes cut on with zero group velocity, where they are purely transverse standing waves. An alternative view to the modal formulation sees the waves as being formed of superimposing pairs of plane waves which are travelling obliquely to the x-axis. As the frequency is increased above cut-on, the group velocity approaches c_0 asymptotically as the waves take an increasingly direct path down the waveguide.

2.1.1 Damping

In the preceding description of the system, propagating waves have purely real wavenumbers and do not attenuate as they travel down the x-axis. This is a direct consequence of the rigid boundary condition, which yields purely real values of $\eta_{n,m}$. The absence of any damping is problematic when modelling the forced response in the waveguide. In the frequency domain, there is an unbounded resonance when exciting at the cut-on frequency of a mode, as energy accumulates in

the transverse standing wave without limit. This manifests as an infinitely long reverberation in the time-domain. Some form of dissipation must therefore be added to the model in lieu of modelling the wall impedance.

Other sources of attenuation in a rigid duct are considered. These could arise from, for example; bulk losses in fluid, scattering from rough walls, interaction with air bubbles, and thermo-viscous losses at the wall.

We assume that the bulk losses are negligibly low, the duct walls are smooth, and there are no gas bubbles suspended in the fluid. Instead, attenuation will be assumed to arise only due to thermo-viscous losses in the boundary layer. This is the region of fluid near the wall where viscosity effects are significant due to the particle velocity rapidly approaching zero at the boundary. A model which incorporates boundary layer attenuation in the plane wave was first proposed by Kirchhoff [151]. Since then, many researchers have developed theories which extend this to the higher order modes in a duct. The most general of these, introduced for example by Dokumaci and Bruneau et al. [152, 153] lead to non-linear dispersion relations which must be numerically solved with a root-finding algorithm. Alternative closed-form solutions have been derived under certain assumptions such as a wide duct with uniform mean flow [154, 155]. In this work the model proposed by Bruneau et al. [156] for wide ducts is used to predict the axial wavenumbers k_x.

The model is valid under the assumption that duct radius is much larger than the boundary layer thickness d, but small enough that bulk losses are insignificant. This is expressed [157]

$$d << \frac{a}{2} << \frac{c_0^2}{\omega^2}\frac{1}{d} \tag{2.21}$$

and the boundary layer thickness is defined as

$$d = \sqrt{\frac{2\mu}{\omega\rho_0}} \tag{2.22}$$

where μ is the dynamic viscosity of the fluid.

In addition to this, the Bruneau model assumes that the duct boundary is 'locally planar' with respect to the acoustic wavelength. Whilst this is not well satisfied at lower frequencies (<≈10kHz), comparison with the more general Dokumaci solutions using the open source package 'acdecom' [158] showed good agreement between the two models over the frequency range studied. The complex axial wavenumbers are calculated as follows

$$k_x^2 = k_x' + (A - \mathrm{i}B) \tag{2.23}$$

where k_x' is the undamped solution calculated with the previous formulation. The parameters A and B are expressed

$$A = 2k\frac{\mathrm{Im}\left(\varepsilon_{n,m}/a\right)}{1-\left(n/\eta_{n,m}\right)^2} \quad B = 2k\frac{\mathrm{Re}\left(\varepsilon_{n,m}/a\right)}{1-\left(n/\eta_{n,m}\right)^2} \tag{2.24}$$

$$\varepsilon_{n,m} = \left(\frac{n^2-\eta_{n,m}^2}{(ka)^2}\right)\beta\sqrt{\mu} + \beta(\gamma+1)\sqrt{\lambda_T M/C}, \quad \beta = \sqrt{\frac{k}{2\rho_0 c_0}}(1+j). \tag{2.25}$$

The relevant thermo-viscious parameters introduced λ_T, M_m, C, and γ, are the thermal conductivity, molar mass, specific heat capacity, and specific heat ratio

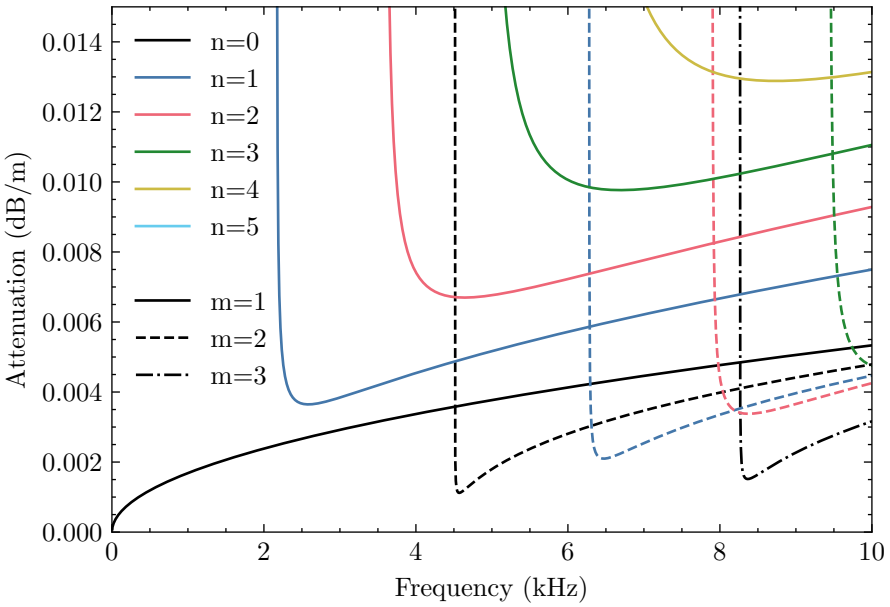

Figure 2.4: Attenuation curves in the duct with only boundary layer losses included through the Bruneau approximate model. [156]

respectively. The γ parameter is set to a value just above 1, due to the fact that water is slightly compressible [159].

With the solution for the complex axial wavenumbers, the attenuation is commonly expressed in the following way

$$\text{Attenuation (dB/m)} = -20 \log 10(\text{e}) \cdot \text{Im}(k_x). \tag{2.26}$$

The attenuation curves using the thermo-viscous Bruneau model are shown in Figure 2.4. These suggest that attenuation is lower for axisymmetric modes, and increases quickly with n for (n, 1) modes. The plane wave solution is identical to the well-known Kirchhoff plane wave. Altogether the attenuation in the duct is low with only boundary layer losses. For example, the plane wave amplitude at 10 kHz is predicted to halve at a distance of 1.2 km.

2.1.2 Monopole Source Expansion

The forced response in the waveguide is formulated with a summation of the orthogonal modes derived in the previous section, which are excited according to the axial velocity source distribution $V_s(r,\theta)$. The general procedure to determine the velocity coefficients involves calculating the inner product between the source term and the radial eigenfunctions

$$V_{n,m} = \frac{1}{\mathcal{A}} \iint_{\mathcal{A}} \Phi_{n,m}(r,\theta)\, V_s(r,\theta)\, d\mathcal{A} \tag{2.27}$$

from which the pressure coefficients follow with

$$P_{n,m} = \rho_0 c_0 \frac{k}{k_x} V_{n,m} \tag{2.28}$$

and the total pressure field is expressed with the modal summation

$$P(x,r,\theta) = \sum_{n=0}^{\infty}\sum_{m=1}^{\infty} P_{n,m}\Phi_{n,m} e^{-ik_x x}. \tag{2.29}$$

For an arbitrary source distribution, determining $V_{n,m}$ may require numerical methods. In the present work the solution is simplified by considering the case of a monopole source, assumed to lie at $x = 0$, $r = r_0$, $\theta = \theta_0$. Thus

$$V_s(r,\theta) = \hat{Q}\delta(\theta - \theta_0)\delta(r - r_0) \tag{2.30}$$

where $\hat{Q}$ is the volume velocity of the monopole, which is constant with frequency and has units of $\mathrm{m}^3\,\mathrm{s}^{-1}$. The resulting pressure field for this excitation can then be written explicitly for $x > 0$ as [160, 161]

$$P(x,r,\theta,\omega) = 2\frac{\hat{Q}\rho_0 c_0}{\Lambda_{n,m}} \sum_{n=0}^{\infty}\sum_{m=1}^{\infty} \frac{k}{k_x} J_n(k_r r) J_n(k_r r_0) \cos(n|\theta - \theta_0|) e^{-jk_x x} \tag{2.31}$$

where the normalisation factor $\Lambda_{n,m}$ for each mode is given by

$$\Lambda_{n,m} = \begin{cases} \pi a^2 J_0^2(\mu), & \text{if } n = 0 \\ \frac{\pi a^2}{2} J_n^2(\mu a)\left(1 - \left(\frac{n}{\mu a}\right)^2\right) & \text{if } n > 0. \end{cases} \tag{2.32}$$

Equation 2.31 gives direct insight into pressure field excited by the source. The presence of k_x in the denominator indicates that the largest response over frequency is at the cut-on of a given mode. In the undamped case, $k_x = 0$ at cut-on and the pressure is infinite. This is avoided with the damping model used, which ensures $|k_x| > 0$ at all frequencies. The $J_n(k_r, r_0)$ term shows the dependence of the pressure amplitude on the radial coordinate of the monopole. For example, if $r_0 = 0$ then each term in the series for which $n > 0$ will evaluate to zero, and only axisymmetric waves are excited.

The modal series in equation 2.31 contains infinite terms. In practice however, the series converges after a given number of terms depending on the frequency of excitation. It is sufficient to use the value M for which $\eta_{0,M} > ka$, and the value of N for which $\eta_{N,1} > ka$, where k is calculated from the maximum frequency of interest.

Parameter		Value	Unit
a	Duct radius	0.2	m
c_0	Fluid sound speed	1480	m/s
ρ_0	Fluid density	1000	kg/m3
λ	Fluid thermal conductivity coefficient	0.6	W/mK
M_m	Fluid molar mass	18	g/mol
C	Fluid specific heat (isobaric)	4200	J/K
γ	Ratio of specific heats	1.002	
μ	Dynamic viscosity of water	0.001	Pa·s

Table 2.1: System parameters of a water-filled duct.

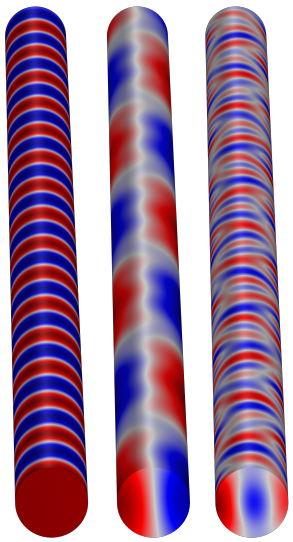

Figure 2.5: Harmonic pressure fields excited by a monopole source located at $x = \theta = 0, r = 0$. For frequencies of 1500, 2200, and 4000 Hz from left to right.

2.2 Harmonic Response

Now a brief description is given of the system's harmonic response when subject to a monopole source, which is positioned at the wall with coordinates $x = 0$, $r = a$, $\theta = 0$. The parameters of the system, chosen to represent a fluid-filled duct of typical intake pipe dimensions, is shown in Table 2.1. The monopole source radiates sound isotropically, and represents the limit of a pulsating sphere approaching zero radius. This approximates the case where an isotropic source is small compared to the shortest wavelength of interest. In this chapter, frequencies up to 40.96 kHz are studied, and in the time-domain the highest frequencies are filtered out to remove aliasing. The minimum wavelength is then between 3-5 cm. The source strength $\hat{Q}$ is set to 1 in all cases for convenience, thus the pressure calculated with equation 2.31 also represents the transfer function $H(x, r, \theta, \omega)$ between the source strength and the pressure at any given point.

$$H(x, r, \theta, \omega) = P(x, r, \theta, \omega) \quad \text{when} \quad \hat{Q} = 1 \, (\mathrm{m}^3 \, \mathrm{s}^{-1}) \tag{2.33}$$

The pressure field calculated with equation 2.31 is visualised over a length of the waveguide for three frequencies in Figure 2.5. At the lowest frequency of 1500 Hz, the response is comprised of only one mode, which is the familiar plane wave with no transverse variation in pressure. As the frequency increases, higher order

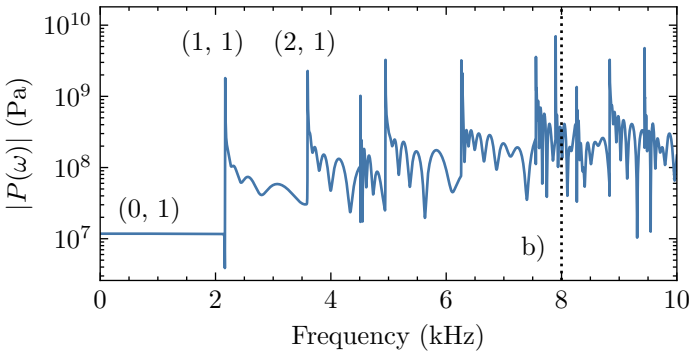

(a) Pressure response with frequency at $x = 5$ m.

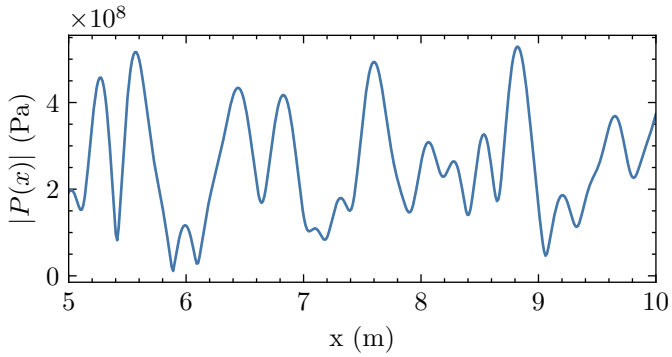

(b) Pressure response with distance at $f = 8$ kHz.

Figure 2.6: The magnitude of the pressure field calculated with equation 2.31, where $r = a$, $\theta = 0$. In a) the pressure spectrum is plotted at a single distance with and the first three propagating modes are labelled. In b) the maximum pressure is plotted down the axis for a single frequency.

waves begin to cut on and the resulting modal interference causes the pressure field to become increasingly complex. This can be seen in the pressure spectrum calculated at $x = 5$ m, shown in Figure 2.6a). Below the first duct cut-on, only the plane wave propagates and the response is flat with frequency. The cut-on of higher-order modes is identified by the sharp peaks in pressure. As more modes propagate and interfere, there is increasing variation in the maximum pressure with both distance and frequency. This is further illustrated in Figure 2.6b), where the maximum pressure is plotted for a single frequency with axial distance. The constructive and destructive superposition of multiple modes leads to regions of very high, and almost zero pressure depending on the axial coordinate.

The full pressure spectrum up to 40 kHz is shown at distances of 50 m and 5000 m in Figure 2.7. Closer to the source, the maximum pressure slowly increases with frequency, due to the increasing number of propagating modes which can constructively interfere, and in contrast to the damping model which predicts higher attenuation with frequency. This latter effect only becomes significant very far from the source, since the system is only very lightly damped. At the maximum frequency of 40 kHz the mode numbers included in equation 2.31 are determined to be $N = 34$, $M = 13$, and over 400 modes are used in the calculation of the pressure field.

We now discuss how to maximise the harmonic pressure. At any given point, there will be an optimal frequency of excitation which elicits the largest possible harmonic response. For simplicity, the transverse coordinates will always be set to

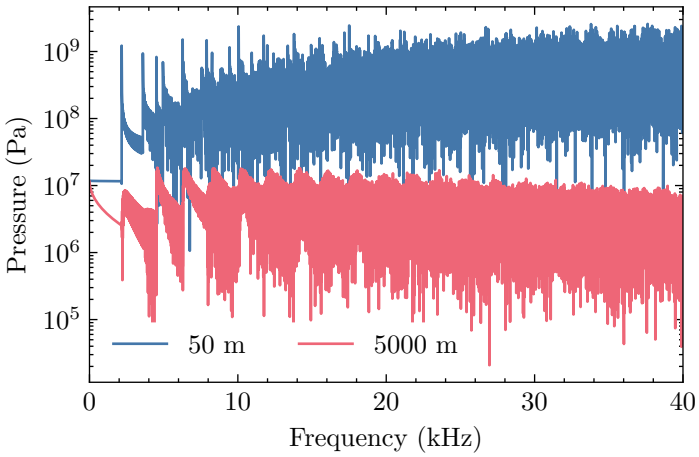

Figure 2.7: Magnitude of the volume velocity to pressure transfer function at $r = a, \theta = 0$, for two distances from the source.

$r = a, \theta = 0$ and the axial coordinate x_f will be referred to as the target (or focal) distance. The peak pressure for a given x_f will typically be found somewhere near the cut-on frequency of a higher-order mode, or may arise due to multiple modes combining in phase. The maximum harmonic response can be expressed as

$$H_{\max}(x_f) = \max\left(|H\left(x_f, \omega\right)|\right). \tag{2.34}$$

As mentioned, $H_{\max}$ is very sensitive to frequency and distance due to multi-modal interference. In a practical setting this makes it challenging to maintain the maximum response at different distances.

Figure 2.8 shows the maximum pressure with distance for a few selected frequencies alongside $H_{\max}$. This outlines the difficulty when seeking an optimal excitation. The frequency $f = 2169$ Hz is the pressure peak associated with the (1, 1) mode, which is first higher-order mode to cut on. Similarly $f = 24926$ Hz represents the cut-on of a much higher frequency mode. In both cases the maximum pressure with a single frequency has large fluctuations with distance, and drops off faster than the optimal excitation calculated with equation 2.34. For $f = 1500$ Hz, only the plane wave propagates and the maximum pressure down the duct is uniform but much lower relative to what can be achieved with the higher-order modes.

2.3 Time Domain Response

Having assessed the system in the frequency domain, we now look to use transient excitations to maximise the pressure at a given point. The objective is to use the dispersive behaviour of the duct to focus energy the target. Before proceeding, the transfer function is first modified to limit the bandwidth of the monopole and thus prevent aliasing in the time domain by filtering out the highest frequencies. The transfer function is henceforth given by

$$H(x_f, \omega) = H'(x_f, \omega)Z(\omega) \tag{2.35}$$

Where $Z(\omega)$ represents a fourth-order, zero-phase Butterworth low-pass filter with cut-off frequency $0.6f_{\max}$, and $H'(x_f, \omega)$ is the unfiltered pressure transfer function at x_f obtained from equation 2.33.

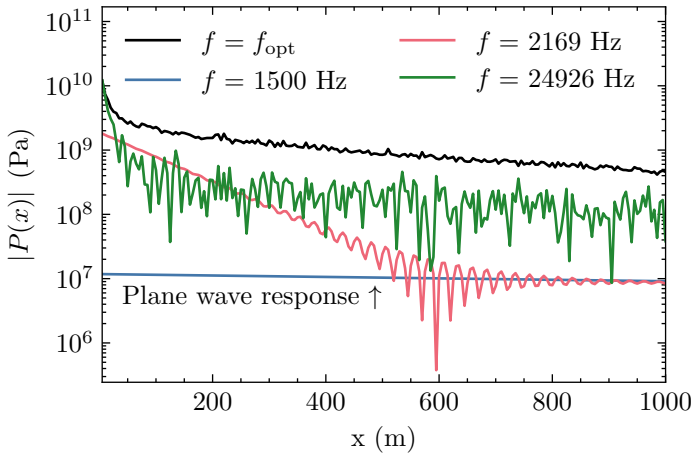

Figure 2.8: Maximum pressure at the wall along the waveguide axis for various excitation frequencies. Also shown is the maximum pressure at the optimal frequency f_{opt}, calculated independently at each distance.

We now consider applying a signal, $u(t)$, which is taken to represent the time-varying monopole source strength. For convenience, this signal will always be normalised such that $|u(t)| < 1$. To calculate the pressure response $g(x_f, t)$ some distance away, one can first convert $u(t)$ into the frequency domain with the Fourier transform

$$U(\omega) = \mathcal{F}\left\{u(t)\right\}. \tag{2.36}$$

The spectrum of the response at x_f can then be expressed

$$G(x_f, \omega) = U(\omega)H(x_f, \omega), \tag{2.37}$$

which can then be converted back into the time domain

$$g(x_f, t) = \mathcal{F}^{-1}\left\{G(x_f, \omega)\right\}. \tag{2.38}$$

In this work, all time-frequency transformations are performed with the discrete fast Fourier transform (FFT). The transfer function is sampled at a number of evenly spaced points between 0 to $f_{max} = 40960$ Hz. The number of samples is varied depending on the desired FFT duration in the time-domain.

2.4 Time Reversal

Time reversal uses the T-symmetry of the wave equation to effectively reverse the propagation step of a wave as it travels from a source to a receiver. Typically a large array of transceivers is used to measure the response induced by a distant excitation, and then simultaneously re-emit the time-reversed version of the measurement. This is known as a time reversal mirror (TRM). If no information is lost then the waves will travel backwards and recreate the source event as if time had been reversed.

In the present work, time reversal is used with a single source and receiver, which is known as single-channel time reversal. As will be seen, using only a single channel can still be very effective in a waveguide such as this because of the way that waves are confined by the boundaries. In the duct, an alternative to the modal description sees the dispersive behaviour as arising from pairs of interfering

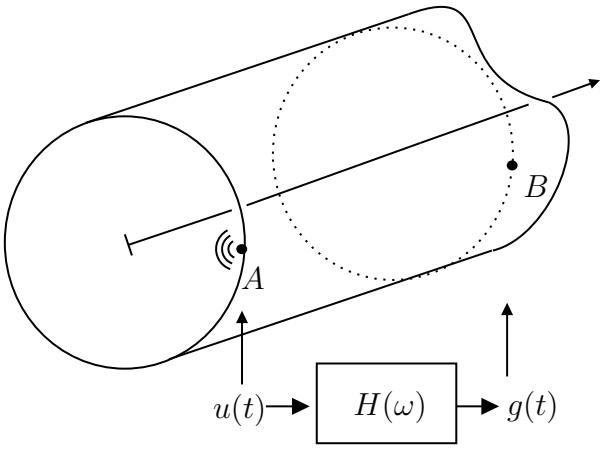

Figure 2.9: Diagram of the transient focussing setup. The monopole is excited at A with a time varying source strength and the resulting pressure response is calculated at B.

plane waves which 'bounce' down the duct via a series of oblique reflections off the walls. From this perspective, the spatial information usually provided with a TRM is instead encoded in the time-domain as an 'echo' or reverberation of the source event. Focussing systems which use high-order scattering in this way are known as 'virtual phased arrays' or 'chaotic cavity transducers'.

2.4.1 Application

Consider the diagram of the problem in Figure 2.9. The monopole source is located at position A, $(x = 0, r = a, \theta = 0)$, where the signal $u(t)$ is applied, denoting the time varying source strength. At some distant point B, located at x_f with the same transverse coordinates, the pressure response $g(t)$ is obtained. If $u(t)$ is the unit impulse

$$u(t) = \delta(t) \tag{2.39}$$

then $g(t)$ is the impulse response function of the system $h(t)$, calculated with

$$h(t) = \mathcal{F}^{-1}\left\{H(\omega)\right\} \tag{2.40}$$

Figure 2.10 shows the impulse response at various distances from the source. Apparent here is the temporal broadening due to dispersion which significantly attenuates the response as energy spreads along the waveguide axis. The pulse is broadband and so contains many frequencies which travel at varying axial velocities. Time reversal then states that applying $h(-t)$ at B be should have the opposite effect, and instead energy will converge as the waves propagate back to the original source at A. In fact, because the wave equation is reciprocal, the system should behave identically if the source and receiver positions are interchanged. With this, $h(-t)$ can instead be applied to the source at A to focus at B. With the source strength limited such that $|u(t)| \leq 1$, the time reversal waveform is expressed

$$u_{\mathrm{TR}}(t) = \frac{h(-t)}{\max(|h(t)|)}. \tag{2.41}$$

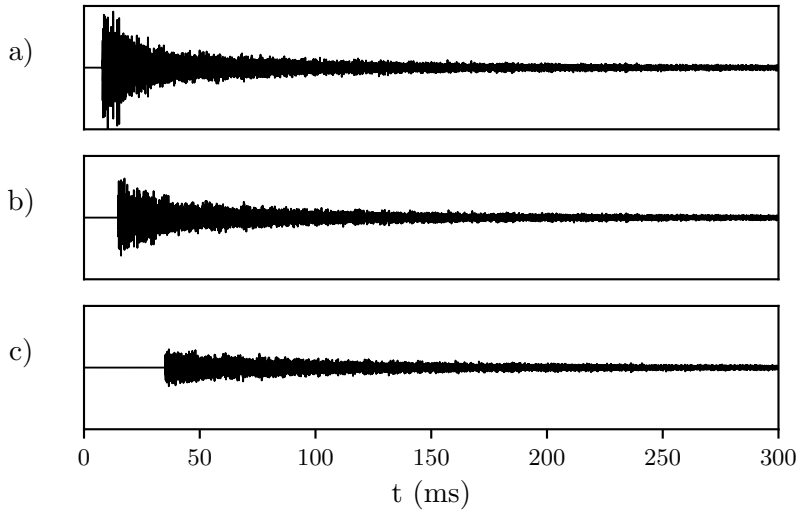

Figure 2.10: The impulse response function calculated at 10, 25 and 50 metres, shown on the same amplitude scale. Spatio-temporal broadening due to dispersion attenuates the response with distance.

which will create a response at B similar to the original impulse applied at A. The response is not a perfect delta function because information is lost when sampling the field with a single transducer.

It is noted that the waveform created with equation 2.41 is generally much less than 1 for most of its duration. In the interest of achieving the largest possible response at B, the amplitude of the waveform can be further modified to increase the signal power of the excitation. A variety of techniques have been explored for this. Montaldo et al. assert that digitising the impulse response over 1-bit theoretically provides the best excitation for the largest response [134]. Experiments by Willardson et al. [141] compared this method to similar techniques, and found applying 1-bit over a certain threshold, known as 'clipping', performed the best. The clipped waveform is expressed

$$u_{\mathrm{CTR}}(x_f, t) = \begin{cases} \mathrm{sgn}(u_{\mathrm{TR}}(x_f, t)), & \text{if } |u_{\mathrm{TR}}(x_f, t)| \geq \epsilon_T \\ u_{\mathrm{TR}}(x_f, t), & \text{otherwise} \end{cases} \tag{2.42}$$

where sgn denotes the sign/signum function and ϵ_T is the threshold value, in this case set to $\epsilon_T = 0.01$. The clipping technique preserves the phase information in time-reversed impulse response but greatly increases the signal power by forcing the waveform amplitude to the largest possible value.

Equations 2.41 & 2.42 are now applied to the impulse response at $x_f = 50$ m to obtain the focal waveforms shown in Figure 2.11. The transfer function is sampled over 2^{17} points and the corresponding duration of the FFT is 1.6 seconds. Both focal waveforms are applied to the monopole source and their corresponding responses in the time domain are shown at the focus in Figure 2.12. The responses have been normalised by the maximum harmonic response at the same distance H_{max}. In both cases, the response is characterised by a large delta-like peak at the focus. With traditional time reversal, the amplification factor compared to the harmonic response at this point, denoted as the 'gain', is approximately 3.2. By contrast, the clipping technique achieves a gain of over 22. Without clipping, the time domain response more closely resembles an ideal impulse, with smaller

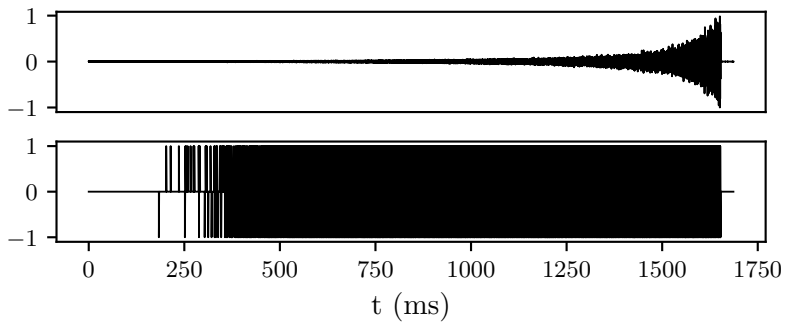

Figure 2.11: Traditional time-reversal waveform (top) and its 1-bit digitised/-clipped counterpart (bottom), sampled from the impulse response at $x = 50$ m. The 1-bit technique significantly increases the power of the input signal.

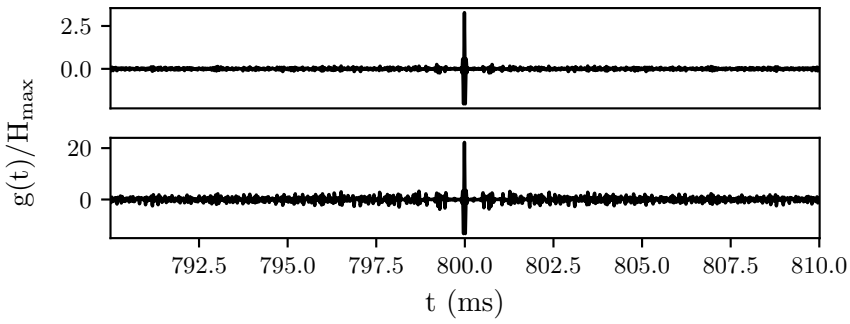

Figure 2.12: Response at the target to the time reversal waveforms illustrated in Figure 2.11.

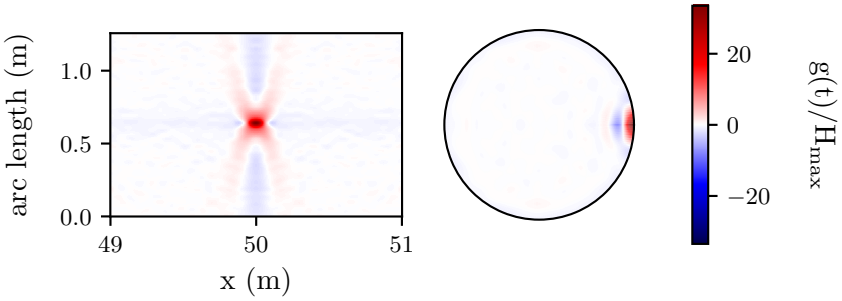

Figure 2.13: Snapshot of the pressure field around the focal point at the time when the response to the 1-bit time reversal waveform is at a maximum.

sidelobes. This is also true of the spatial focal quality. In this work, these characteristics are not important, and only the peak amplitude is of interest. With this, we discard the regular time reversal and all analysis is henceforth performed with the clipping technique. The pressure field around the focus is shown for the peak clipped response in Figure 2.13. By changing the location from which the impulse response is sampled, the focus can be moved to any position in the waveguide. In this case the pressure at the wall is of most relevance. Since the rigid boundary conditions require that the pressure is at a local maximum at the wall, focussing here utilises all propagating modes.

2.4.2 Performance vs Harmonic

To further illustrate the relative advantages of clipped/1-bit time reversal method, the focal distance x_f is scanned down the duct axis. The FFT duration is 1.6 seconds. At each distance, the maximum transient and harmonic pressures are calculated and plotted in Figure 2.14. Also shown is the peak transient response at each distance for a waveform designed to focus at 400 m. The pressure is expressed in decibels with respect to the largest harmonic pressure at the input. With a harmonic excitation, the pressure drops rapidly with axial distance and falls to -20 dB at 40 m. Using time reversal, the maximum transient pressure actually increases with distance above what is achievable harmonically at the source. The maximum transient pressure does not fall below 0 dB until over 600 m from the source. This demonstrates the ability to both amplify the pressure at a given point and extend the range a given pressure can be applied in the duct. When looking at the maximum response down the duct for the 400 m waveform, the pressure naturally peaks at the focal point. However, for a considerable range of distances away from the focus, the transient pressure is still greater than the maximum harmonic response at the same point.

They key differences between the harmonic and transient responses are illustrated by the time domain response shown in Figure 2.15. Here focussing is applied continuously at $x_f = 50$ m. Repeated application of time reversal produces a waveform at the target resembling a pulse train with a fundamental period equal to the duration of the focal waveform, which is the length of the FFT. By contrast, the peak harmonic response is obtained with a continuous sinusoid with a frequency of $f = 10053$ Hz. Whilst the peak transient pressure is much higher when using time reversal focussing, this is accompanied by a drop in the RMS pressure. In Figure 2.15, the RMS pressure of the time reversal pulse train is about one third that of

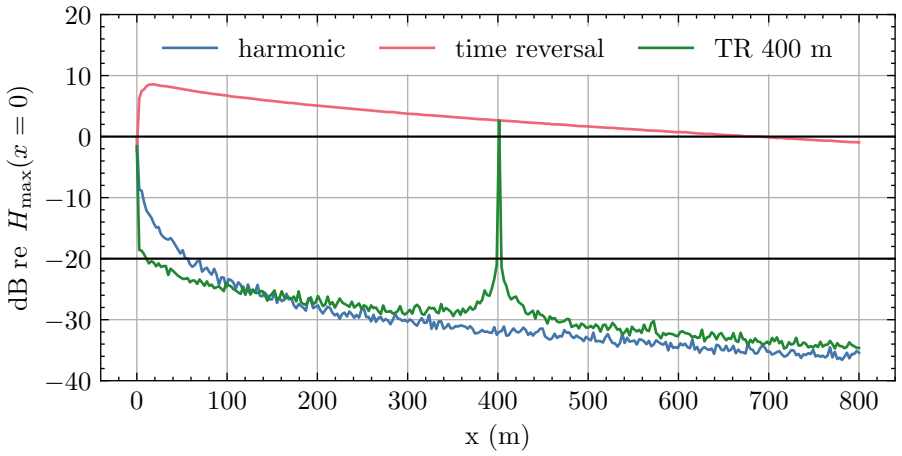

Figure 2.14: Maximum pressure obtained along the duct at the wall ($\theta = 0$), using a harmonic and and transient excitation. For each separate distance, the peak harmonic pressure over all frequencies and the peak transient pressure is calculated. The peak transient pressure is also shown for a waveform designed to converge at 400 m.

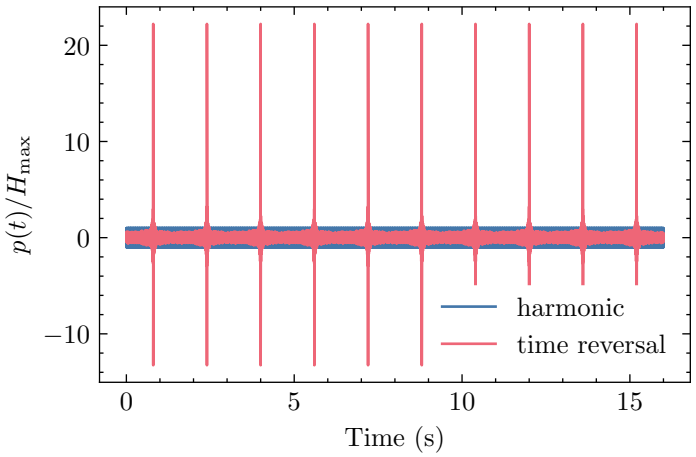

Figure 2.15: Time domain representation of the maximum harmonic and transient responses at the wall at $x = 50$ m. The focal waveform duration and pulse repetition period is 1.6 s.

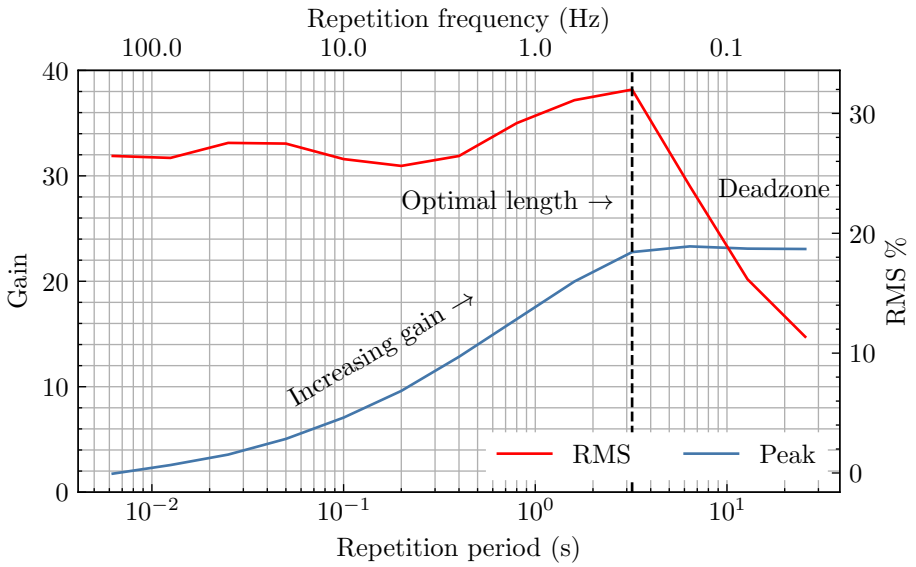

Figure 2.16: How the peak and RMS pressures, as compared to the optimal harmonic excitation, change with the duration of the applied focal waveform. Calculated at $x = 50$ m.

the harmonic response. It is therefore noted that the average power injected into the system is lower for transient focussing.

2.4.3 Pulse Frequency Modulation

The gain yielded using time-reversal depends primarily on the length of the focal waveform. This is determined by either duration of the impulse response, or the maximum length of the FFT. The focal waveform can be deliberately shortened by taking fewer samples of the transfer function over the same bandwidth, thereby reducing the FFT duration. As a result, the peak amplitude at the target is reduced but the pulses can be applied more frequently. Conversely, the FFT can be lengthened to increase the gain up to a point. The maximum gain possible at any point is determined by reverberation time of the system.

Figure 2.16 shows how the peak and RMS pressure relative to the harmonic excitation change when varying the focal waveform duration. The responses are calculated at $x_f = 50$ m. The number of points sampled is increased in powers of two thereby doubling the focal waveform length. The amplitude gain increases monotonically with repetition period until the focal waveform duration reaches 3.2 s. Beyond this, longer excitations do not increase the gain. The RMS pressure also reaches a maximum at the same duration and then rapidly drops.

These results demonstrate the trade-off between the amplitude and repetition frequency of the pulse train response at the focus. This relationship will vary with distance, since the length of the impulse response changes along the waveguide. The reverberation time grows with distance until a point which is determined by the level of damping. In an undamped waveguide for example, the duration of the impulse response would grow without limit with distance from the source allowing unbounded gain when applying time reversal.

Figure 2.17 details this further by showing how the gain and RMS pressure change along the waveguide axis for different focal waveform durations, determined by the FFT length. With increasing distance from the source, the length of the

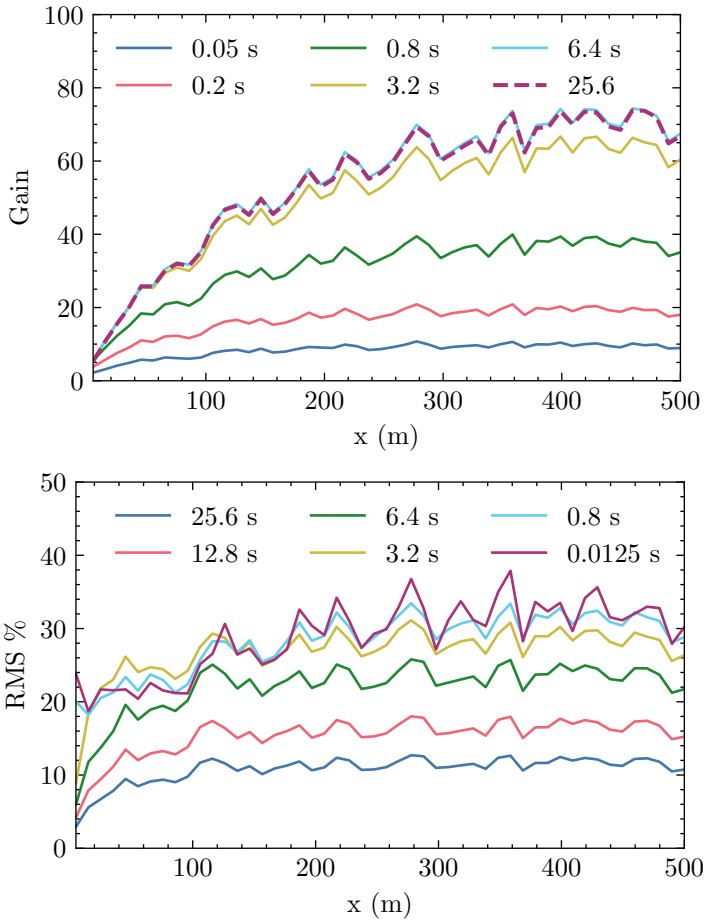

Figure 2.17: Variation of peak and RMS transient pressure with distance, compared to the optimal harmonic excitation, for a number of different focussing waveform lengths.

impulse response grows, allowing for greater focussing potential and therefore gain. This holds until the duration of the impulse response grows longer than the FFT. Beyond this point the gain levels out. This can be clearly seen for $T = 0.05, 0.2, 0.8$ s. Lengthening the FFT further increases the gain up to a point. The gain curves for $T = 6.4$ s and $T = 25.6$ s are identical. For the purpose of focussing, this indicates that the full length of the impulse response has been captured and the maximum gain in the system has been realised. A similar phenomenon is seen with the RMS pressure. Here however, shortening the FFT duration increases the RMS pressure up to a limit. Considering both the gain and RMS curves, a duration of 3.2 s performs the best in this system out of the times studied. Longer than this, and the RMS pressure drops significantly for little increase in gain. Shorter than this, and the gain drops without increasing RMS.

These results indicate there is a maximum waveform duration at which both the gain and RMS pressure peak when applying time reversal. If desired, the waveform can be shortened to increase the pulse repetition frequency with a commensurate reduction in gain.

2.5 Discussion and Conclusions

In this chapter, acoustic propagation in a water pipe was idealised with a model of a rigid walled duct with boundary layer damping. Wave propagation was calculated with the normal mode expansion technique and the free and forced wave behaviour was detailed. The system response to monopole source was modelled with the objective of obtaining the maximum pressure at the duct wall over a long range of distances from the source. This was considered firstly with a harmonic steady-state excitation. Optimising this to achieve the maximum pressure required changing the excitation frequency at each point, due to the multi-modal interference which results in a highly heterogeneous pressure field down the waveguide axis.

Considering instead a transient excitation, the 1-bit or 'clipped' time reversal method was suggested as the technique to maximise the instantaneous pressure at the target. This involved taking the impulse response of the system at the target position, reversing it in time, modifying to maximise the signal power and then applying to the monopole source. After implementing these steps, the higher-order mode dispersion was leveraged to spatially and temporally compress energy at the target, resulting in a high amplitude pulse. Compared to the highest harmonic pressure at the same point, the time reversal method was capable of an amplitude gain of over 30dB. When applying the focal waveform continuously the result is high amplitude pulse train at the target with a fundamental period that is the same length as the focal waveform. The RMS pressure, and therefore the power injected into the system, was found at most to be between 30-40% of that obtained with the optimal harmonic excitation, indicating that the power transfer is reduced in return for amplitude gain. Comparing the harmonic and time-reversed responses over a range of distances from the source, it was shown that the peak time-reversed pressure also drops much more gradually with distance than the harmonic pressure. In fact, at 600 m the peak amplitude achieved with time reversal was comparable with the maximum pressure obtained harmonically at the source.

The relationship between the focal waveform duration and the peak and RMS pressure was investigated. It was shown that the achievable gain is a function of the impulse response duration, or reverberation time. Shortening the focal waveform

allowed for pulses to be applied more frequently at the target but with a lower peak amplitude. Longer focal waveforms increased the gain up to a point, at which the full focussing potential was realised. Increasing the focal waveform duration beyond this did not increase the gain, and only decreased the RMS pressure at the target. It was then concluded that there exists an optimal focal waveform length which maximises both peak and RMS pressure at the target.

3. Axisymmetric Wave Propagation and Focussing in a Fluid-Filled Pipe

In this chapter, the fully-coupled fluid-filled pipe is studied, considering the axisymmetric modes only. The Wave Finite Element method is used to predict wave propagation in the system.

3.1 Introduction

When considering guided waves in piping systems, much of the interest lies in the lowest order circumferential modes. These play a dominant role in the response, particularly at lower frequencies. The axisymmetric (n = 0) case is useful to study in isolation. Aside from being computationally easier, the reduced number of modes propagating axisymmetrically is conceptually more straightforward. Of the four fundamental waves which propagate in a water pipe, the 'plane' acoustic, longitudinal and torsional waves are all axisymmetric. The only other fundamental mode is the $n = 1$ beam bending mode.

The wave behaviour can be characterised as predominantly relating to either the axisymmetric acoustic duct modes or extensional (longitudinal) waves in the pipe wall. The overall level of coupling between fluid and structure is determined by the density ratio of the two materials, and the thickness/radius ratio of the pipe wall. In a thick steel pipe containing air, for example, the acoustic and structural waves can practically be regarded as separate. For a relatively thin steel pipe containing water, however, the fluid coupling significantly affects the wave behaviour.

The axisymmetric pipe system is studied in this chapter with the Wave Finite Element (WFE) method (see Appendix C for the implementation). This is first validated by comparison with results from conventional FE. Once the numerical modelling procedure is established, the behaviour of both a thin and thick pipe are studied. The free waves are first analysed to characterise the modes in the coupled system. The dispersion relation, attenuation and fluid/structure energy distributions are evaluated to provide insight into how power is acoustically/structurally carried down the waveguide axis by each mode.

After this, attention is given to the forced response. Harmonic forcing is applied to the structure with a external radial force, and in the fluid with a centrally located monopole source. The power flow and energy distribution between fluid and structure is evaluated at each frequency. The pressure response of each pipe is then assessed with comparison to a rigid duct, where it is shown that the coupled system increasingly approaches the behaviour of a duct at higher frequencies. Hav-

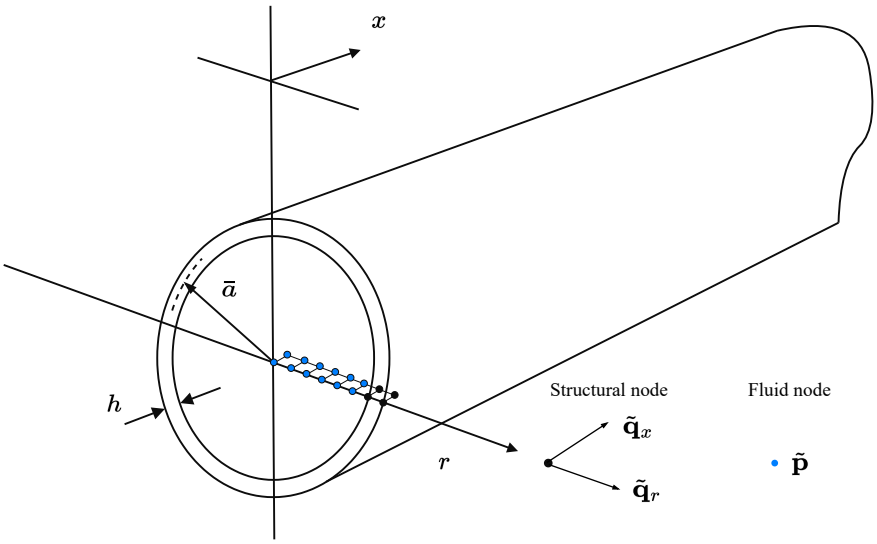

Figure 3.1: Diagram of the axisymmetric infinite fluid-filled pipe system. 2D finite elements discretise the fluid and pipe wall, with degrees of freedom corresponding to the nodal displacements of the structure and pressure in the fluid.

ing assessed the harmonic case, the system can be studied in the time domain to assess transient excitations. Once again, the time reversal method is used to focus energy and instantaneously maximise the quantity of interest at a particular point. Results of focussing in the coupled system are shown to closely resemble those obtained for the rigid duct. Parametric studies are performed to assess the influence of damping, as well as different combinations of forcing and response quantity. The overall objective is to understand how to optimally excite the system for the maximum antifouling impact at different distances from the source.

3.2 Numerical Modelling & Validation

In this section, the numerical modelling procedure is established and validated. The Wave Finite Element (WFE) method is used to predict the wave propagation in an infinite straight steel pipe filled with water. The system is assumed to be uncoupled from any surrounding media. An identical system is also modelled using conventional FE, and the forced response at the input is compared to validate the WFE method.

Figure 3.1 shows a diagram of the system, where the degrees of freedom are $(\tilde{\mathbf{p}}, \tilde{\mathbf{q}}_r, \tilde{\mathbf{q}}_x)$, denoting the pressure and displacement in radial and axial directions respectively. The ring frequency $f_{ring} = c_l/2\pi\bar{a}$, of a water intake pipe is typically between 1-5 kHz [162], where c_l is the extensional plate velocity of the material. This corresponds to a steel pipe radius of 15-80cm. In this chapter, the pipe is chosen to have an inner radius of 20cm, to match the dimensions of the acoustic duct studied in Chapter 2. Hysteretic damping can be added to the structure or fluid with the Young's or bulk modulus respectively

$$E' = E(1 + j\eta_s), \quad B' = B(1 + j\eta_f) \tag{3.1}$$

Practically, η_f can be set to zero, since the dissipation which occurs in the fluid is much lower than in the structure and is not well predicted by hysteretic damping

Parameter	Description	Value	Unit
E	Steel Young's modulus	192	GPa
K	Water Bulk modulus	2.1	GPa
ρ_s	Steel density	7850	kg/m^3
ρ_f	Water density	1000	kg/m^3
η_s	Nominal steel loss factor	0.01	
η_f	Nominal water loss factor	0.0	
h	Wall thickness (thin, thick)	1,4	cm
a_i	Inner radius	20	cm

Table 3.1: Pipe geometry and material parameters. A loss factor of $\eta_s = 0.01$ is used in all cases where not otherwise stated.

in any case. It is noted that this form of damping is only strictly valid in the frequency domain, and can lead to acausal behaviour in the time domain. However, low enough values of η should not significantly affect the response [163]. The wall thickness is studied in the case of either a 'thin' or 'thick' pipe, which respectively are modelled with $h = 1$ cm and $h = 4$ cm. All system parameters are shown in Table 3.1.

3.2.1 Conventional FE Model

Simulating the infinite system with standard FE requires that the waves radiate away at each end of the domain and do not reflect. In this case, absorbing layers with increasing damping (ALID) are used [164, 165] which attenuate waves by gradually increasing the hysteric loss factor away from the waveguide termination. This is implemented in COMSOL by specifying a spatially varying Young's/Bulk modulus. For either the structural or fluid domains, the loss factor from the boundary into the absorbing layer is given by the following expression

$$\eta' = \eta + \frac{3\left|x - x_b\right|^3}{L_a}. \tag{3.2}$$

where η is the loss factor in the propagating region, x_b is the axial coordinate of the termination, and L_a is the length of the absorbing layer. Typically, L_a should be sized to fit at least three wavelengths over all frequencies. This condition can be problematic to satisfy around the cut-on frequency of higher order modes, where the axial wavelength is infinite. Aside from this, longer wavelengths dominate at low frequencies, where the pipe is relatively less mobile to radial forcing.

The thin ($h = 1$ cm) pipe was meshed over a propagating region of 4 m, with absorbing layers of length $L_a = 6$ m at each end. The dimensions used here are for the purpose of validation. Longer waveguides can also be modelled and the absorbing layers can be shortened, depending on desired accuracy. As mentioned however, the computational demand grows rapidly with the length of waveguide. The element size should depend on the maximum frequency of interest. Typically a rule of thumb requires at least 6 (linear) elements per wavelength. Quadratic elements were used, and the size was chosen as 1 cm for a maximum frequency of 20 kHz. The total mesh contains over 50,000 nodes. Each node may have a single DoF in the case of a pressure node or up to three at the fluid-structure interface.

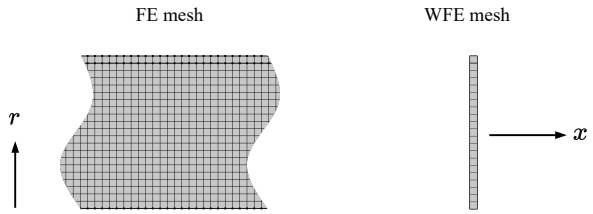

Figure 3.2: Diagram of the mesh in (left) conventional FE & (right) the WFE method. The full FE mesh is regarded as infinite and terminated with absorbing boundaries. The WFE mesh used is created from a single segment of the full FE mesh.

3.2.2 WFE Model

The WFE method is used to model the waveguide with a reduced mesh size, as in Figure 3.2. Here the WFE segment is essentially a single axial slice of the larger FE model. The mass, stiffness and boundary matrices of the segment are extracted from COMSOL with MATLAB LiveLink and then imported into Python where the WFE code is applied to solve for the infinitely repeated system in the wave domain. In the WFE mesh, there are a total of 139 degrees of freedom. The DoFs internal to the left and right faces are dynamically condensed, leaving a 94x94 matrix for which to solve the WFE eigenproblem.

Comparison At $x = 0$ a 1 N radial line force is applied to the external pipe wall in both conventional and wave finite element models. This force acts over the entire circumference of the pipe. A frequency response is calculated over a linear set of 400 frequencies from 1 to 20,000 Hz. Results for the driving point velocity are shown in Figure 3.3. There is good agreement between the two models over most frequencies. The largest discrepancy is found near the ring frequency. It is likely that there are some reflections present in the full FE model which can affect the accuracy, especially near cut-on frequencies. Figure 3.4 compares the spatial pressure field in the pipe at a single frequency of 10kHz. Again, good agreement is shown between the two models. With the accuracy of the WFE model verified, axisymmetric waves in the thin & thick fluid-filled pipes can be analysed for any distance from the source in the infinite system at no additional computational cost.

3.3 Free Wave Propagation

Firstly the free waves are examined in the absence of forcing. In the frequency domain, each guided wave mode propagates axially according to

$$\mathbf{\Phi}_j e^{-ik_j x} \tag{3.3}$$

where $\mathbf{\Phi}_j$ is the cross-sectional mode shape, in this case an eigenvector corresponding to the degrees of freedom on one face of the WFE segment. Each eigenvector contains the generalised displacements and forces

$$\mathbf{\Phi}_j = \begin{bmatrix} \tilde{\mathbf{q}} \\ \tilde{\mathbf{f}} \end{bmatrix}_j \tag{3.4}$$

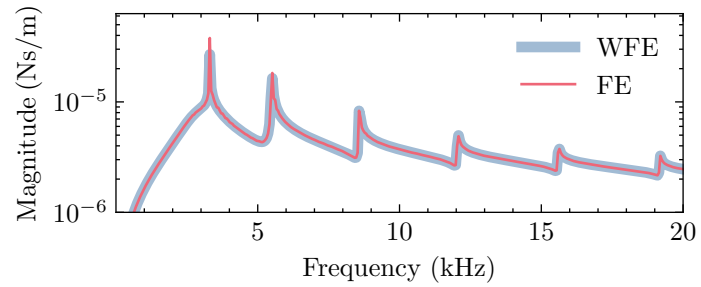

(a) magnitude

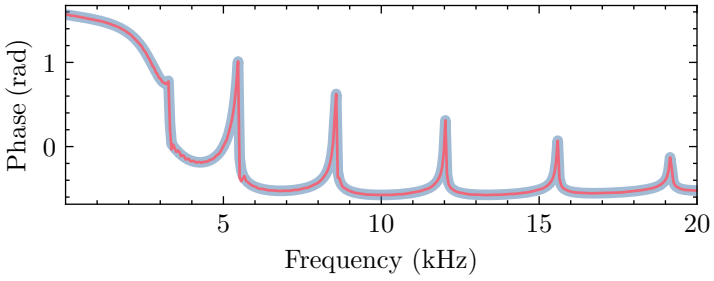

(b) phase

Figure 3.3: Comparison between results obtained with conventional and wave finite element methods for the radial driving point velocity of the pipe wall subject to a 1N line force.

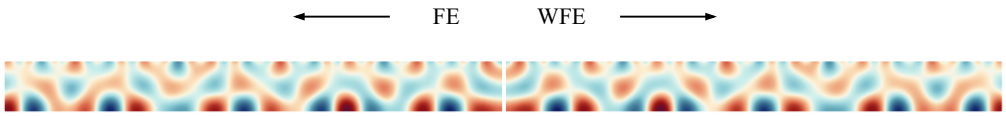

Figure 3.4: Comparison of the pressure field in the FE (left) and WFE (right) models at a frequency of 10kHz. The field is calculated between 0-2 m from the source.

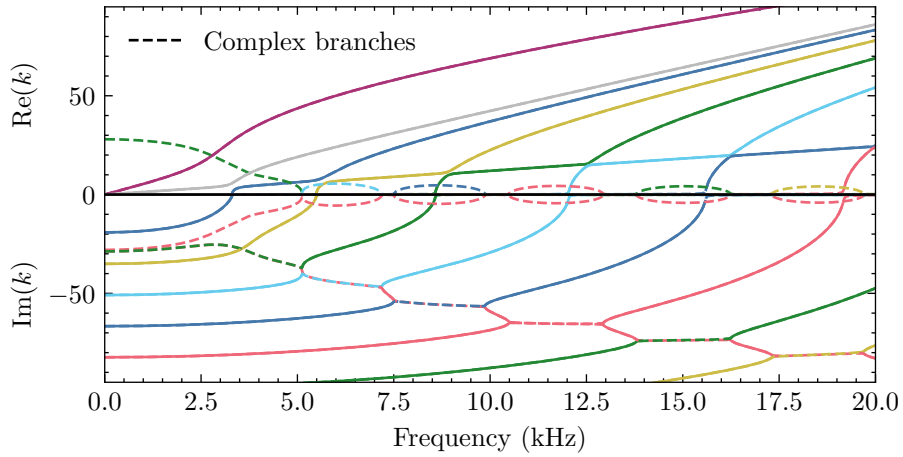

Figure 3.5: Right-going wavenumber spectrum of the thin fluid-filled pipe system, real, imaginary and complex branches of the dispersion relation, representing propagating, evanescent and attenuated waves

which are in turn comprised of structural and acoustic degrees of freedom.

$$\tilde{\mathbf{q}}_j = \begin{bmatrix} \tilde{\mathbf{q}}_r \\ \tilde{\mathbf{q}}_x \\ \tilde{\mathbf{p}} \end{bmatrix}_j \qquad \tilde{\mathbf{f}}_j = \begin{bmatrix} \tilde{\mathbf{f}}_r \\ \tilde{\mathbf{f}}_x \\ \tilde{\mathbf{Q}}_A \end{bmatrix}_j \tag{3.5}$$

The axial propagation is described by the axial wavenumber k_j. Ignoring the modal amplitudes, the free wave propagation can be directly studied from the characteristic solutions of the WFE eigenproblem, which yield the mode shapes, dispersion relation and attenuation of each wave.

3.3.1 Dispersion

The axial propagation of each wave is characterised by the dispersion relation, $k(\omega)$. Whilst the frequency is always real, the wavenumber of any given mode in the undamped system may be purely real, purely imaginary or complex. In any system with damping, all wavenumbers will always be complex. Figure 3.5 shows the dispersion relation for the undamped thin pipe. The waves are sorted with the wave assurance criterion (WAC) [166] which tracks the solutions over frequency by their modal similarity at adjacent frequencies. Real, imaginary and complex waves are all present in the system. However, in practice the interest is in those which are strongly propagating with a small Imag(k). The imaginary wavenumbers are only important when evaluating the response near the source, as they represent rapidly decaying near-field disturbances.

The dispersion relation is used to derive the phase and group velocities. With this, we concentrate only on the propagating modes. Figure 3.6 shows these for the thin & thick pipe. Commonly these modes are denoted by $s = 1, 2, 3...$ and are ordered by their cut-on frequency. Of the two fundamental modes, $s = 1$ (also known as $L(0,1)$ or α) denotes the fluid dominated mode, which, at low frequencies, corresponds to the plane wave in a rigid duct. The $s = 2$ mode is also fundamental, and corresponds to the compressional rod wave.

In the thin pipe, the main three distinct types of wave behaviour are identified by their velocity asymptotes. The fluid dominated wave has a phase and group

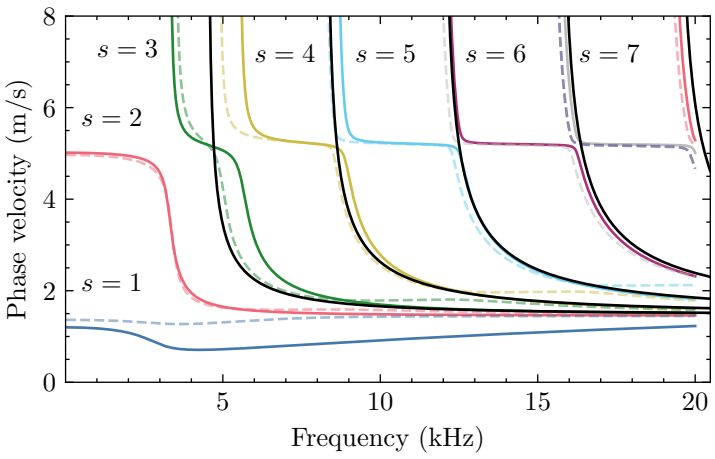

(a)

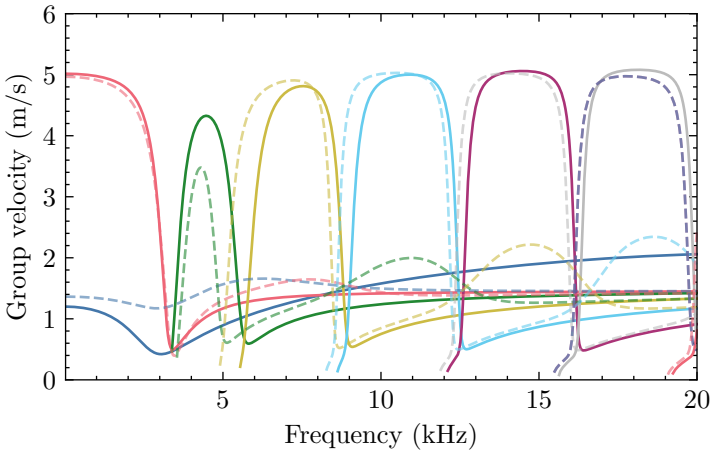

(b)

Figure 3.6: (a) Phase and (b) group velocities for the thin (solid) and thick (dashed) pipe systems. Also shown in black are the phase velocity curves for the rigid duct.

velocity close to the sound speed in water at low frequencies. Above the ring frequency at 4 kHz, the mode changes its behaviour to a plate like (S0 lamb) wave in the pipe wall. The $s = 2$ is essentially the extensional rod wave below the ring frequency until it switches to an acoustic plane wave at high frequency. All higher order modes generally alternate their behaviour between duct and extensional shell-type modes. For comparison, the phase velocities of axisymmetric waves in a rigid duct are also shown in 3.6. At cut-on, particularly with a thin pipe wall, the fluid-structure coupling is high and the waves cannot easily be characterised as either predominantly structural or acoustic. This will become clearer by evaluating the energy distribution of each wavemode.

The thick pipe exhibits broadly similar velocity curves as the thin pipe. Note that here the $s = 1$ mode is less affected by the pipe coupling near the ring frequency, owing to the increased stiffness of the pipe wall, and behaves mostly as a plane wave in a rigid duct. This is indicated by the lower level of dispersion. At higher frequencies, the acoustic modes briefly visit one additional asymptote in the thick pipe, which is the aforementioned S0 plate solution in the pipe wall. This coupling does not occur in the thin walled pipe, since the phase velocity of

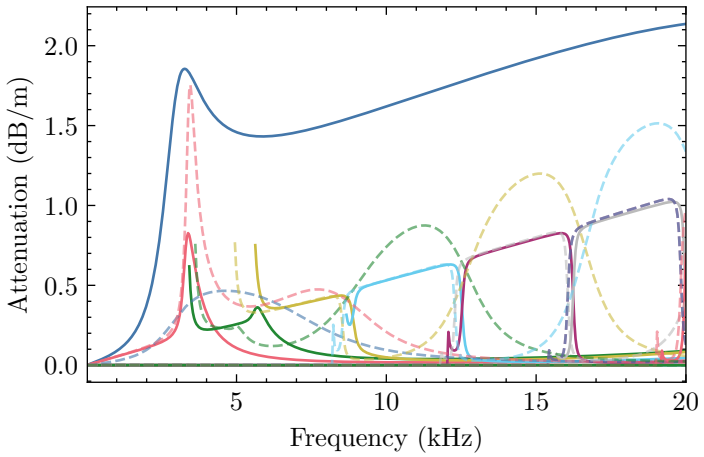

Figure 3.7: Attenuation for the thin (solid) and thick (dashed) pipe systems

this wave remains below the speed of sound over the bandwidth studied. In the thick pipe however, the phase velocity of the S0 wave in the pipe wall crosses the phase velocity of sound in the fluid, and coupling can occur.

3.3.2 Attenuation

The dispersion relation also predicts the attenuation of each mode where damping is used. This is given by the imaginary part of the wavenumber and is commonly expressed in decibels per metre

$$\text{Attenuation (dB/m)} = -20 \log 10(\text{e}) \cdot \text{Im}\,(k)\,. \tag{3.6}$$

The attenuation is shown in Figure 3.7. In the thin pipe, the attenuation follows the three main asymptotes as before, corresponding to predominantly flexural, extensional, and acoustic modes in order of highest damping. The fluid dominated mode is significantly attenuated near the ring frequency, due to the strong coupling with the structure. Generally speaking acoustic modes are least attenuated. This is understood by the fact that the fluid is undamped and so dissipation must arise through coupling with the structure only. Where the pipe appears stiff to the acoustic waves, there is little attenuation of the fluid waves, which decreases even further with frequency as the duct modes take a more direct path down the axis and approach the velocity of an acoustic plane wave.

In the thick pipe, by contrast, the stiffer pipe wall couples far less with the fluid dominated mode, which behaves comparatively closer to a pure acoustic wave. Corresponding to the asymptotes in seen in the velocity curves, additional peaks in attenuation are seen at higher frequency for acoustic modes where fluid-structural coupling increases once more due to coincidence with the S0 wave. Generally speaking, we see that waves in the thicker pipe are more attenuated due to the increased coupling. However, this is assuming the pipes are not immersed in any surrounding media, and have no other structural constraints such as flanges or supports. Buried pipes, for example, are expected to have much higher levels of attenuation.

3.3.3 Energy Distribution

To understand how the power is distributed through the structure and fluid, the energy ratio is calculated for each propagating mode in the pipe. First the power flow is calculated in the structure. For the eigenvector of the jth mode $\mathbf{\Phi}_j$, we extract the elements which are associated with radial and axial displacements in the pipe wall. These quantities are axisymmetric and given in the usual units of m and N respectively. The total mechanical power for each mode is then the sum of the powers in each mechanical degree of freedom calculated as

$$P_j^s = \frac{1}{2}\,\text{Real}\left([\tilde{\mathbf{f}}_r^T, \tilde{\mathbf{f}}_x^T]_j^* \begin{bmatrix}\tilde{\dot{\mathbf{q}}}_r \\ \tilde{\dot{\mathbf{q}}}_x\end{bmatrix}_j\right) \tag{3.7}$$

where * denotes the complex conjugate and the velocities are found in the frequency domain with $i\omega[\tilde{\mathbf{q}}_r, \tilde{\mathbf{q}}_x]^T$

The total acoustic power is calculated by integrating the axial intensity over the fluid cross-section. To find this, the particle velocity in the axial direction is required. This is related to the gradient of pressure $\partial\tilde{\mathbf{p}}/\partial x$ by the linearised momentum equation

$$\tilde{\mathbf{v}}_x = -\frac{1}{i\omega\rho}\frac{\partial\tilde{\mathbf{p}}}{\partial x} \tag{3.8}$$

where it is noted that the pressure gradient down the axis is given by $-ik_j\tilde{\mathbf{p}}$. For a given mode, the axial intensity can be evaluated at each acoustic degree of freedom

$$\mathbf{I}_x = 0.5\,\text{Real}(\tilde{\mathbf{p}} \circ \tilde{\mathbf{v}}_x^*) \tag{3.9}$$

where $\circ$ represents element-wise multiplication of the nodal pressures and axial particle velocities. To then evaluate the total acoustic power flow in a given mode, the axial intensity is integrated over the cross-section. There is no circumferential variation in the pressure field, therefore

$$P^f = \int_0^{a_i} 2\pi r\,\mathbf{I}_x dr. \tag{3.10}$$

and the total acoustic power flowing in each mode is thus

$$P_j^f = \int_0^{a_i} \text{Real}\left(\frac{k_j}{\rho_f\omega}\tilde{\mathbf{p}}_j^2\right)\pi r\,dr. \tag{3.11}$$

where the integral is evaluated numerically over the nodes of the WFE mesh. The structural/acoustic power flows are calculated for each mode at any given frequency. The energy ratio between fluid and structure is defined as

$$E_r = P^f/P^s \tag{3.12}$$

Figure 3.8 shows the free-wave energy ratios for the propagating modes. For the thin pipe, the power of each mode is generally either almost completely in the fluid or structure. The fundamental modes switch behaviour near the ring frequency, with the $s = 1$ tending to a flexural wave and the $s = 2$ mode tending to an acoustic plane wave thereafter. The higher order modes all exhibit similar behaviour, cutting on as duct modes, then switching to extensional modes with low fluid coupling, then veering back to the acoustic solution at high frequency. For each of these modes, there is a point where the power is evenly distributed

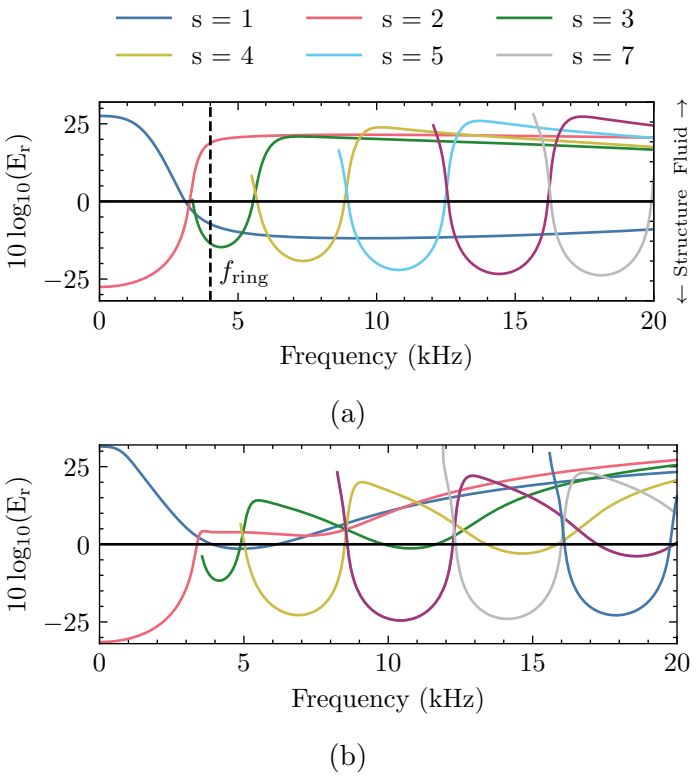

Figure 3.8: Free wave power ratios for each propagating mode in the (a) thin and (b) thick pipe

between the structure and fluid, and where the degree of coupling is expected to peak.

The thick pipe bears significant differences in the power ratio. The $s = 1$ mode is no longer primarily structural in the high frequency limit, and instead most of the energy remains in the fluid apart from a small bandwidth around the ring frequency. This also indicates that the solution is no longer comparable to a flexural wave in the pipe wall as in the thin pipe. By contrast, $s = 2$ retains more energy in the structure for a thick pipe. For the higher order modes, there are now two regions for each branch where the energy is mostly in the structure. This is due to the additional coupling of the fluid with the S0 wave, as mentioned before.

3.4 Forced Response

Now the response of the system to harmonic forcing is evaluated. A structural and acoustic excitation is chosen to characterise the response in each case.

Acoustic Excitation For the acoustic excitation, a unity strength monopole source located at $x = r = 0$ is used. For any predominantly acoustic mode in the axisymmetric system, the pressure will be at a maximum at the centre of the pipe. This makes the chosen source suitable for exciting all waves of interest. An alternative excitation would be to use an axisymmetric acoustic line source for $r > 0$. However, this will not yield meaningfully different results to a centrally placed monopole and so is ignored here. The input to the WFE model is the right

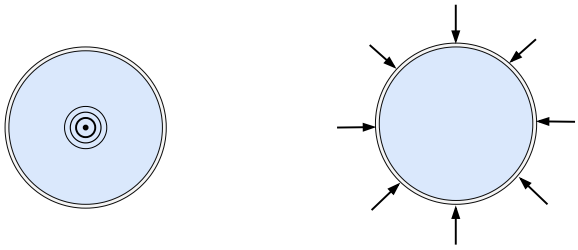

Figure 3.9: The two types of forcing applied to the system in this chapter. The monopole (left) excites the fluid directly whereas the radial ring force (right) is applied to outer wall of the structure

hand side of the inhomogeneous Helmholtz equation [157].

$$\nabla \cdot \left(-\frac{1}{\rho_f} \nabla p \right) - \frac{k_f^2 p_{\mathrm{t}}}{\rho_f} = \frac{4\pi}{\rho_f} S\delta\left(x\right), \quad S = \frac{i\omega\rho_f}{4\pi} Q_{\mathrm{S}}. \tag{3.13}$$

where Q_s is the monopole source strength in m^3/s. The response to constant input of $Q_s = 1$ can then be found by setting the RHS of this equation, and the WFE input to unity, and subsequently multiplying all calculated response quantities by $i\omega$. In practice, an acoustic transducer in the fluid will not behave as a perfect point source and will also exhibit a dependence on frequency. In lieu of modelling any specific actuator we shall proceed with the monopole source, being mindful of any assumptions which are prone to breakdown, particularly at higher frequencies.

Structural Excitation The structural excitation used for in this chapter is a unity strength radial line source acting on the outer wall of the pipe. This means 1N acts over the entire outer pipe circumference. This is assumed to be the best available way of forcing the structure to excite structural waves with predominantly radial motion, and acoustic waves which are coupled with this motion. The main assumption is that the applied force is independent of frequency. With any real actuator, frequency dependent characteristics of the actuator itself as well as the dynamics of the pipe will lead to deviations from this assumption. Still, many commercial inertial actuators behave approximately as ideal force sources above their resonant frequency as long as the system being driven has significantly higher mechanical impedance than the actuator itself.

3.4.1 Input Power Distribution

The input power ratios are determined for the acoustic and structural excitations in both pipes. This describes the distribution of input power between the fluid/structure at each frequency. In the absence of damping, these ratios are independent of distance from the source. The input power ratios are important in assessing how to excite the pipe to achieve the most power in either the fluid or the structure, depending on application. For example, if the fluid is expected to carry waves with lower attenuation it is beneficial to understand how to inject the maximum power into the fluid and not the structure.

The input power is found first calculating the excited amplitude $\tilde{e}_j$ of each mode for the given excitation as described in Appendix C. Then equations 3.7

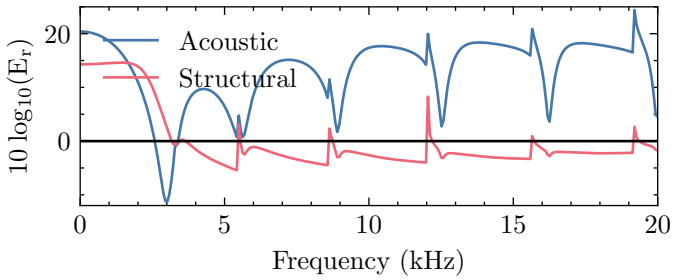

Figure 3.10: Input power ratio the thin pipe with acoustic/structural forcing

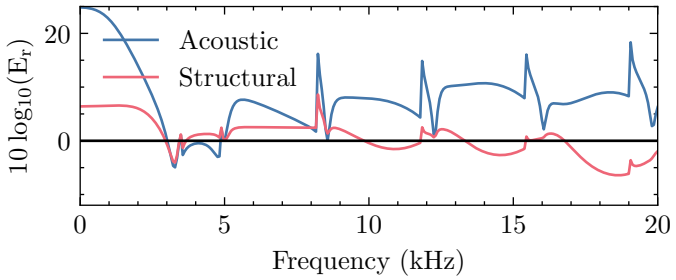

Figure 3.11: Input power ratio the thick pipe with acoustic/structural forcing

& 3.11 can be applied with the scaled eigevectors $\tilde{e}_j \mathbf{\Phi}_i$. The total power for an applied excitation is then found by superposition over all modes with

$$P_0^{\mathrm{f,s}} = \sum_{j=1}^{N} \tilde{e}_j P_j^{\mathrm{f,s}} \tag{3.14}$$

Figures 3.10 & 3.11 show the input power ratios for the chosen excitations in both thin and thick pipes. As would be expected, the monopole source preserves most of the energy in the fluid in both systems. The exception is a small region around the ring frequency where the coupling increases with the radial compliance of the pipe wall. Above this, the power ratio is controlled by the duct type modes, which are mostly fluid based. At higher frequencies there are sharp peaks in the acoustic power as the duct modes resonate at cut-on, and then a sharp increase in structural power as they reach a coincidence with the *in vacuo* $L(0,2)$ mode. Beyond this, energy returns mostly to the fluid for each duct mode as it approaches the velocity of the acoustic plane wave. The force source injects power primarily into the structure above the ring frequency in the thin pipe. The exception is around the cut-on frequencies of the duct modes, where high coupling shifts the power distribution toward the fluid.

Whilst the situation is broadly comparable in the thick pipe, the energy distribution shifts decidedly towards the structure for an acoustic source, and towards the fluid for a structural source. Overall the power flow is more evenly distributed, and the behaviour is less easily characterised by purely extensional/duct waves.

3.4.2 Transferred Power & Distribution

In an undamped system, the average axial power flow is constant, and is equal to the input power. In this case, the energy distribution in fluid & structure

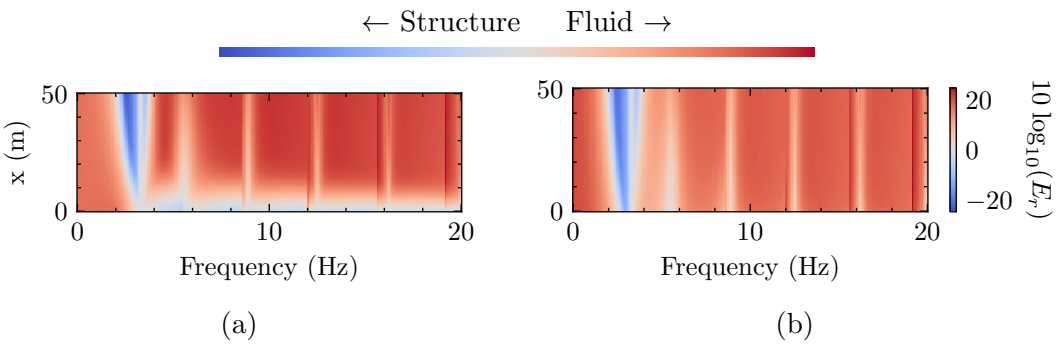

Figure 3.12: Fluid/structure energy ratio with frequency and distance from the source for the thin pipe. (a) Structural excitation (b) Monopole Excitation

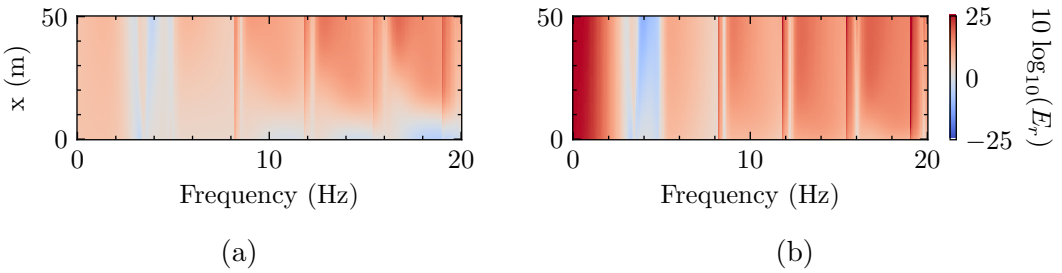

Figure 3.13: Fluid/structure energy ratio with frequency and distance from the source for the thick pipe. (a) Structural excitation (b) Monopole Excitation

is fixed at a given frequency and does not change as waves propagate down the pipe. When damping is considered, this no longer the case, as certain modes will experience varying levels attenuation, and the power distribution will shift accordingly. Naturally, it is expected that energy distribution will shift to the fluid since structural damping is the only mechanism for energy dissipation in this model.

To calculate the transferred power, equation 3.14 is applied once again but now each mode is propagated down the waveguide axis by $e^{-ik_j x}$. This allows the power in either the fluid or structure to be calculated for a given axial distance.

$$P^{\mathrm{f,s}}(x) = \sum_{j=1}^{N} \tilde{e}_j P_j^{\mathrm{f,s}} e^{ik_j x} \tag{3.15}$$

Figures 3.12 & 3.13 show the energy distribution up to 50 m from the source. The $x = 0$ slices of these plots correspond to the input power ratios presented in Figures 3.10 & 3.11. Immediately clear is that the fluid is dominant in transferring power over most frequencies at any considerable distance from the source. The main exception is the region near the ring frequency. In the thin pipe, when driven with a ring force, the power is found mostly in the structure close to the driving point. By $x = 10$ m however, the power dissipation dictates that much of this energy is lost due to the hysteretic damping in the structure.

As before in the thick pipe, the power is generally more evenly distributed between the fluid and structure. The exception is below the ring frequency for a monopole source, where the low level of fluid coupling in the relatively stiffer pipe leads to a much greater proportion of power remaining in the fluid.

To conclude the power flow analysis, the total axial power flow at $x = 0$ & 50 m is shown in Figures 3.14 & 3.15 for the structural and acoustic excitations re-

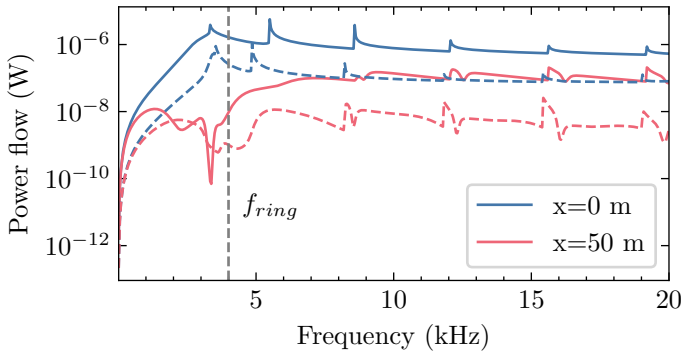

Figure 3.14: Total power flow for the (solid) thin and (dashed) thick pipe at $x = 0$ and $x = 50$ when driven by a radial ring force

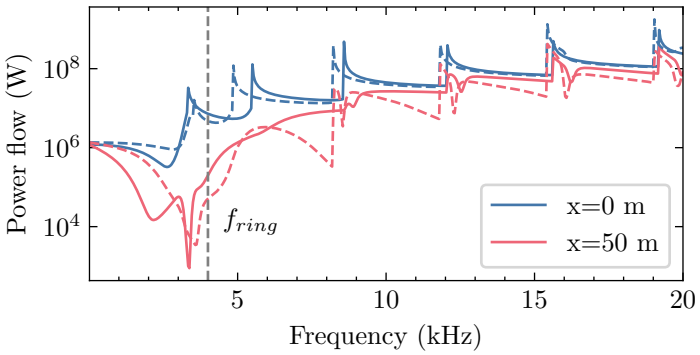

Figure 3.15: Total power flow for the (solid) thin and (dashed) thick pipe at $x = 0$ and $x = 50$ when driven by a central monopole source

spectively. Correspondingly, the power loss between these two distances is plotted in Figure 3.16. Here we see that around the ring frequency, whilst the input power is high, so is the attenuation and such waves contribute negligibly to the response at long range. The power flow is greater at higher frequencies and also less attenuated. Close to 0 Hz, there is also little attenuation, however with a structural excitation, the total power injected is also very low due to the relative stiffness of the pipe. By contrast there is no such limitation with an acoustic source and the acoustic plane wave may be readily excited close to 0 Hz where it will experience very low of levels of attenuation in the pipe which is almost rigid at this frequency. Whilst this demonstrates that harmonically the acoustic plane-wave may be used to carry energy far from the source below the ring frequency, this wave is relatively non-dispersive and so its use will not be significantly enhanced by the application of time reversal focussing. Between the structural and acoustic excitations more broadly, the latter will excite waves which suffer relatively lower levels of attenuation at distance.

3.4.3 Rigid Duct Comparison

As mentioned, the fluid-filled pipe system will increasingly behave like a rigid duct as the frequency increases above the ring frequency. To demonstrate this, the analytical duct model from Chapter 2 is compared to both the thin and thick pipes when driven by a central monopole source. The transfer functions calculated

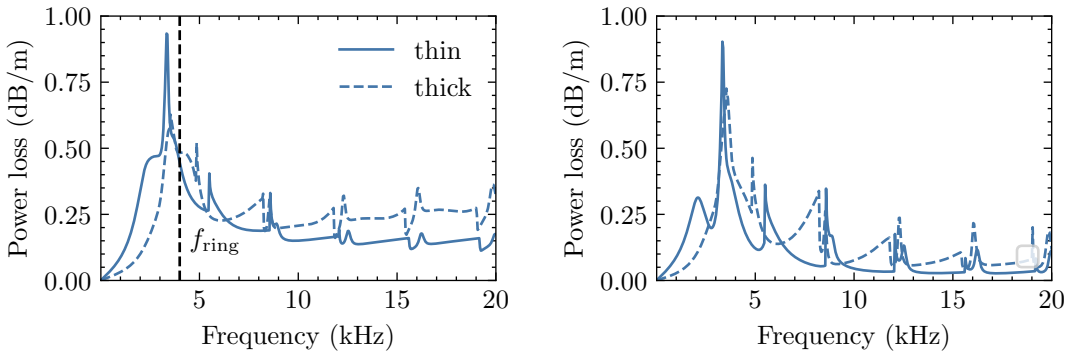

Figure 3.16: Power loss per metre vs frequency at $x = 0$ and $x = 50$ when excited by a) structural force b) central monopole

at $x = 1$ m and $x = 100$ m are plotted in Figure 3.17. The pressure response is comparable at high frequency between all three systems. The main discrepancy occurs near the ring frequency where the structure resonates radially and the power dissipation is high due to structural damping. With increasing frequency, the pipe becomes comparably stiffer and behaves more as a rigid boundary. This can be seen by the growing similarity between the pressures in the three systems. Below the ring frequency, the thicker pipe shows less attenuation of the plane wave. Once again this is arises due to the decreased coupling of fluid and structure where the pipe wall is thicker.

Taken together with the total power flow and attenuation, this result demonstrates that the pipe system can be regarded as behaving close to a rigid duct in the frequency range where the power transmission at long range is generally highest. It is then suggested that the results seen for the rigid duct will generally hold in the coupled system above a particular frequency. Furthermore, when time reversal is applied, it is the higher order acoustic modes which allow energy focussing due to their dispersive nature and it is these modes which are most comparable to the rigid duct counterpart.

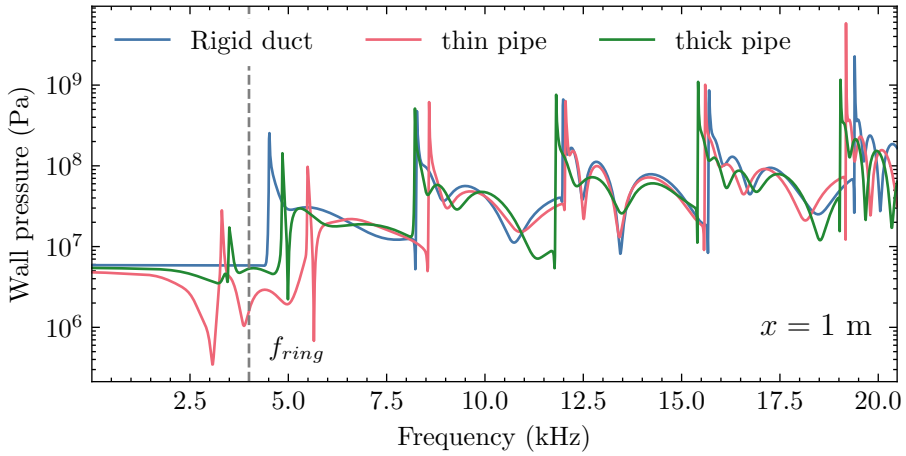

(a)

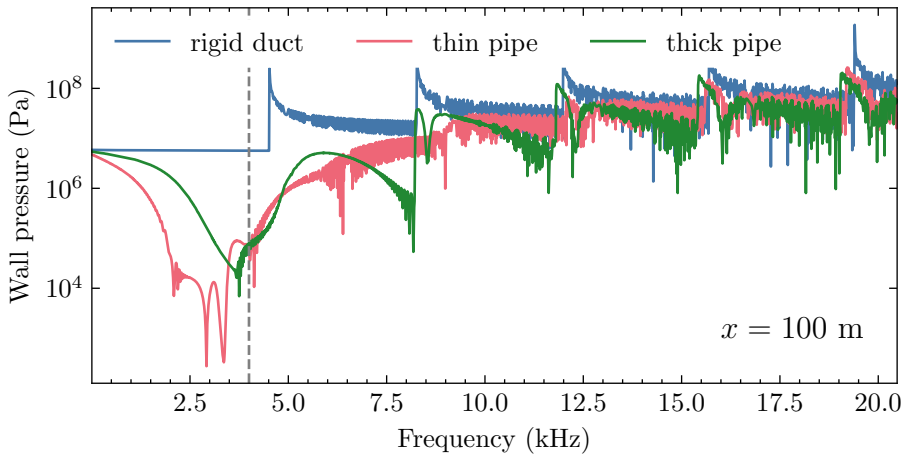

(b)

Figure 3.17: Volume velocity to pressure transfer function for a rigid duct and the thick/thin pipes at $x = 1$m and $x = 100$ m

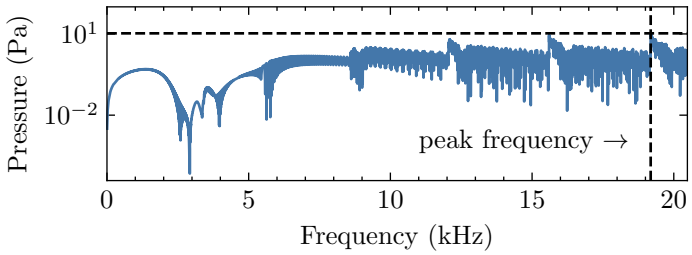

Figure 3.18: Force to wall pressure transfer function at $x = 50$ m

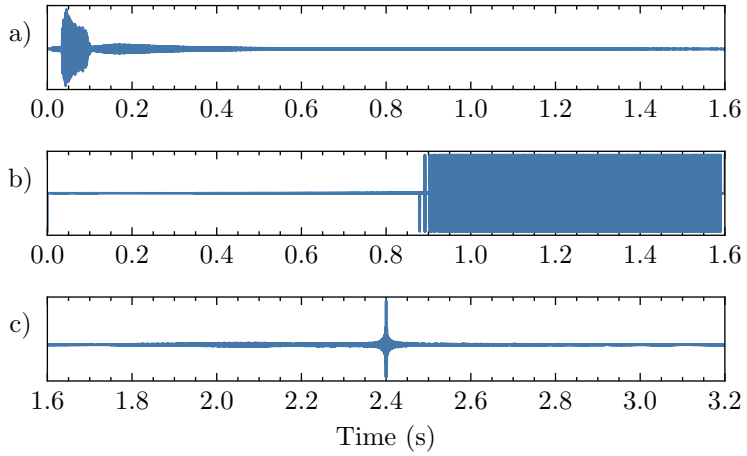

Figure 3.19: Transient waveforms at $x = 50$ m showing a) impulse response b) time reversed and clipped focussing waveform c) response to the focussing waveform.

3.5 Time Reversal Focussing

Now time reversal is used to maximise the peak response of the system. Having contrasted the thin and thick pipes in the previous section, the thick pipe is discarded and only the thin pipe is studied. The aim is to show how the dispersion in the system can be utilised in the time domain to focus energy at a given point. It was stated previously in Chapter 2 that 1-bit/clipped time reversal will theoretically lead to the largest response of a linear system. This technique is now applied to the axisymmetric pipe and the results are compared with the largest possible harmonic response over the same bandwidth.

3.5.1 Application

The relevant quantities are once again calculated in the time domain through use of the discrete fast Fourier transform (FFT). With a fixed bandwidth, and therefore Nyquist frequency f_{Nyq} of 20 kHz, the response can be calculated at any distance over N_{fft} points in the frequency domain. After applying the FFT, this leads to a an impulse response of length $T_{\text{foc}} = 1/(2f_{\text{Nyq}})$. The time reversal procedure can then be applied as in Chapter 2.

To demonstrate, the technique is applied at $x = 50$ m with a structural excitation. We concentrate on the pressure at the inner wall of the pipe, thought to be relevant for biofouling purposes. Figure 3.18 shows the pressure response in the frequency domain calculated over $N_{\text{fft}} = 2^{16}$ samples. The peak harmonic pressure

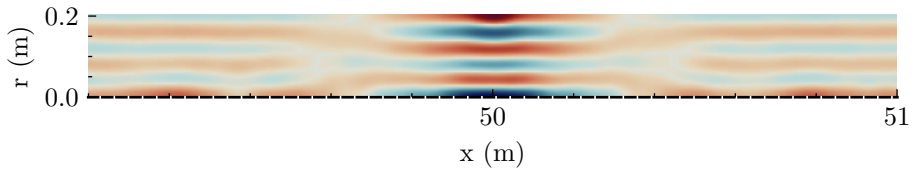

Figure 3.20: Pressure field from 49-51 m at the time when the peak pressure is obtained for time reversal focussing targeted at $x = 50$ m

is approximately 10 Pa, obtained at around 19 kHz. To exceed this pressure, we first calculate the impulse response. This is shown in Figure 3.19a). The duration in the time domain is 1.6 s which is suitable to capture the majority of the impulse response at $x = 50$ m. As previously demonstrated for the duct, there is no requirement to fully capture the impulse response when applying time reversal, and shorter durations in the time domain can be used.

Figure 3.19b) shows the focussing waveform which is created by unity normalising, time reversing and clipping/1-bit digitising the impulse response. This focussing waveform is used as the input to the force source, where its application will cause energy to converge back at the point where the original impulse response was sampled from. This is shown in Figure 3.19c) where the pressure is seen to sharply peak as the energy focusses. In this case, the maximum instantaneous pressure is over 200 Pa, a 20x increase over the largest harmonic response at this distance. The pressure gain can be expressed as

$$\text{Gain}(x) = \max(p(x,t))/\max(\tilde{\mathbf{p}}(x,\omega)) \tag{3.16}$$

which is the ratio of the largest transient response to the largest harmonic response at the same distance for the same maximum forcing amplitude.

Figure 3.20 shows the pressure field around the focus at convergence. Although the time reversal technique maximises the pressure at the wall, it should be noted that much larger pressures can be achieved at the centre of the pipe. This is a simple consequence of the zeroth order Bessel functions which describe the pressure field in the axisymmetric system, which have their peak at $r = 0$.

To evaluate the spatial resolution of the focussing technique in the present scenario, the peak instantaneous pressure is calculated at each point along the pipe wall, when subject to the waveform designed to focus the pressure at $x =$ 50 m. The results are shown in Figure 3.21, where three different durations of focal waveform T_{foc} are used, corresponding to varying the number of samples taken in the frequency domain N_{fft}. The peak harmonic pressure is also shown for comparison. In Figure 3.21, the duration of each focussing waveform is labelled by the repetition frequency at which pulses can be applied at the focus $f_{\text{foc}} = 1/T_{\text{foc}}$. As expected, the focussing waveform with the longest duration achieves the largest peak response at the focus. In addition, the longer the focussing waveform, the broader the peak. This is particularly noticeable with the 0.8 s ($f_{\text{foc}} = 1.25$ Hz) waveform, where the peak transient response is higher than the peak harmonic response over a considerable distance, far from the intended focus of $x =$50 m.

The relationship between f_{foc} and pressure and gain in this scenario is summarised in Figure 3.22. It is seen that focussing can be applied over a significant range of repetition frequencies, whilst still achieving peak responses larger than the maximum harmonic. For example, if desired, a focussing waveform can be applied at 40 Hz and still achieve a gain of 5.

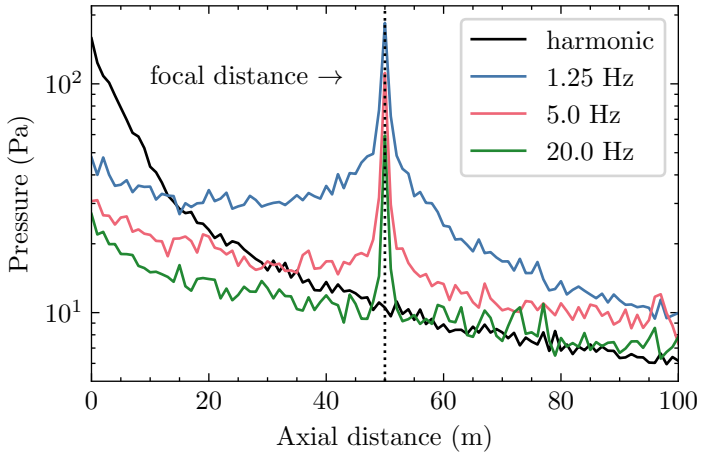

Figure 3.21: Maximum transient pressure at the wall of the pipe when applying time-reversal focussing with a structural excitation. Focussing waveforms with three different durations are applied, shown according to their repetition frequency f_{foc}. The maximum harmonic response at each distance is also plotted for comparison.

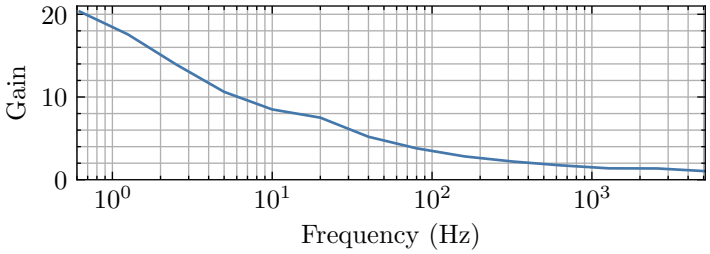

Figure 3.22: Relationship between gain and repetition frequency for time reversal focussing at x =50 m with a structural excitation.

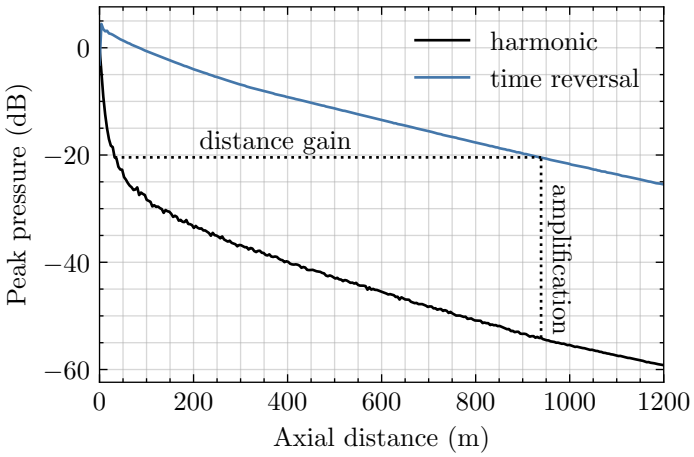

Figure 3.23: Maximum transient & harmonic pressures at the wall of the pipe when applying time-reversal focussing with a structural excitation at each axial distance. Pressures are referenced to the largest harmonic response at the input.

3.5.2 Performance vs Harmonic

We now compare the time reversal and harmonic excitations over a range of distances from the source, this time moving the focus down the waveguide axis. The repetition frequency is fixed at $f_{\text{foc}} = 1.25$ Hz. The values are referenced to the largest harmonic pressure at the driving point, and plotted in Figure 3.23. As shown, time reversal obtains the largest peak pressure at any distance from the source. Aside from the gain in amplitude, the distance at which a given pressure can be obtained harmonically is significantly extended. As indicated on the figure, the point at which the pressure has dropped -20 dB is increased from approximately 30 m to 950 m with focussing. At this point, the gain is over 30 dB. Through focussing, the range of pressures achieved harmonically under 50m is now extended to 1000m. It should also be kept in mind that the focussed peak in pressure is spatially quite broad (as in Figure 3.21), and can exceed the harmonic response many metres away from the focus.

Influence of Source and Response Quantity Figure 3.24 shows the results of the previous study repeated for all combinations of source and response quantity. There does not appear to be any significant difference in focussing performance between the various scenarios tested. Although this does not mean that they are equally effective from a biofouling perspective, the improvement yielded by time reversal will be similar when compared to harmonic forcing in the same situation.

Damping The preceding time reversal studies were performed in a pipe with 1% hysteretic damping. Naturally the level of attenuation will critically affect range at which given pressures can be obtained in the waveguide. This is particularly pertinent where there may be additional sources of attenuation, such as for a buried pipe. Although, in order to accurately study such a case, one would need to explicitly model the surrounding soil. Here, different loss factors in the structure are used to demonstrate how damping effects the maximum harmonic and time reversed transient pressures far from the source. As it has been established that results are similar between both sources and response quantities, the following

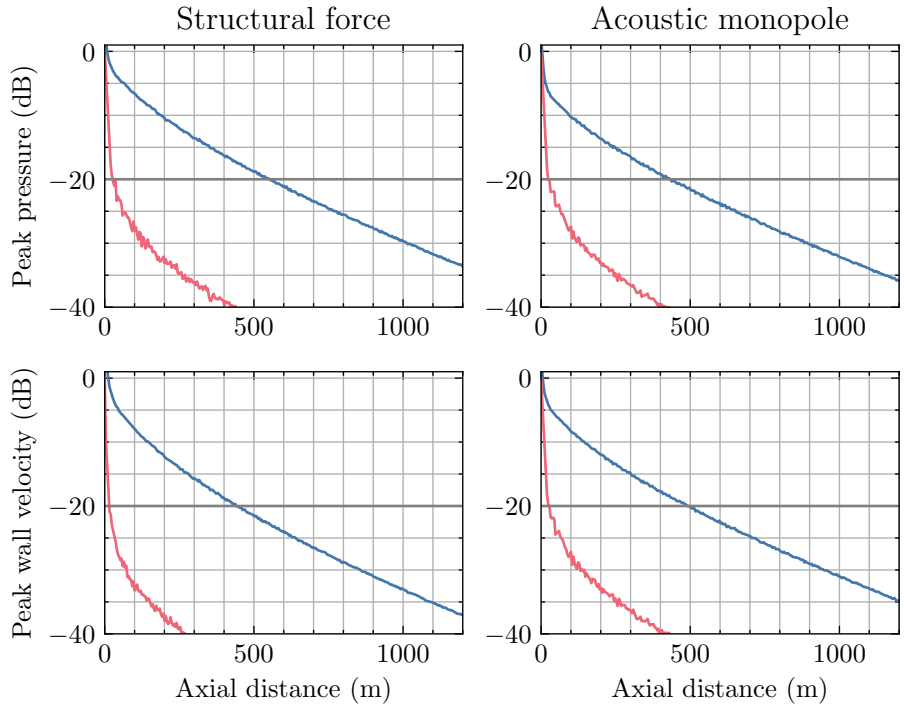

Figure 3.24: Maximum transient & harmonic wall pressures/velocities for both types of forcing.

results are obtained from the force to pressure response.

Figure 3.25 shows a parametric study using four different structural loss factors, plotted as in 3.23. All quantities are referenced to the maximum harmonic response at the input in the least damped system. Naturally, the higher the loss factor, the faster the drop in pressure from the source. In the case where the damping is very low ($\eta_s = 0.1\%$), the maximum time reversal pressure can be as much as 4 dB higher than even the maximum harmonic pressure at the input. This holds as far as 80 m from the source. Increasing the damping expectedly leads to the pressure falling off faster with distance. Interesting to note, however, is that the focussed pressure in moderately damped pipes can still comfortably exceed the maximum harmonic pressure in the lightly damped system over a considerable range of distances. For example, where the harmonic pressure has dropped by 20 dB at 200 m in the system with a loss factor of 0.1%, this point is reached at 1000, 500, and 250 m in the systems with loss factors of 0.5, 1 and 2% respectively. This shows that time reversal can be used to overcome the limitations imposed by a highly dissipative system.

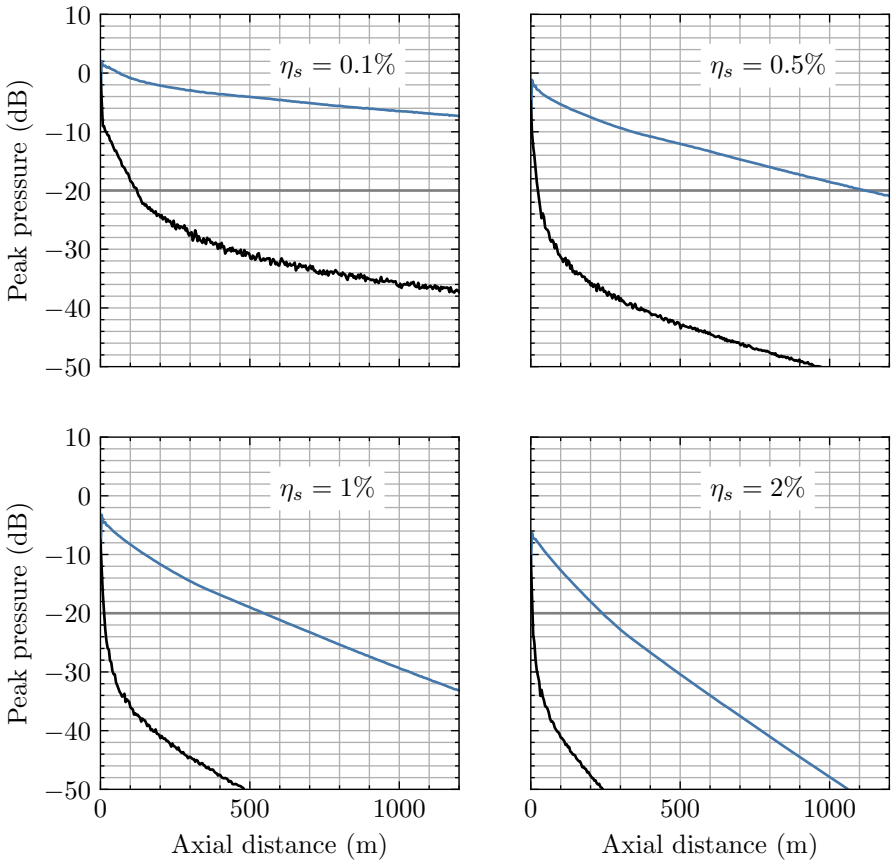

Figure 3.25: Maximum transient & harmonic pressures at the wall of the pipe when applying time-reversal focussing with a structural excitation at each axial distance. Four different loss factors are used. Pressures are referenced to the highest harmonic response at the input in the least damped system.

3.6 Conclusions

In this chapter, the WFE method was used to model and analyse the axisymmetric waves in a fluid-filled pipe. The free and forced responses were studied with respect to the various propagating wavemodes and the objective of maximising the fluid pressure and/or structural velocity at the fluid-structure interface for antifouling purposes. The excitations considered were a structural ring force on the outer wall of the pipe and a centrally located monopole source in the fluid. After studying the harmonic response, transient focussing through the use of the 1-bit time reversal method was applied to further increase the response quantity of interest at any distance from the source. The main assumptions of the model were an unburied pipe with no ring-stiffeners or structural supports down its length, and hysteretic damping present in the structure only. Both a 'thin' and 'thick' pipe were studied to gain insight to the effects of wall thickness on the system.

3.6.1 Discussion

When studying the free waves, there were four main types of wave behaviour identified in the system. The fluid wave could be grouped into the fundamental wave, akin to the acoustic plane wave, and the higher order acoustic modes which arise in a duct. The structural waves were those which either related to predominantly in-plane longitudinal motion or out-of-plane radial motion. By analysing the attenuation curves it was found that the waves which exhibit high radial motion of the pipe wall were by far the most attenuated, followed by longitudinal structural waves. Waves which propagated predominantly in the fluid, largely uncoupled from the structure, experienced the lowest levels of attenuation, making them seemingly more attractive for long range antifouling. The differences between thin/thick pipes were found mostly in the level of fluid-structure coupling for different modes. The fundamental fluid mode intuitively showed much lower coupling with the the thick pipe. However, the higher order acoustic modes were shown to couple more strongly with the thick pipe overall at higher frequencies. This was due to coupling with the S0 type mode in the pipe wall, which, in the thick pipe, is fast enough to cross the acoustic branches in the phase-velocity domain. This lead to a more even energy distribution between fluid and structure and for this reason levels of attenuation were broadly higher in the thick pipe.

For the forced harmonic response, the behaviour could be grouped into three frequency ranges. Namely below, at, or above the ring frequency. Below the ring frequency, the power injected was predominantly fluid based regardless of excitation. At the ring frequency, the power was mostly structural and above the ring frequency the distribution of energy depended primarily on the type of excitation, with power concentrated in either the fluid or wall for an acoustic or structural excitation respectively. When evaluating the power flow far from the source however, it was determined that the energy distribution is skewed toward the fluid due to the damping in pipe wall bleeding energy out of the structure. From this it can once more be concluded that mostly uncoupled fluid waves at high frequency are the most suitable for antifouling at range. The calculations of total power flow at the input and far from the source demonstrated that the higher frequencies, where acoustic duct modes dominate, are by far the best excited and least attenuated. Whilst the fundamental waves which propagate at very low frequencies are also lightly attenuated, they are also not as strongly excited as the

higher order modes which resonate at cut-on. The highest attenuation was found at the ring frequency, where radial motion of the pipe wall is very high. Whilst this high radial motion is ostensibly beneficial from an antifouling perspective, it does not carry far down the pipe. Therefore it is concluded that the ring frequency resonance is likely to be useful for biofouling control only at short ranges.

The low attenuation of high frequency acoustic waves was further demonstrated by comparing the monopole-source-induced wall pressure to that of a rigid walled acoustic duct. Here it was shown that the fluid-coupled pipe approaches the behaviour of a hard-walled duct with increasing frequency. Additionally the behaviour also converges at very low frequencies, where only the acoustic plane wave propagates and the mechanical impedance of the pipe wall is very high.

With the application of 1-bit time reversal, it was shown that a transient excitation can be used to obtain an instantaneous response at a target point much higher than that of the greatest harmonic excitation. The pressure or velocity 'gain' was shown to depend primarily on the length of the impulse response, which, unconstrained by the duration of the FFT, is a function of the damping and distance from the source. The actual duration of the transient focussing waveforms were constrained by the FFT duration whilst keeping bandwidth constant. Shorter focal waveforms could then be applied more frequently at the cost of peak response and vice versa. It was additionally found that a longer focussing waveform yielded a spatially broader peak along the axis, meaning that although the pulses of pressure/velocity are applied at a lower repetition frequency, a greater area of the pipe wall can be treated at once.

When applying the focussing technique across a range of axial distances, it was shown that a given pressure could be extended far beyond what is possible with a harmonic excitation. For the case of 1% damping in the fluid, the -20 dB harmonic pressure was extended from 50 to 1000 m. The performance was shown to generally hold across all combinations of excitation and response, demonstrating the robustness of the 1-bit time reversal technique. When evaluating the effect of damping, it was shown that the loss factor in the pipe wall critically affects the range at which a given response can be obtained. However, even in the strongly damped system, the application of time reversal yielded peak responses which were far greater than the harmonic response in its lightly damped counterpart over a considerable range. This indicates the focussing technique is less susceptible to the effects of attenuation in the waveguide as opposed to a harmonic excitation, where the peak response drops far more rapidly.

3.6.2 Conclusion

The analysis in this chapter has explored harmonically and transiently exciting an axisymmetric water pipe to maximise the pressure and structural velocity at the pipe's inner wall. It was determined that long range transmission of power down the pipe is best achieved with an acoustic excitation in the fluid above the ring frequency, where higher order acoustic waves can propagate largely uncoupled from the structure and therefore experience lower levels of attenuation. Alternatively power can also flow through the fundamental fluid wave relatively unattenuated at very low frequencies. This wave is less well excited than the higher order modes, however. The prominence of these waves for carrying energy in the system was highlighted through comparison to a rigid walled duct, where it was shown that significantly above or below the ring frequency the fluid-coupled pipe approaches

the uncoupled duct solution.

Although vibration in the structure, particularly radial motion, is highly attenuated at long range due to hysteretic damping, nearer to the source it may still be used as an effective means of biofouling control. In this case excitation near the ring frequency, where the pipe wall resonates radially, provides the highest level of structural vibration and the largest input power over all frequencies for a structural force.

Where time reversal focussing is applied, the entire bandwidth studied is utilised with a transient excitation in the form of the system's impulse response. The focussing technique used, namely 1-bit time reversal, was shown to significantly increase the pressure/velocity at a targeted distance compared to a harmonic excitation with the same source strength. The harmonic/transient methods are contrasted by a high power, high frequency, continuous sinusoidal response on the one hand, versus a low power, low frequency pulse train with much larger peak responses on the other. Time reversal was shown to be robust when applied to systems with differing levels of damping, with the transient peak response decaying with axial distance much more slowly than the harmonic peak response. At long range particularly, time reversal focussing proves effective in increasing the response or extending the range of a given response.

4. Higher-Order Wave Propagation and Focussing in a Fluid-Filled Pipe

4.1 Introduction

Having studied the axisymmetric ($n = 0$) system, the analysis is now extended to the higher circumferential order waves ($n > 0$) which propagate in the pipe. These are modes for which the displacement field is periodic along the circumference (with period n). Although great in number, in practice the lowest order modes predominate the response, particularly at low frequencies. For this study, only the thin pipe from Chapter 3 is used.

To avoid incurring high computational cost associated with modelling the full cross-section in WFE, this chapter uses the cyclic symmetry assumption along the circumference. This reduces the size of the problem and separates modes by their circumferential order. Free wave behaviour and forced response is then analysed for each n, both for an acoustic and structural excitation. Time reversal is applied to the multiple higher order modes in the pipe and results compared to the axisymmetric system to illustrate the advantage of these waves for increasing peak response at a given point in the pipe. The implications for biofouling control at close and long range are discussed.

Finally the response to one or more point excitations, used to represent discrete actuators, is studied with a superposition of all propagating circumferential modes. With this, guided waves can be focussed at targeted angles in the pipe, either with a single actuator or a time reversal mirror acting as a phased array. The influence of the source bandwidth is analysed to determine the best frequency range to implement transient focussing.

4.2 Numerical Modelling

The propagation of all higher-order modes can be predicted using the WFE method. This typically requires a 2D cross-section (Figure 4.1), as opposed to the line of 1D elements used in Chapter 3. Whilst more efficient than conventional FE, this approach still requires a large number of degrees of freedom and considerable computation time to obtain accurate results.

Alternatively, the same two-dimensional mesh as in Chapter 3 is used to model the system restricted to a single n by assuming the field in the circumferential direction is periodic and has an integer number of wavelengths around the circumference [96]. Figure 4.2 shows a diagram of one face of the WFE mesh. The degrees

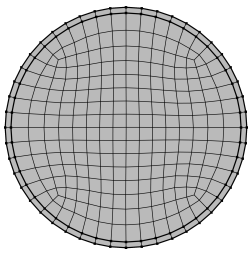

Figure 4.1: One face of the full 3D WFE mesh.

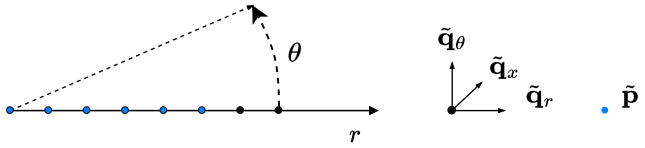

Figure 4.2: One face of the cyclically symmetric WFE mesh. The boundary conditions are chosen so that each model represents a single circumferential mode order n.

of freedom are $(\tilde{\mathbf{p}}, \tilde{\mathbf{q}}_r, \tilde{\mathbf{q}}_x, \tilde{\mathbf{q}}_\theta)$ where the latter denotes the torsional motion of the pipe. With the boundary condition $\tilde{\mathbf{q}}(x, r, \theta) = \tilde{\mathbf{q}}(x, r, \theta + 2\pi)$, the displacement field is given by

$$\tilde{\mathbf{q}}(x, r, \theta) = \tilde{\mathbf{q}}(x, r, 0)e^{-jn\theta} \tag{4.1}$$

This is implemented natively in COMSOL, which once again serves as a tool for creating the geometry, mesh, and assembling system matrices. Each circumferential order is represented by a separate model using the same mesh.

4.3 Analysis of Higher Order Modes

4.3.1 Free Waves

The dispersion and attenuation curves for n up to 5 are shown in Figure 4.3. Four main types of wave behaviour are observed with corresponding high frequency asymptotes. These relate to the longitudinal, torsional, and flexural motion of the structure, and pressure waves in the fluid. As in the axisymmetric system, the $n > 0$ modes have many branches above the ring frequency which switch their behaviour between predominantly structure and fluid-borne waves.

Below the ring frequency, most propagating waves are flexural. For $n = 1$ the flexural mode corresponds to the well known fundamental beam bending mode at low frequency, where the radial and circumferential displacements have approximately the same magnitude. The $n > 1$ flexural solutions have cut-on frequencies which depend mostly on the pipe diameter, and exhibit a sinusoidal pattern of wall flexure around the pipe circumference. Below this cut-on, no modes can propagate and as such, waves excited close to 0 Hz are only of the order $n < 2$. The cut-on frequencies of the flexural branches increase with n, and the waves become more

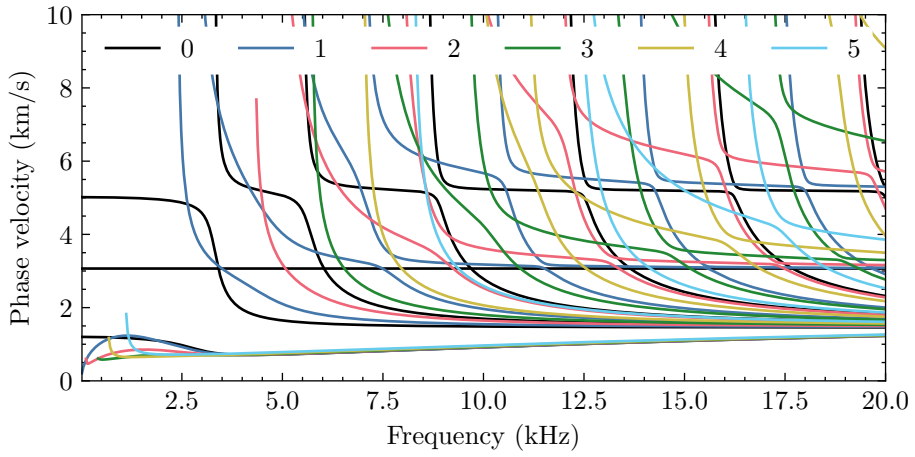

(a)

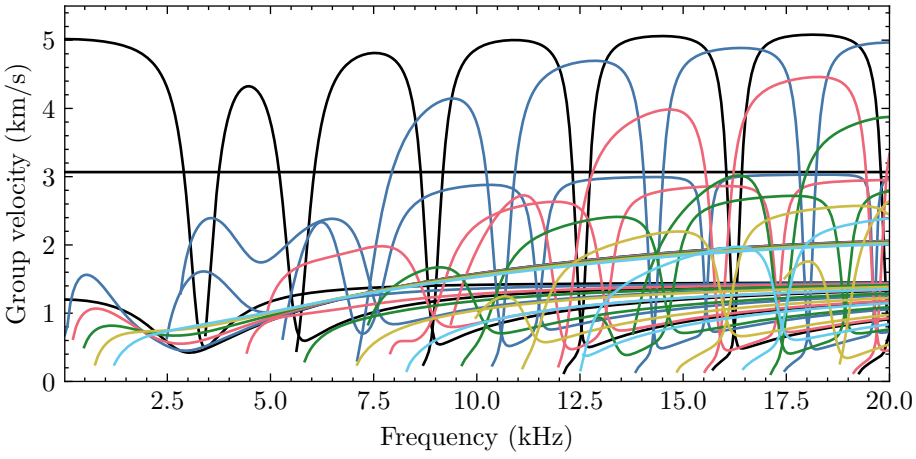

(b)

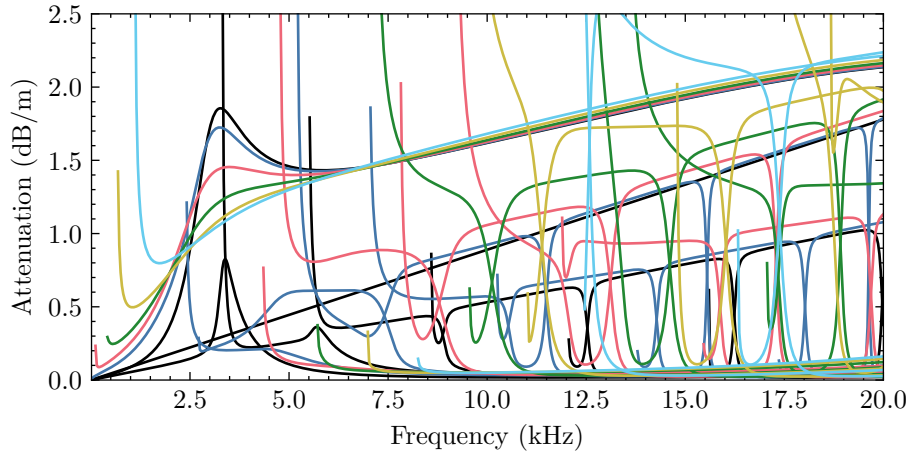

(c)

Figure 4.3: (a) phase and (b) group velocities for the thin (solid) and thick (dashed) pipe systems. Also shown in black are the phase velocity curves for the rigid duct.

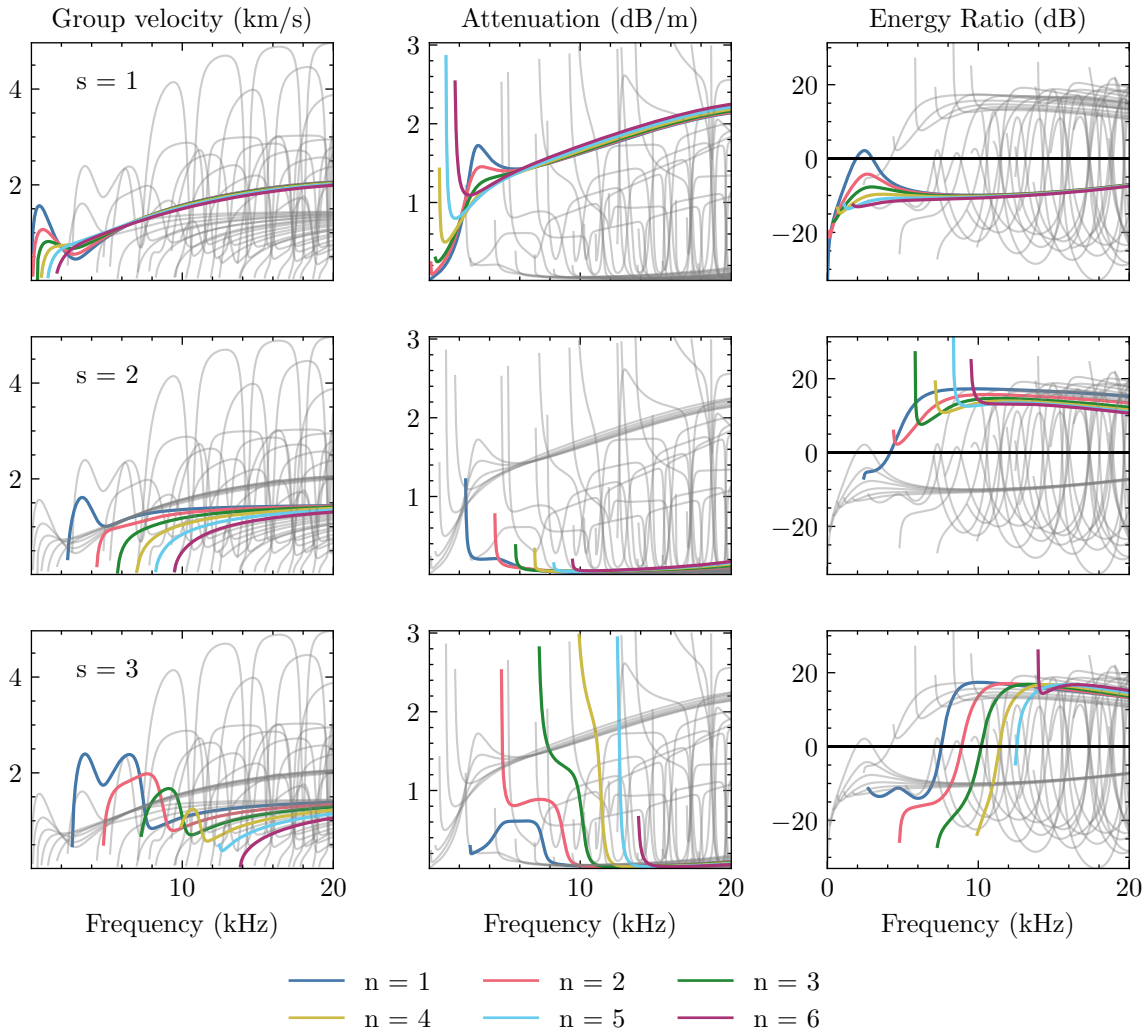

Figure 4.4: (a) phase and (b) group velocities for the thin (solid) and thick (dashed) pipe systems. Also shown in black are the phase velocity curves for the rigid duct.

dominated by radial motion. Far above the cut-on frequency, all of these modes converge to the same plate-like solution.

Separating the branches for each $n > 0$ by their order of cut-on, denoted with s, Figure 4.4 shows in further detail the first three modes which cut on for each n from 1 to 6. For the flexural ($s = 1$) solutions, the attenuation is higher than for other waves, with increased peaks at the ring frequency for smaller n. The fluid-structure energy ratios indicate power is mostly carried in the pipe wall with waves also becoming more structurally dominated with n. The notable exception to this is the $n = 1$ bending wave, which carries most of its energy in the fluid for a small bandwidth around the ring frequency. This occurs below the cut-on of any acoustic mode, and so the energy is stored in the forced pressure field which tightly hugs the fluid-structure boundary [49].

The second wave to cut on for each n is the first acoustic duct mode of that circumferential order, which has zero nodal lines in the radial direction. From their velocity, attenuation and energy ratios curves in Figure 4.4, these branches appear almost completely uncoupled from the structure, and behave close to a pure duct mode. With the exception of the $n = 1$ beam mode, the power flows mostly in the fluid over the entire bandwidth studied and correspondingly the attenuation

is lowest. This occurs because the acoustic duct modes cut on significantly below any propagating structural mode with a similar wavenumber for the same n. As a result, there is very little coupling with the pipe wall. This effect becomes more pronounced with increasing n, as the structural and acoustic modes move away from one another in the wavenumber domain. The same phenomenon is seen for the $s = 3$ waves, where at $n = 6$ mode in Figure 4.4 is almost entirely uncoupled from the wall.

For the remaining $s > 3$ waves, there is increasing coincidence between duct and *in vacuo* pipe modes and branches rapidly change their behaviour, appearing as mainly either acoustic or structural (longitudinal and torsional) waves. As with the axisymmetric case, the regions of coupling become narrower at high frequency, and the pipe appears stiffer to the fluid overall.

4.3.2 Forced Waves and Focussing

This section analysis the forced response to a structural/acoustic source exciting waves of a single circumferential order n. Simulating the orders separately allows comparison between different modes of excitation. In practical contexts, more than one n is likely to be excited, but the response to an arbitrarily distributed source can be represented with a weighted sum of single n responses. This is applied for a point source later in Section 4.4.

Acoustic Excitation For the acoustic excitation, an off-axis line source located at the inner wall ($r = a_i$) is used, which is distributed circumferentially as required. This will most strongly excite modes which have their peak pressure close to the pipe wall. A source located at $r = 0$ will only excite axisymmetric modes as in Chapter 3. As before, the Helmholtz equation governs the fluid domain

$$\nabla \cdot \left(-\frac{1}{\rho_f} \nabla p \right) - \frac{k_f^2 p_\mathrm{t}}{\rho_f} = \frac{4\pi}{\rho_f} S\delta\left(x\right) dx, \quad S = \frac{i\omega\rho_f}{4\pi} Q_s' e^{-jn\theta}. \tag{4.2}$$

with the addition of the circumferential extension. The source term is specified in per unit length and the source strength Q_s' has units $\mathrm{m}^2\,\mathrm{s}^{-1}$.

Structural Excitation A structural excitation takes the form of a distributed force applied over the outer wall of the pipe ($r = a_o$). The input to the WFE model specifies the total force distributed over the circumference, expressed as a linear force density

$$p_n(\theta) = \frac{F_\mathrm{tot}}{2\pi a_o} e^{-jn\theta} \tag{4.3}$$

where F_{tot} is the total force applied and in this case equal to 1 N.

The power distribution between fluid and structure at the driving point is calculated and shown in Figure 4.6 for the two different types of forcing with modes n from 0 to 6 plotted. Unlike the axisymmetric case, where power is mostly carried in the fluid below ring frequency, all modes are predominantly structural for $n > 0$ at low frequency. The $n > 1$ orders contain no fundamental modes, and so at frequencies close to 0 Hz power can only be carried in $n = 0$ and $n = 1$. Additionally, since only the flexural modes propagate below the cut-on of the first acoustic mode ($s = 2$), the energy ratio of the higher order responses are the same regardless of the excitation used over this bandwidth. Here the energy flow

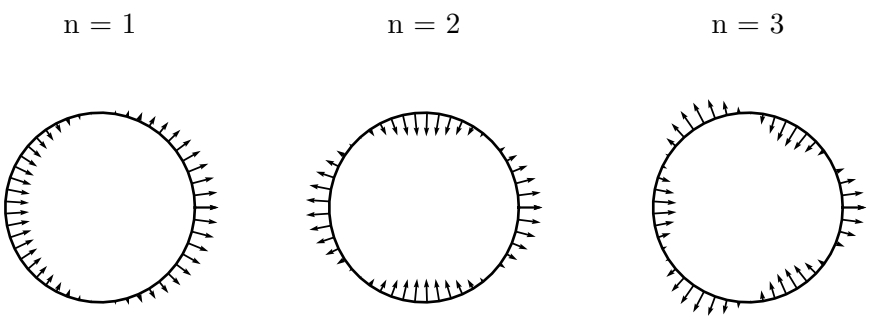

Figure 4.5: Illustration of the circumferential forcing applied to the system for each n.

is exclusively dominated by the pipe wall with the $n = 1$ exception mentioned before.

After the cut-on of the $s = 2$ mode, the energy ratios change markedly, and for both excitations tip towards the fluid. Beyond this frequency, the energy ratio is determined mostly by the type of excitation, with the energy ratio being mostly positive/negative for an acoustic/structural excitation respectively. Whilst the energy ratio for a force source can tip strongly towards the fluid over a few narrow frequency regions where coupling is high, the acoustic source preserves the power almost entirely in the fluid over the same bandwidth.

Propagated Power The total power flow in both fluid and structure at the input and at $x = 50$ m are shown for the structural and acoustic excitation in Figures 4.7 & 4.8 for each n. These indicate the relative power flow in for each circumferential order.

For a low frequency structural excitation at or close to the source, the total power injected increases with n. The axisymmetric excitation induces very little power flow due to the high stiffness at low frequency in this mode of vibration. Moving toward the ring frequency, the situation is somewhat inverted. Here the axisymmetric mode resonates and carries the most power, followed by the $n = 1$ & $n = 2$ modes, with no significant difference in power flow for $n > 2$. Beyond the ring frequency, the system is mostly dominated by the acoustic response. In this case, the circumferential order is less critical to the power flow, with the average power being comparable between n and slowly decreasing with frequency. The sharp peaks seen in this frequency range are associated with duct modes cutting on. By calculating the power flow at long range ($x = 50$ m), the effects of structural damping are observed with a particularly acute effect on the low frequency flexural modes. Now the peak power flow decreases with n as the higher circumferential orders experience more attenuation over the distance calculated. Notably $n = 1$ carries the most power at the ring frequency. This is because the first $n = 1$ duct mode is propagating, allowing power to flow in the undamped fluid. Similarly in the axisymmetric case, the power flow is relatively unattenuated around the ring frequency since power can flow in the fundamental acoustic mode. For the higher circumferential orders there is a sharp transition in power flow corresponding to that seen in the energy ratios in Figure 4.6. As the first duct type mode cuts on for each n the power flow increases and attenuation drops drastically as acoustic waves begin to propagate in the fluid. Beyond this frequency the power flow is

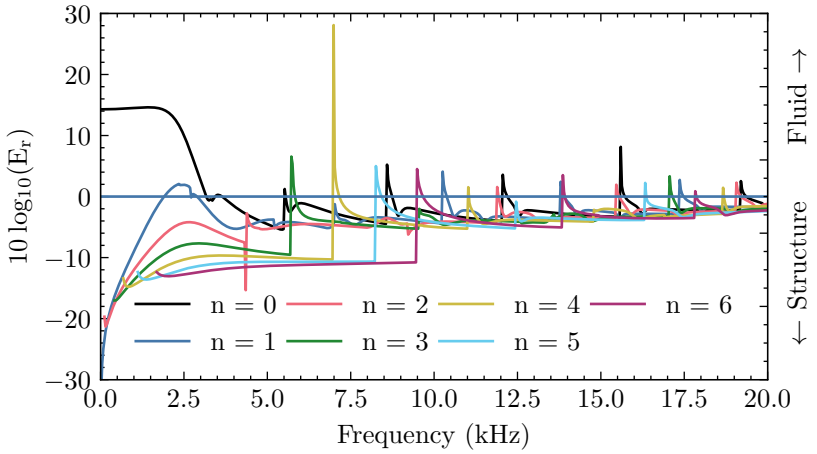

(a)

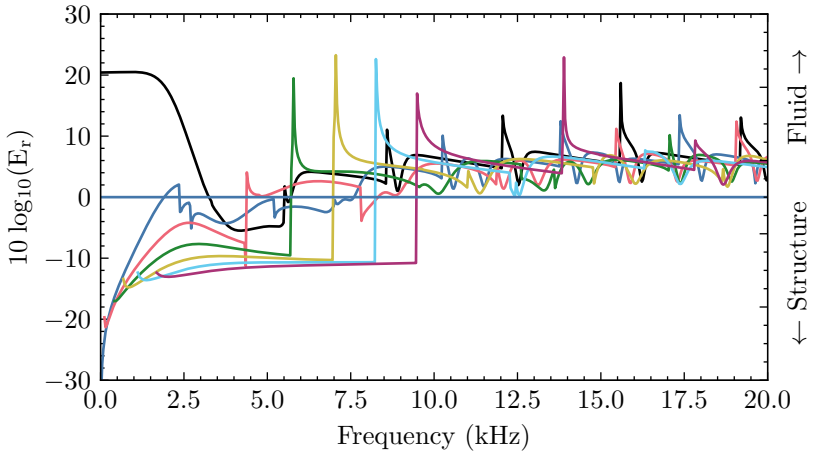

(b)

Figure 4.6: The forced energy ratio for each circumferential mode when the pipe is excited with a) a structural force and b) an acoustic line source.

comparable between circumferential orders.

With an acoustic excitation, there is very little power flow for $n > 0$ at low frequencies, where no acoustic waves propagate and the pressure field is 'forced' by the structure. Only the axisymmetric fluid dominated mode carries significant energy here. This is also the case at $x = 50$ m where the axisymmetric fluid dominated mode is also predominant at low frequencies. As the first acoustic mode cuts on for each n, the power flow increases abruptly as seen before with the structural excitation. Beyond this frequency the various duct type waves are responsible for most of the power flow.

To summarise, the system's response for the $n > 0$ waves can be divided into the range of frequencies above and below the cut-on of the first acoustic ($s = 2$) mode. Below this cut-on, power is constrained to the structure and flows only in the set of flexural modes, which themselves are subject to a low frequency cut-on for $n > 1$. Intuitively, an applied radial force on the structure most effectively excites these waves. The response close to the source increases with n and lower order circumferential modes are less mobile, a trend which extends to the $n = 0$ response. At long range, however, the higher n waves are more strongly attenuated and as such the lower orders contribute more to the response. When considering an acoustic excitation in this bandwidth, no wave propagation in the fluid is possible for $n > 0$, and so only the flexural branches are excited indirectly by the pressure at the wall. Near the source, the response decreases with n. Because of the fundamental acoustic mode, the $n = 0$ case stands out at being able to excite propagating fluid waves at very low frequency, and so dominates over all other n when applying an acoustic excitation close to 0 Hz.

Above the cut-on of the first acoustic mode, the power flows predominantly in the fluid at long range for both excitations as a consequence of the damping in the structure. Therefore over this bandwidth an excitation in the fluid is presumed to be most effective at transmitting power down the pipe. For $n = 4, 5, 6$, the peak power at range occurs when the first acoustic mode cuts on. This is in contrast to the axisymmetric fluid modes, which have larger pressure peaks with increasing frequency.

Transient Focussing The 1-bit/clipped time reversal technique is now applied to each circumferential system up to $n = 6$, and compared with the maximum harmonic response over the same bandwidth. This is to assess the differences between circumferential orders in the ability to maximise the response with either a harmonic or focussed transient excitation, given the same source strength. As in the previous chapter, the acoustic pressure at the wall and the structural wall velocity will be considered when the system is subject to a structural/acoustic excitation.

Figure 4.9 shows the peak harmonic and transient focussed responses for each combination of source and response quantity. In each case, the response is referenced to the highest harmonic response at the input over all n. The gain and range advantage of transient focussing extends the -20 dB point to over 400 m in most cases. The best performance is seen in the acoustic-pressure case, which has the slowest roll-off. Conversely, the force-velocity case has by far the steepest roll-off due to high structural attenuation, although an exception is seen for the $n = 1$ mode due to the attenuation in the beam bending mode approaching zero at 0 Hz, whilst the system is still relatively mobile to structural forcing. A similar phenomenon is seen in the acoustic-pressure response for the $n = 0$ mode, where

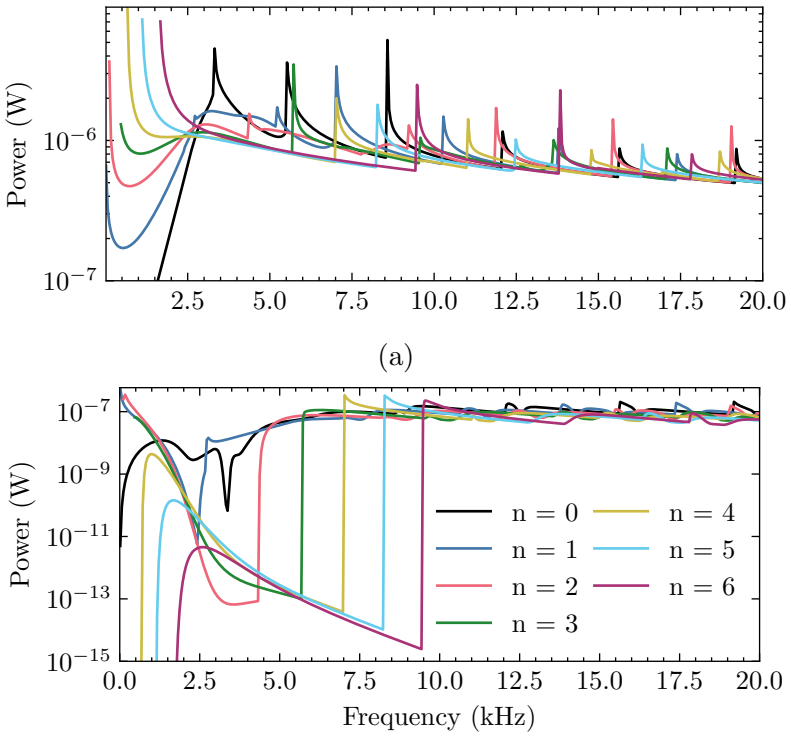

Figure 4.7: Axial power flow in each circumferential order of the pipe subject to a structural force. a) $x = 0$ m and b) $x = 50$ m.

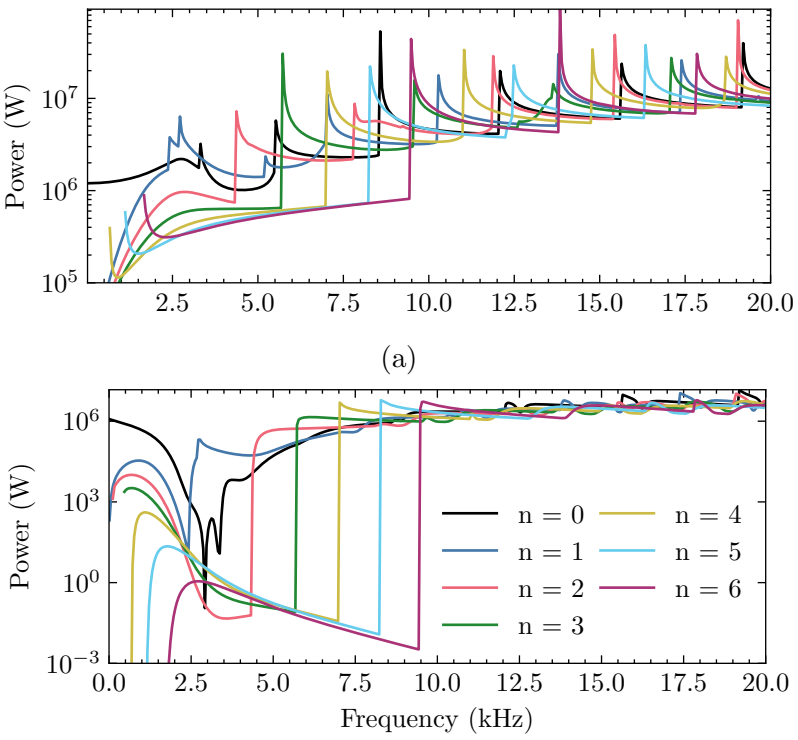

Figure 4.8: Power flow in each circumferential order of the pipe subject to an acoustic source. a) $x = 0$ m and b) $x = 50$m

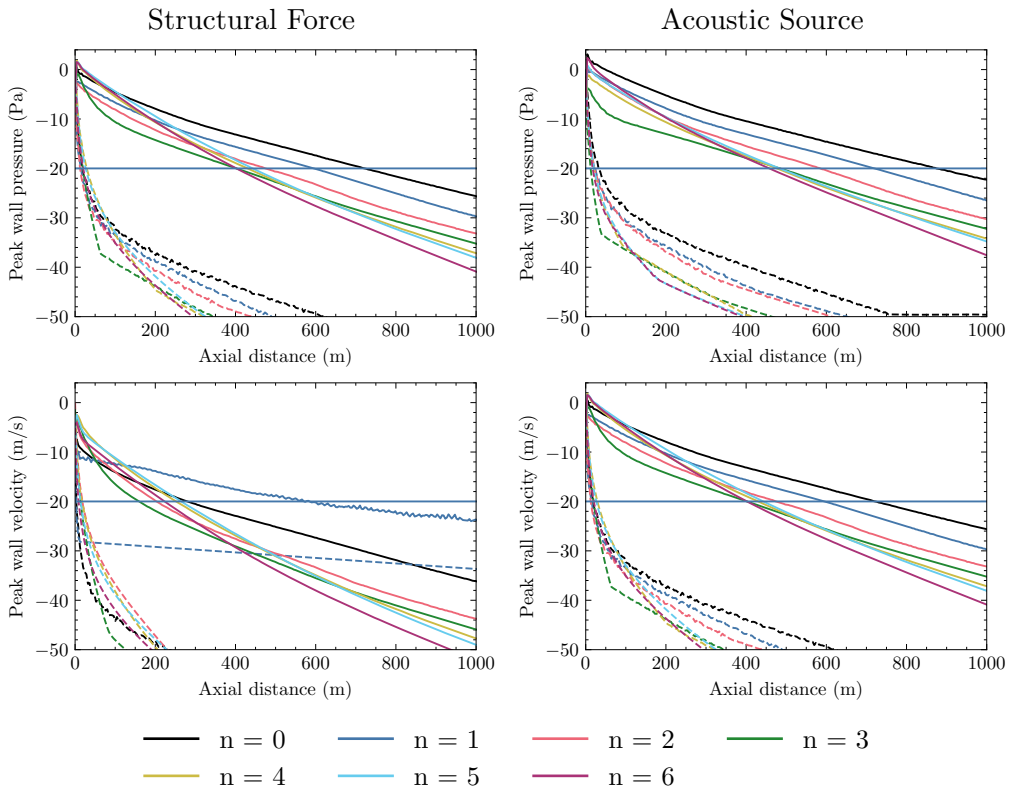

Figure 4.9: Maximum harmonic (dashed) vs time-reversed (solid) response at pipe wall for various circumferential mode orders and combinations of source and response quantity. Expressed in dB with respect to the largest harmonic response at the source over all n.

the roll-off of the peak harmonic response abruptly flattens out near 800m. This arises out of the near-zero attenuation of the fundamental acoustic wave at very low frequencies, which is still excited by an acoustic source. Such behaviour is the basis of long range acoustic leak detection in water pipes.

Very close to the source, the maximum response is generally found in circumferential orders $n > 0$. The input mobility subject to a structural force peaks with $n = 3$ and then gradually decreases with increasing n. Far from the source however, the responses are sorted according to their circumferential mode order, with the lowest n having the highest response at long range.

4.4 Point Excitation

In this section, all propagating modes in the system are excited through the application of one or more point forces/sources. The response is a superposition of the higher-order modes discussed so far. Use of such a localised excitation allows for more precise spatial focussing and multiple point sources can be deployed as a time reversal mirror, or phased array.

4.4.1 Formulation

An arbitrary force distribution $p(\theta)$ can be represented [54] with a Fourier series of the circumferential modes

$$p(\theta) = \sum_{n=-\infty}^{\infty} \hat{F}_n e^{-jn\theta} \tag{4.4}$$

with the coefficients $\hat{F}_n$ depending on the desired linear force density function. For a point force at $\theta = 0$ of total strength F_{tot}, the force distribution can be described as a function of arc length $s = r\theta$ with a Dirac delta $p(s) = \delta(s)$ such that

$$\int_{-\pi r}^{\pi r} F_{tot}\, \delta(s) ds = F_{tot}. \tag{4.5}$$

For a force applied to the external wall of the pipe, this expands into the Fourier series

$$p_\delta(\theta) = \frac{F_{tot}}{2\pi a_o} \sum_{n=-\infty}^{\infty} e^{-jn\theta} \tag{4.6}$$

which has constant coefficients independent of n. The application of an ideal point force therefore excites all circumferential orders equally and the series in Equation 4.6 requires an infinite number of terms to be accurate.

Alternatively, a point force can be represented by a rectangular pulse of finite width. Considering the force to be applied between $\theta - \Delta$ and $\theta + \Delta$ with a height H such that $2\Delta H = F_{tot}$, this leads to the expansion

$$p_\delta(\theta) = \frac{F_{tot}}{2\pi a_o} + \frac{F_{tot}}{\pi a_o} \sum_{n=1}^{\infty} \frac{\sin(n\Delta)}{n\Delta} e^{-jn\theta} \tag{4.7}$$

in which case the amplitude of circumferential orders $n > 0$ will decay according to the $\mathrm{sinc}(n\Delta)$ function, with the roll-off determined by Δ. Where $\Delta = \pi$ the applied force is axisymmetric and only $n = 0$ modes are excited. Conversely, the series tends to that of the ideal delta function as $\Delta \to 0$. Intuitively, this means the number of circumferential modes which meaningfully contribute to the response is determined by the arc length of the force applied relative to the pipe's circumference.

In practice, however, in the far field the number of terms required for accurate prediction of a point force response will chiefly depend on the maximum frequency of the excitation, which corresponds to the number of cut-on modes. Since all $n > 1$ modes have a non-zero cut-on frequency, the series in equation 4.4 can be truncated according to the number of propagating circumferential modes over a given bandwidth. This can be reasonably well approximated by considering the uncoupled structural and acoustic systems. For the waves in the pipe wall, the flexural branches cut on first and can be approximated using thin shell equations [47, 162].

$$f_{\text{flex}} = \frac{c_L}{2\pi\bar{a}} \sqrt{\frac{\left(\frac{h^2}{12a^2}\right) n^2 \left(n^2-1\right)^2}{\left(n^2+1\right)}} \tag{4.8}$$

where c_L is the longitudinal plate velocity. The cut-on frequencies of a hard acoustic duct can be found as in Chapter 2

$$f_{\text{duct}} = \frac{c_f \eta_{n,1}}{2\pi a_i}. \tag{4.9}$$

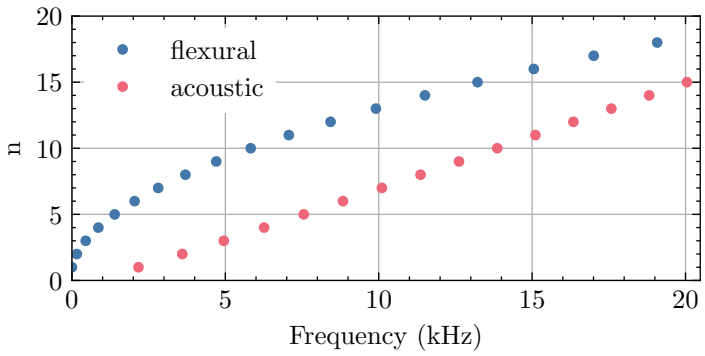

Figure 4.10: Flexural and acoustic mode cut-on frequencies in an isolated shell and rigid duct.

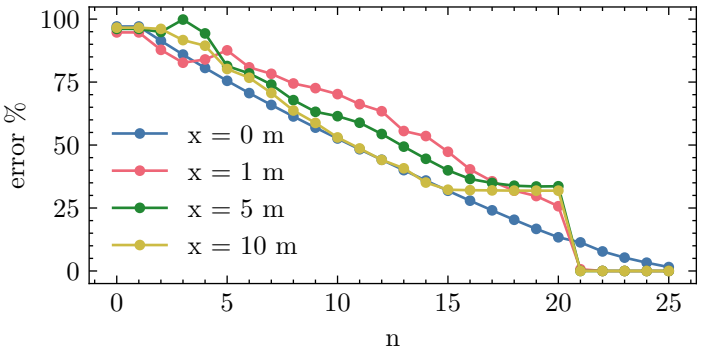

Figure 4.11: Error in the force-to-velocity transfer function when truncating the series at n

The cut-on frequencies are shown in Figure 4.10. The flexural modes are always the first to cut on over this bandwidth, and truncating the series after approximately 20 terms should yield sufficient accuracy to model a point excitation. To verify this, the force-to-velocity transfer function of a point excitation is calculated with varying the number of n included up to 25. The relative error as compared to the 26 term response is shown in Figure 4.11. Away from the source, the result converges at $n = 21$ and the error drops to zero. At the driving point, there is still a small error above $n = 21$ due to the near-field contributions of modes which are below their cut-on frequency.

Comparing this to the series for a rectangular pulse, this means practically that there are a range of widths which produce a 'point-like' response in the pipe over a given bandwidth. It is found for the present case that an applied force arc length < 3 cm will behave sufficiently like an ideal point excitation.

The response to an acoustic monopole source can be constructed in the same way as for the structural force. The monopole is located at the inner wall by superimposing line sources with densities $Q'_s/2\pi a_i$.

Modelling Single and Multiple Sources The response to one or more unity strength point sources is now calculated. For a single circumferential order n, the response at $\theta = \theta_{ext}$ for a given axial distance to an input force of 1N is denoted $H_0(n, \omega, r)$. The solution can then be extended in the circumferential dimension

with

$$H(n, \omega, r, \theta) = H_0 e^{-jn(\theta - \theta_{ext})} \tag{4.10}$$

after which the superposition of circumferential modes for a point force is calculated with a flat summation

$$H(\omega, r, \theta) = \sum_{n=1-N}^{N-1} H_0 e^{-jn(\theta - \theta_{ext})} \tag{4.11}$$

Due to the linearity of the system, the preceding analysis can be readily extended to the case where there are multiple excitations acting around the pipe at various θ. The contribution of M evenly spaced spaced excitations is expressed

$$H(\omega, r, \theta) = \sum_{m=0}^{M-1} \sum_{n=1-N}^{N-1} H_0 e^{-jn(\theta - \theta_{ext})} \tag{4.12}$$

where $\theta_{ext} = 2\pi m/M$.

In Figure 4.12 the input response to a radial point force on the outer wall is plotted for 3 frequencies. For comparison and validation, the calculation is compared between the superimposed cylindrically symmetric models and the full WFE segment with a 2D cross-section.

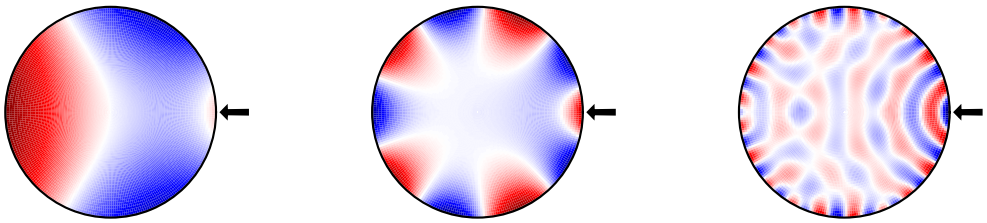

(a) (b) (c)

Input pressure response in the fluid calculated with superposition of 22 cyclically symmetric models.

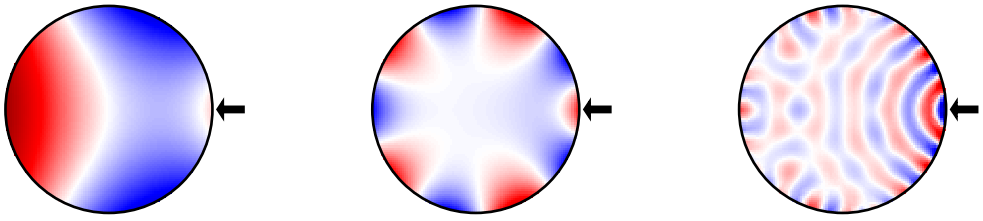

(a) (b) (c)

Input pressure response in the fluid calculated with a full 3D mesh of the pipe with a 2D cross-section.

Figure 4.12: Comparison of the pressure response at $x = 0$ m between the superimposed cylindrically symmetric models and the same system meshed in 3D. a) 50 Hz b) 1000 Hz, b) 20,000 Hz.

4.4.2 Harmonic Power Flow

The harmonic power flow in the pipe for a structural/acoustic source is briefly discussed and shown in Figure 4.13. The distribution of power between fluid and structure has been determined in the previous section. Power injected is mostly fluid/structure based for an acoustic/structural excitation respectively, a result which has been established using analytical models in [53,54]. Far from the source the majority of the power is found in the fluid due to the relatively high structural attenuation. The power loss for both types of excitation peaks around the ring frequency of the pipe and attenuation is lowest at either very low or high frequencies. As seen previously, the acoustic excitation suffers considerably lower attenuation overall.

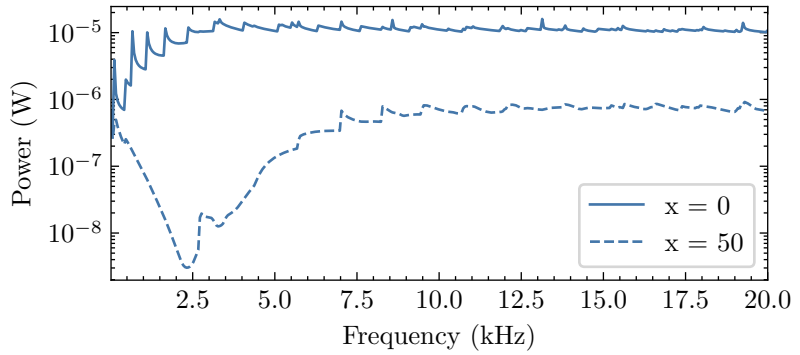

(a)

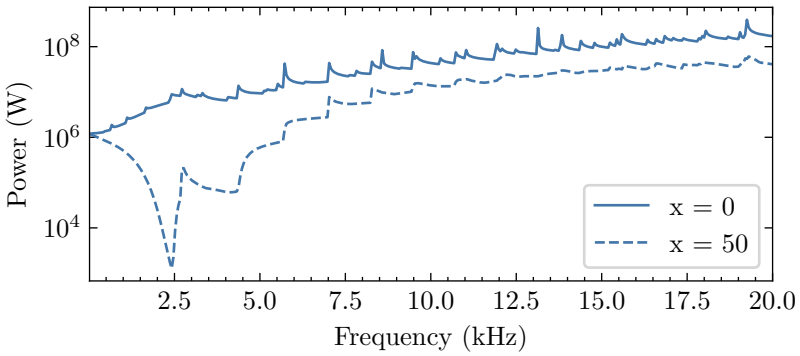

(b)

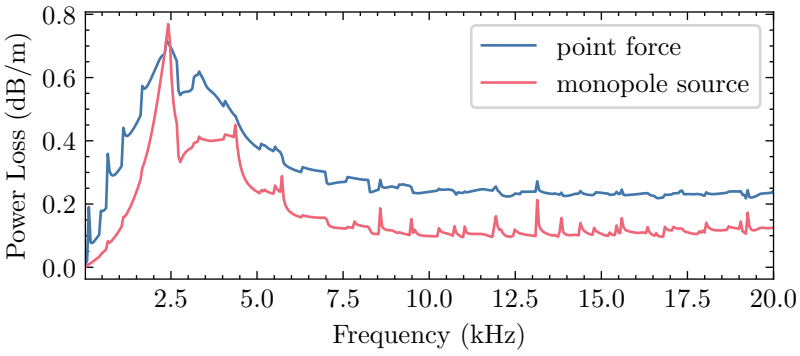

(c)

Figure 4.13: Power flow at a) $x = 0$ m b) $x = 50$ m and c) the corresponding power loss for a point force and acoustic source

4.4.3 Time Reversal and Spatial Focussing

The superposition of multiple circumferential modes excited with a point source allows for more precise focussing of energy through the circumferential dimension. Application of time reversal then allows the focal point to be located at any specific coordinate in the waveguide.

To demonstrate this, in the following study time reversal is applied at a distance of $x = 50$ m to focus acoustic pressure with a single structural point force at $\theta_{ext} = 0$. Three focal targets are chosen within the fluid domain and a 0.1 s duration waveform is derived from a FFT with 2^{12} samples. It is noted that this relatively short waveform chosen for ease of computation and longer durations could be be used for a larger transient peak. For comparison, the largest harmonic pressure is also found over all frequencies for each of the target points.

Figures 4.14 & 4.15 show the pressure field when the response at the target is at its peak for the harmonic and time reversal excitations. In the harmonic case, the cut-on frequencies of various modes generally provide the maximum pressure depending on the target location. In Figure 4.14c) for example, where the target is at $r = 0$, the maximum pressure is obtained at the cut-on of one of the higher order axisymmetric duct modes. In the previous chapter it was shown that these modes cut on with increasingly larger peaks, and have their maximum pressure at the centre of the pipe. The 'optimal' frequency in this case therefore corresponds to the highest order mode which cuts on over the bandwidth studied at 19 kHz. For Figure 4.14a), where the target is at the wall 180° from the source, the maximum pressure is obtained at 15 kHz via one of the non-axisymmetric duct modes. In 4.14c) the target is offset 90° from the source. Here the pressure field can be recognised as being dominated by the $n = 4, s = 2$ duct mode, which cuts on at a comparatively lower 7 kHz.

The variation in optimal frequency with target position, as well as the relatively low pressures obtained in the harmonic case present obvious limitations to using this form of excitation for biofouling control. It should be noted, however, that although the peak response is low, the average power flow was shown to be higher than for time reversal and the pressure field is broadly uniform around the circumference. This is most apparent in 4.14c) where there is little to no bias in the pressure field toward the focal point, and the same peak pressure is obtained over much of the pipe circumference. With the use of time reversal on the other hand, the pressure fields shown in Figure 4.15 demonstrate a narrower focal peak. The maximum response is much greater than the harmonic counterpart, and the fundamental frequency is down-shifted to just 10 Hz. This illustrates the effect of spatio-temporal focussing when using time reversal. The field in 4.15c) exhibits a double focal point due to the single actuator at $\theta = 0$ producing a symmetric field about the r-axis.

Figure 4.16 shows the maximum pressure over the entire fluid-domain when harmonic and time reversal techniques are applied with a single actuator. In the case of a harmonic excitation, the maximum response is calculated at each point over all frequencies studied. As illustrated, the comparatively lower pressure harmonic peaks exhibit little spatial preference. When time reversal is applied, the peak response is found close to the (r, θ) coordinate of the source, and along the r-axis from the source. This spatial biasing can naturally be mitigated by utilising multiple sources spaced around the pipe's circumference. In Figure 4.17, the distribution of the maximum transient response for 3 equally spaced point sources is shown, calculated according to equation 4.12. This setup is the same as a

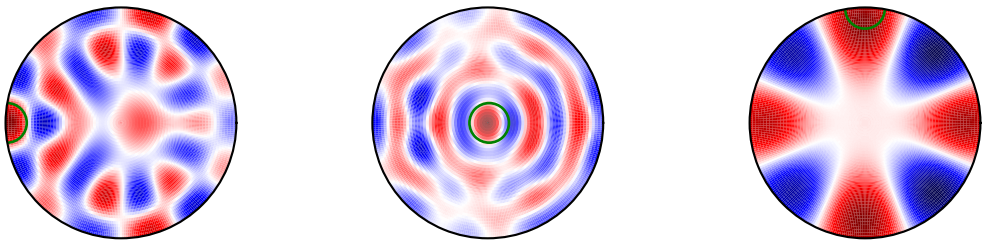

(a) 15 kHz, 36 Pa (b) 19 kHz, 49 Pa (c) 7 kHz, 33 Pa

Figure 4.14: Pressure fields for the peak harmonic response at three targets.

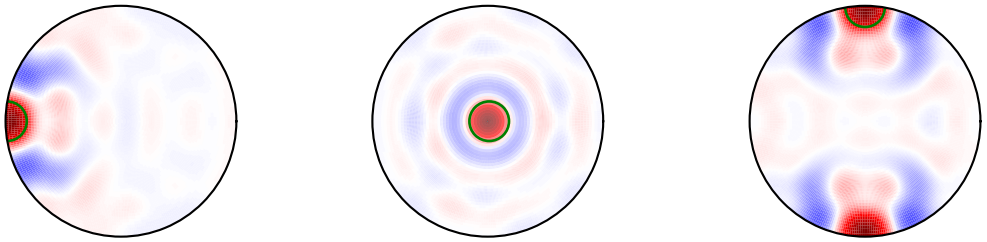

(a) 10 Hz, 545 Pa (b) 10 Hz, 357 Pa (c) 10 Hz, 375 Pa

Figure 4.15: Pressure fields for the peak transient response at three focal targets. The pulse repetition frequency in each case is 10 Hz.

'time reversal mirror' (TRM), where the impulse response at a number of 'receivers' at $x = 0$ is calculated subject to a single excitation at the focal point. Each IRF is then time-reversed and applied to the receivers, which now act as sources. In this way, the system behaves as a phased array. Since the system is reciprocal, it is sufficient to calculate the IRF at the focal point subject to each individual source in the array, after which the time-reversed waveforms can be applied correspondingly for each source and the total response found by superposition.

With such a configuration, the angular dependence of the maximum response decreases significantly. Adding yet more forces further compounds this, as in Figure 4.18, where the normalised angular profile of the pressure field at the pipe wall is plotted for various numbers of sources. It is noted that even in the case of a single actuation point, the peak response around the pipe is usually at least 70% that of its maximum value. For 3 sources, the response around the pipe does not fall below 80% of the peak. Increasing M further, the distribution grows increasingly uniform. The angular profile of the maximum harmonic response over

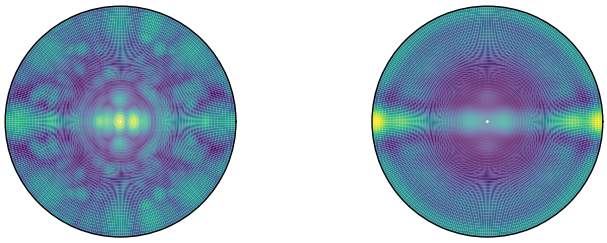

(a) (b)

Figure 4.16: Spatial dependence of the peak pressure for a) harmonic and b) transient excitations, subject to a single structural force at $\theta = 0$.

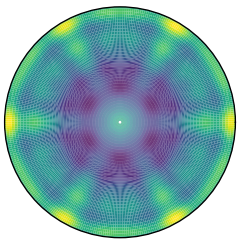

(a)

Figure 4.17: Spatial dependence of the peak pressure when applying time reversal with three equally spaced sources.

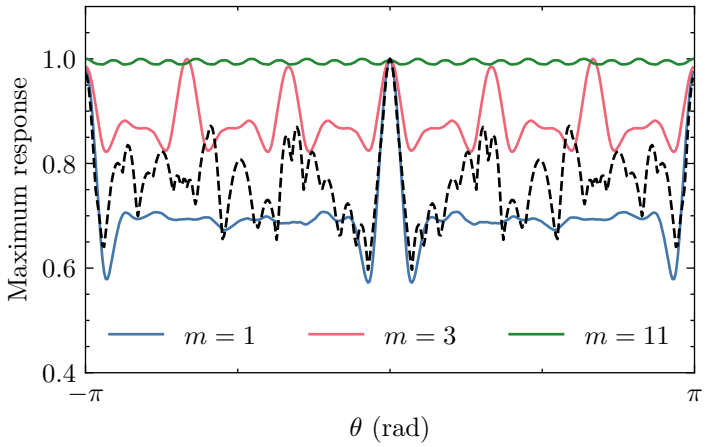

Figure 4.18: Maximum normalised pressure response around the pipe wall. Three different source numbers are used for time-reversal and the maximum harmonic response over all frequencies for a single source is shown in black.

all frequencies for a single transducer is shown (dashed) for comparison.

When considering a harmonic excitation with multiple sources, there are a number of approaches to maximising the response at a given point, and determining the 'best' technique for this purpose is not as straightforward as for the case of transient focussing. Here the problem is which frequencies and phase offsets to apply to each actuator in the array to achieve the largest possible response at a desired point.

A selected mode may be preferentially excited at resonance by selecting the phase offsets of each source at a single frequency. For example, the $n = 4, s = 2$ acoustic mode shown in Figure 4.14c) may be excited at its cut-on by configuring 8 equally spaced actuators with alternating phase offsets of 0 & 180° around the pipe. For a more general approach, the phased array technique developed by Rose et al. [110] can focus energy at a given angle using a single-frequency excitation with appropriately tuned amplitudes and phase offsets for each transducer. This method results in an angular profile which approaches a delta function at the targeted angle. Whilst this is desirable for increasing the signal-to-noise ratio for the application of non-destructive testing, the response is not maximised, since not all sources are driven with the largest possible amplitude. Additionally, the restriction that each source is driven at the same frequency is suboptimal. For the objective of maximising the harmonic response at a given point with an array of transducer, the harmonic peaks obtained at the focal point from each transducer

individually should sum together in phase at the target. Achieving such coherence between different frequencies is not trivial to implement and is highly sensitive to perturbations of the system. In any case, the maximum response with M transducers cannot in general exceed that of M times the maximum response of a single transducer. With this in mind, the transient focussing applied with a time-reversal mirror is presented as the optimal technique for maximising the response at any point.

4.4.4 Influence of Bandwidth

In the analysis so far, a frequency-independent excitation has been assumed which in this case takes the form of an ideal force source. In practice, any actuator will have a finite bandwidth of operation. This restriction will naturally reduce the performance of transient focussing. It is of importance then to analyse how a band-limited excitation affects the maximum response, and to determine the most efficient frequencies for time reversal in this system.

To study this, low and high-pass filters are applied to the system's transfer function to model the effect of an force with limited bandwidth. In each case, the filter used is a second-order Butterworth with a variable cut-off frequency, defined as the -3dB point. Time reversal focussing is applied to focus the pressure pipe wall at $\theta = 0$ for a range of distances from the source. At each distance, the cut-off frequencies of each filter are varied in steps of 1 kHz in order to adjust the bandwidth from 0 to 20 kHz. The peak response for each test is normalised by the maximum unfiltered response.

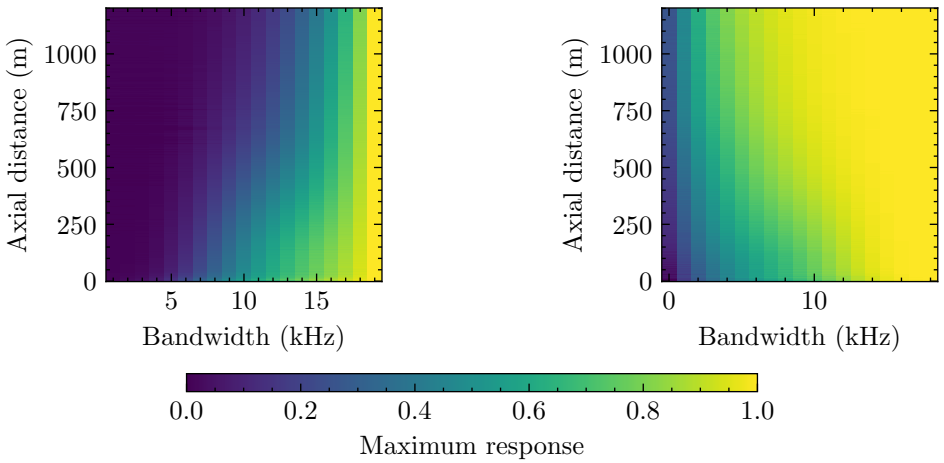

Figure 4.19: Peak transient response obtained when filtering the system with a low-pass (left) and high-pass (right) filter with variable bandwidth over various distances.

Figure 4.19 shows the results of applying the low/high-pass filters to the system with time reversal. Near the source, where the propagating waves have suffered relatively little attenuation, the focussing performance gradually increases with bandwidth with both filters. For the low-pass filter, the maximum performance is only reached at the full bandwidth for each distance. In contrast, the performance of the system with the high-pass filter applied reaches its maximum much faster as the bandwidth is increased. This is particularly pronounced at distances farther from the source, where the performance saturates after 8-10 kHz. This suggests

that the higher range of frequencies in the bandwidth studied are most important to achieving the maximum response when using transient focussing. This result is understandable when considering that the higher frequency propagated waves are better excited and less attenuated due to propagating in the fluid.

4.5 Conclusion

From the analysis of the free waves propagating for each higher mode order $n > 0$, it was found that the behaviour can be split between the frequency range above and below the cut-on frequency of the first acoustic mode. Below this frequency, the structural response of the pipe wall dominates with a single flexural mode. The first acoustic mode to cut-on for each n was found to be relatively uncoupled from the wall, as there is no coincidence in wavenumber with any structural mode. Subsequent modes to cut-on $s > 2$ behave much like the duct modes in Chapter 3, and alternate behaviour between structural and acoustic waves.

The low frequency flexural waves in the pipe wall may provide high levels of structural vibration close to the source, but are otherwise highly attenuated and thus do not propagate far from the excitation point. Instead, higher frequency waves travelling in the fluid are best suited for long range propagation.

When applying a force or acoustic source to the pipe over a sufficiently small area, the response can be modelled by a flat summation of all propagating circumferential modes over the bandwidth studied. In this case, including $n < 22$ was sufficient to capture the full response of the system up to 20 kHz in the far-field. Considering the objective of antifouling, a harmonic excitation can be used at a resonant frequency to produce high amplitude sound and vibration over a large area of the pipe wall. Additionally the harmonic excitation is presumed to inject the most power into the system, where the RMS response at a given point is maximised. At different locations of interest the optimal harmonic excitation frequency will vary. With multiple actuators, the problem of how to harmonically excite each actuator for the largest response grows more complicated.

In contrast, the 1-bit time reversal method achieves what is proposed as being the maximum possible response at a specific point, whilst reducing the average power and RMS response. The peak response in the system is also much more temporally and spatially concentrated, although it is noted that the time-reversed response is still significantly higher than the maximum harmonic response over a considerable distance from the focal point. The time reversal technique can be readily applied to multiple actuators by using the time reversal mirror (TRM) concept. An estimate of the IRF at the focal point from each transducer is all that is required to apply transient focussing.

Looking at the influence of bandwidth on the system when applying time reversal, it was found that the peak response generally grows as bandwidth increases, but the higher frequencies play a dominant role. This is understood from the previous analysis which showed that higher frequency waves, mostly fluid based, have generally lower attenuation the lower frequency waves which propagate predominantly in the structure.

5. Application of Guided Waves for Zebra Mussel Antifouling

In this chapter, a numerical experiment couples the higher-order pipe from Chapter 4 to a model of a commercially available inertial actuator. The results are compared to known biofouling studies to contextualise the work so far and draw some early conclusions of the feasibility of antifouling with sound and vibration. Firstly, the literature is compiled to give quantitative benchmarks for the levels of pressure and acceleration required to achieve antifouling. After this, the inertial actuator model is described and coupled to the outer wall of the pipe, acting as a radial point force. The harmonic and time-reversed transient responses are then assessed and compared to the given benchmarks. The results suggest that inhibitory levels of low frequency sound and vibration can be obtained at significant distances from the excitation point. Antifouling levels of pressure are shown to be easier to achieve than acceleration. The use of time reversal substantially increases the given response quantity at any point.

5.1 Quantitative Benchmarking of Mussel Antifouling Studies

In this section, the existing literature on zebra mussel control with sound and vibration is revisited to provide benchmarks for a feasibility study. The objective is to give a quantitative summary of the levels of sound and vibration which have been demonstrated to inhibit fouling in an experimental setting.

As it stands, the existing literature on vibroacoustic control of zebra mussels is relatively sparse. Nevertheless, the studies conducted so far have been promising insofar as they have repeatedly demonstrated acute effects of sound and vibration on the ability of zebra mussels to attach themselves to a substrate, and in some cases have even demonstrated the ability to kill settled mussels.

A broad literature review on this subject has already been given in Chapter 1. Here, the studies which are most relevant to the problem addressed by this project are presented in more detail and the results are compared with a numerical experiment to assess the feasibility of replicating the sound/vibration levels required for biofouling control. The studies have been divided into those which focus on acoustic pressure in the fluid, and those which deal with vibration of the substrate. It is worth noting however, that in most systems these two effects cannot be exactly separated due to the fluid-structure interaction.

5.1.1 Acoustic Pressure

The research which has been conducted so far on acoustic zebra mussel antifouling is divided between studies which use electric sparkers to generate very high amplitude pressure pulses, and those which use harmonic sound fields induced by traditional underwater actuators.

Sparkers have already been deployed in the field in some cases and appear to be effective for zebra mussel antifouling. For example Mackie et al. have conducted field experiments demonstrating massively reduced settlement rates in pipes treated with sparkers, as well as induced mortality and a reduction in mussel size [25]. Schaefer et al. note an installation where a sparker pulse applied once every 30s has 'for over four years prevented biofouling' in a 40cm diameter 550m long pipe [27]. Similarly a EPA project concluded that sparkers could prevent growth of mussels in a similar setting [28]. In most of these studies, the specifics of the pressures and bandwidths used are not forthcoming. However, Schaefer et al. quantifies the pressure in a 115m pipe with the use of such a sparker in 2010 [26]. In this case bandwidth of each pulse was approximately 100 kHz and the pressures needed to inhibit settlement of, or kill mussels, 0.04 MPa and 0.23 MPa respectively. In this study the distance protected from settlement was a more modest 23 m with a mortality distance of just 1.5 m. Since then, there appears to have been no new research conducted on the user of acoustic sparkers.

For the use of harmonic sound fields, the number of studies is even fewer. Whilst the subject of acoustic antifouling more broadly has seen substantial research, as for example in the case of barnacles [167] and other aquatic creatures, there are only two studies which stand out for measuring the effect of sound on zebra mussels. Most notably Donskoy performed a number of tests on the translocation of adult zebra mussels in the presence of low frequency underwater sound [168]. It is reported that pressures from 50-315 Pa at frequencies of 37-130 Hz were used, although exact quantities are given for only two tests. These are displayed in Table 5.1. Over the relatively short (12 - 24 hr) duration studied, the number of mussels settled on a substrate was significantly reduced. Mussel mortality, however, was not observed.

Study	Frequency	SPL re 1uPa	Duration	Result	Efficacy
Donskoy	58 Hz	170	12 hrs	Inhibition	97%
	120 Hz		24 hrs	Inhibition	93%
Schaefer	0-100 kHz pulse	227	1 month	Mortality	–
	(every 45s)	212		Inhibition	100%
Kusku	500 Hz	85	100 days	Mortality	33%
	1000 Hz	83			37%
	5000 Hz	87			45%

Table 5.1: Summary of acoustic antifouling studies performed on zebra mussels.

More recently, in 2022, Kusku et al. performed a much longer study on the effects of underwater sound on zebra mussels. This test was conducted over 100 days, using three frequencies from 500 - 5000 Hz [169]. This experiment used much lower sound levels induced by a 1.5W speaker. Compared the Donskoy study, the acoustic pressure was 2000 times lower (see Table 5.1). Over the course of the experiment, the mortality rates in the sound treated tanks steadily grew, reaching 45% after 100 days in the 5000 kHz test. Furthermore, the measured weight of

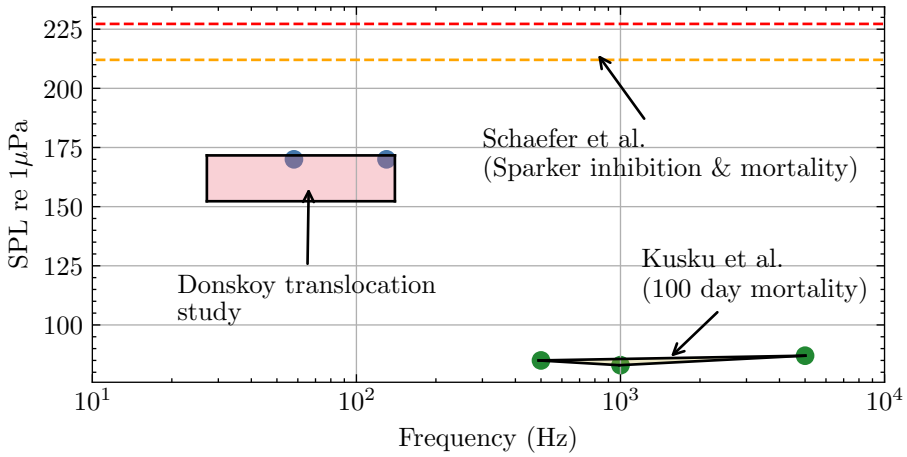

Figure 5.1: Frequency-pressure plot of acoustic antifouling studies conducted on zebra mussels.

the surviving mussels had decreased, and was significantly lower than the weight of the mussels in the control tank, which had actually increased over the same period. The authors propose that previous acoustic antifouling studies did not allow sufficient time to accurately observe the effects of sound on mussels.

Given that such low levels of sound are able to kill mussels over a long enough duration, and reduce the weight of surviving mussels, it is tentatively suggested that there may be a biological, rather than purely mechanical component to the antifouling effect observed. This might be similar to studies that showed antifouling of barnacles at particular frequencies with no observed effect on other aquatic fouling organisms [170]. At this stage, however, no strong conclusions can yet be drawn. Figure 5.1 depicts the pressure-frequency range of the three studies considered in this chapter for acoustic antifouling. The Schaefer sparker study is indicated as a horizontal line due to the broadband nature of the excitation, which was applied every 45 s.

5.1.2 Structural Vibration

There are only a few select studies which measure the effect of vibration on zebra mussels. These are namely the Donskoy study on mussel veligers [168] and the Kowalewski study on juvenile zebra mussels [171]. The results of the Donskoy study are shown in Table 5.2. Here it was demonstrated that 100% mortality could be achieved in a remarkably short time given sufficient levels of substrate borne vibration. The study by Kowalewski also showed 100% detachment rate between 8-10 kHz at vibration levels of approx. 15g, and 100% mortality at 10-12kHz at 20g.

Aside from these studies on zebra mussels, research has been performed by Roberts et al. on the sensitivity of the blue mussel (*Mytilus edulis*) to vibration of the substrate [30]. The motivation of this work was ecological. The response of the mussels to vibration was measured with valve closure, and the treatment duration was just 8 s. Still, this work is useful in providing the thresholds of vibration required to elicit a response from blue mussels, and although a different species, this work may be somewhat applicable to the zebra mussel. The results of the study are given in Table 5.3. Figure 5.2 illustrates the vibration studies which will be considered in this chapter, where it should be remembered that the

Frequency (Hz)	Vibration Level (g)	Mortality Rate (%) vs Time			
		15 min	30 min	60 min	90 min
62	0.01	48	67	97	100
160	0.5	75	88	100	100
450	6	48	70	74	97
1,000	7	54	69	83	92
8,500	8	45	52	61	61
8,500	12	33	44	61	73
9,500	78	69	84	100	100
9,500	600	98	97	100	100
16,000	23	-	32	57	54

Table 5.2: Results of vibration treatment of veligers. Reproduced from [168].

Frequency	Acceleration	Duration
5	0.07	
10	0.06	
20	0.08	
40	0.10	8s
90	0.09	
210	0.55	
410	0.12	

Table 5.3: Vibration threshold study on the blue mussel (Mytilus edulis). Measuring valve closure subject to substrate-borne vibration. Reproduced from [30]

experiment by Roberts et al. was conducted on the blue mussel and only measured valve closure. Notably there is some overlap between the studies by Donskoy and Roberts et al. However, in the case of the former the vibration was applied over many minutes to zebra mussel veligers and for the latter, vibration was applied for just 8 seconds to adult blue mussels. Additionally, the research performed by Donksoy concluded that vibration at these levels could not kill adult mussels, only veligers.

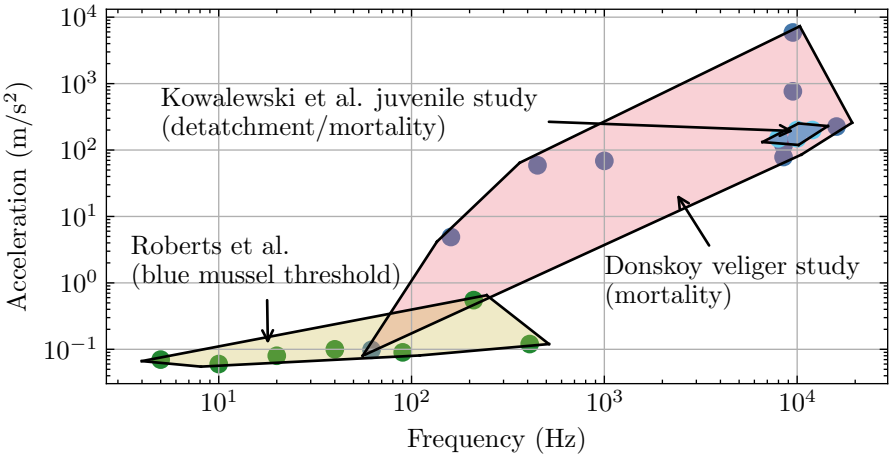

Figure 5.2: Frequency-acceleration plot of vibrational antifouling studies conducted on zebra mussels, with the inclusion of the blue mussel study by Roberts et al.

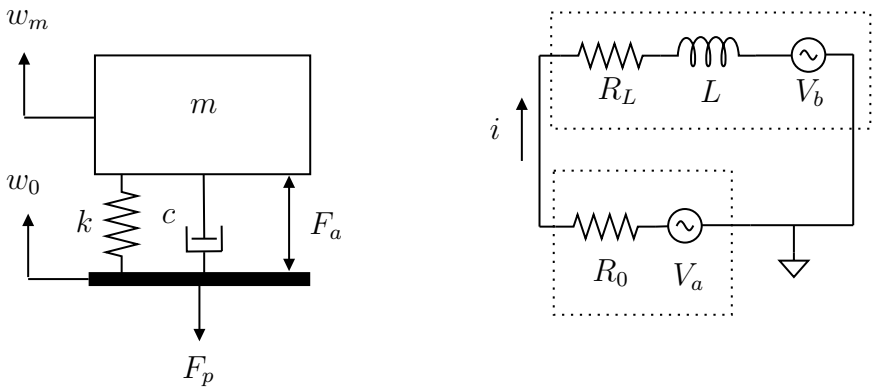

Figure 5.3: Mechanical (left) and electrical (right) subsystems of the inertial actuator model.

5.2 Structural Excitation with Inertial Actuator

In this section, the pipe system studied in Chapter 4 is coupled to a model of a commercial inertial actuator and the response is assessed with respect to the existing research of mussel antifouling. Harmonic and time reversal excitations are compared with the aim of achieving pressure and accelerations levels at frequencies demonstrated to inhibit the attachment of mussels.

5.2.1 Inertial Actuator Model

Inertial actuators (or shakers) are a common way to excite a structure with high amplitude vibration. They can be conveniently fixed with a single attachment point on any structure, and work through electromagnetic coupling between a coil and permanent magnet, which constitutes the inertial mass. Beyond its resonant frequency an inertial actuator behaves approximately as an ideal force source over a significant bandwidth when driving a much larger impedance. An inertial actuator is used in this study, as it is a typical and reliable method for exciting high amplitude, low-frequency vibrations.

Figure 5.3 shows a simplified lumped parameter model of an inertial actuator, divided into coupled mechanical and electrical circuits. The input to the system is given by the voltage source V_a with internal resistance R_0. A current i flows through the coil, modelled by an inductance L with some series resistance R_L. This current then generates a force in the mechanical system F_a due to the electromagnetic coupling.

$$F_a(\omega) = (Bl)i(\omega) \tag{5.1}$$

where B is the flux density of the permanent magnet and l the length of the coil. The product Bl is known as the voice coil coefficient. The force is generated between the permanent magnet of mass m, and the coil, which is fixed to the structure being excited. These are shown as the mass and base respectively of the mechanical circuit in Figure 5.3, and are connected through a spring of stiffness k and a dashpot with viscous damping constant c. The relative velocity between the mass and coil induces a back E.M.F into the coil such to oppose the driving voltage

$$V_b = Bl\left(\dot{w}_m - \dot{w}_0\right). \tag{5.2}$$

With these relations, the coupled system can be modelled.

Coupling Spatially the actuator is assumed to behave as a point force, with the attachment point being a few centimetres or less in diameter. Using the WFE method, the transfer function of the system subject to a structural point force $H(\omega)$ at any degree of freedom can be calculated as outlined in Chapter 4. For a given input force to the pipe F_p, the general displacements can be found with

$$Q(\omega) = H(\omega) \cdot F_p(\omega). \tag{5.3}$$

F_p is calculated considering the coupling to the shaker, and can be expressed as [127]

$$F_p(\omega) = \frac{F_p(\omega)}{F_a(\omega)} \cdot F_a(\omega). \tag{5.4}$$

The transfer function between the actuator force and the force applied to the pipe is given in terms of the relative accelerances of the pipe and actuator

$$\frac{F_p(\omega)}{F_a(\omega)} = \frac{\alpha_a(\omega)}{\alpha_0(\omega) + \alpha_a(\omega)}. \tag{5.5}$$

Here the pipe accelerance α_0 is calculated at the driving point with the WFE model. The actuator force can then be expressed in terms of the voltage

$$F_a(\omega) = \frac{F_a(\omega)}{V_a(\omega)} \cdot V_a(\omega) \tag{5.6}$$

with the corresponding force/voltage ratio given by

$$\frac{F_a(\omega)}{V_a(\omega)} = \frac{F_a(\omega)}{I_a(\omega)} \cdot \left(\frac{V_a(\omega)}{I_a(\omega)}\right)^{-1}. \tag{5.7}$$

The transfer function between the actuator force and current and the electrical impedance are given in the blocked configuration by [172]

$$\frac{F_a}{I_a} = \frac{j\omega m \cdot (Bl)}{j\omega m + c + \frac{k}{j\omega}} \quad \frac{V_a}{I_a} = (R + j\omega L) + \frac{(Bl)^2}{j\omega m + c + \left(\frac{k}{j\omega}\right)}. \tag{5.8}$$

Now the force applied to the pipe for a given input voltage can be calculated combining the prior equations

$$F_p(\omega) = \left[\frac{F_a(\omega)}{V_a(\omega)} \frac{F_a(\omega)}{I_a(\omega)} \cdot \left(\frac{V_a(\omega)}{I_a(\omega)}\right)^{-1}\right] V_a(\omega). \tag{5.9}$$

The preceding equations are calculated for the parameters shown in Table 5.4, which are based on the commercially available DataPhysics IV40 shaker [173] paired with the PA30E amplifier. With this setup, an input voltage of 10V is chosen to drive the actuator. The actuator is considered to act on the external wall of the pipe at $\theta = 0$

The pressure and acceleration at the inner pipe wall are now calculated at same transverse coordinate for a range of distances from the source. Harmonic and time-reversal excitations are used and compared for their maximum response at different frequencies. In the case of time reversal, the frequency used is the pulse repetition frequency, adjusted by varying the length of the FFT and thus the focal waveform. Once again it is emphasised that this comparison of response amplitudes is between that of a sinusoid and pulse train. The longest focal waveform duration is 0.8 seconds, with a corresponding minimum frequency of 1.25 Hz. The shortest focal waveform and highest pulse frequency are 0.75 ms and approx 1.3 kHz respectively.

Parameter	Value	Unit
m	1.21	kg
k	42992	$\mathrm{N\,m^{-1}}$
c	22.8	$\mathrm{N\,A^{-1}}$
Bl	5.6	m
R_L	1.7	Ω
R_0	3.5	Ω
L	0.298	mH

Table 5.4: Model parameters of an inertial actuator based on the DataPhysics IV40 [173]

5.2.2 Pressure Response

The pressure response for the harmonic and transient excitations are shown in Figure 5.4 along with the frequency-pressure regions from the Donskoy and Kusku studies as in Figure 5.1. Using a harmonic excitation, the pressure at the source reaches well into the range tested by Donskoy et al. Further away, the pressure drops significantly as expected, and is particularly attenuated near the ring frequency due to structural damping. Still, the SPL remains higher than the Kusku region far from the source and over a broad range of frequencies. The first low frequency peak seen in the harmonic spectra corresponds to the actuator resonance at approximately 30 Hz. The pressure here is relatively unattenuated as energy is carried through the plane wave mode in the fluid. Although the pipe is stiff to radial vibration at this frequency, indicated by the low SPL value at the input (x = 0 m), the pressure level is still within the range suggested to induce antifouling according to Kusku et al., and the low attenuation would make it suitable for this purpose at a considerable range from the source. Above the ring frequency, the pressure is dominated by the higher-order duct modes and steadily drops due to the actuator roll-off.

The focussed transient pressure response is significantly higher across all frequencies tested, and the SPL does not drop below 120 dB. Whilst the harmonic pressure can only reach the Donskoy pressure/frequency region at the input, with time-reversal focussing, a comparable SPL can be achieved at over 100 m from the source. Naturally, the SPL decreases steadily with the repetition frequency, as the length of the focal waveform and thus the potential for focussing diminishes.

A further advantage of focussing is that the maximum amplitude has a weaker dependence on frequency. Where the peak response obtained with a harmonic excitation is reliant on various resonances in the system, arising either from the cut-on of wavemodes or the actuator itself, the broadband waveform used in time reversal allows the pulse repetition frequency to be adjusted without drastically affecting the peak response. For example, the high attenuation above 1 kHz is seen to strongly filter the harmonic response in a region around the ring frequency, where the pressure drops significantly. With time reversal no such rapid drop-off is observed, as the pulse train at the focus is, by definition, mostly comprised of those frequencies which propagate with the least attenuation. It is seen then, that transient focussing can smooth out any 'bandgaps' inherent to the system. This has useful practical implications where there is an observed frequency sensitivity in fouling organisms.

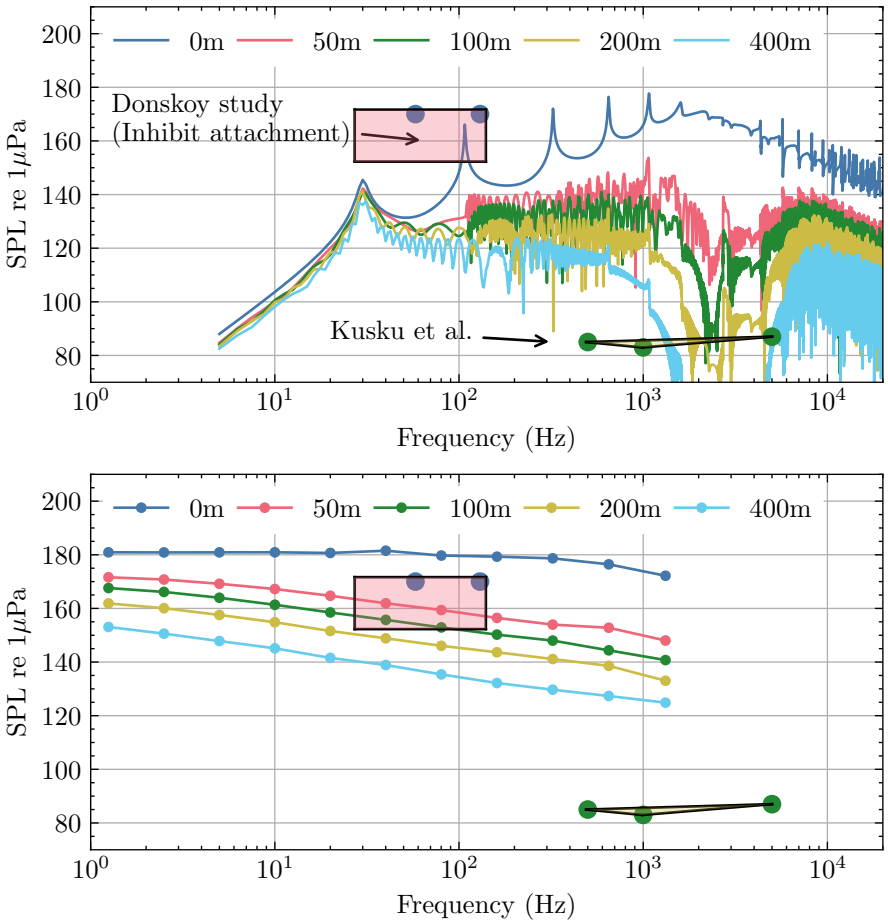

Figure 5.4: Harmonic (top) and transient time reversal (bottom) pressure spectra at various distances, compared to acoustic antifouling studies.

5.2.3 Acceleration Response

Figure 5.5 shows the same study repeated for the acceleration of the pipe wall. Overall, it is observed that the levels of acceleration required to induce antifouling are more difficult to achieve compared to those for pressure. Harmonically, the range of accelerations used in the Donskoy veliger study are only obtainable at or very close to the input. The low frequency actuator resonance reaches a level of vibration comparable to the blue mussel threshold study by Roberts at al. and the lowest frequency tested in the Donskoy zebra veliger study. It is possible that sustained vibration at the levels used in the work by Roberts et al. could lead to mortality, detachment or inhibition but this is not yet known. Going higher in frequency, the input acceleration is seen to peak at various cut-on frequencies approaching the range used by Donskoy to kill zebra mussel veligers. However, at distances farther from the source, attenuation causes the levels of acceleration to fall well beyond those observed to elicit a response or control fouling of mussels, especially at higher frequencies, where stronger vibration is required according to available research. From this it is suggested that harmonic vibration is best used at lower frequencies closer to the source.

On the other hand, using time reversal focussing yields accelerations well above those tested in antifouling studies over a significant range of distances and frequencies. With a harmonic excitation, the response at very low frequencies (< 30 Hz)

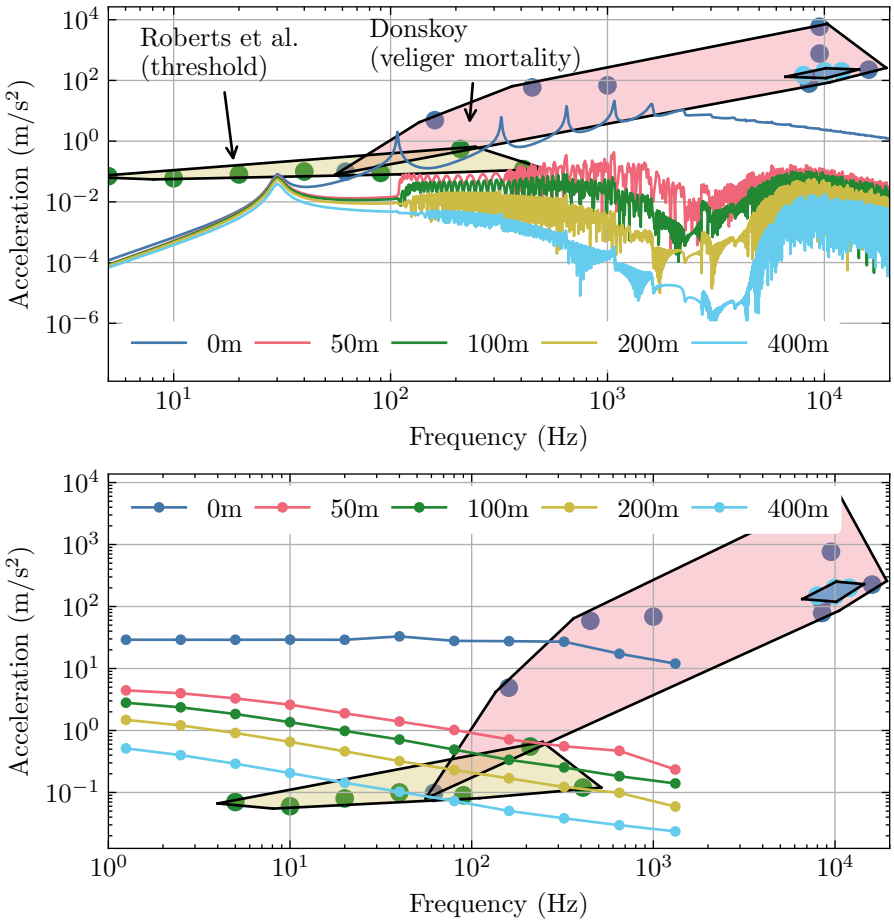

Figure 5.5: Harmonic (top) and transient time reversal (bottom) acceleration spectra at various distances, compared to acoustic antifouling studies.

in particular fell well short of even the threshold levels reported in Roberts et al. With the application of focussing, these acceleration levels are easily surpassed below 40 Hz, and this holds at 400 m from the source. Approaching 100 Hz, the acceleration at most distances is higher than that of the lowest frequency tested by Donskoy in the zebra mussel veliger study. In both the studies by Donskoy and Roberts et al. it was observed that lower frequencies required less acceleration to achieve the same intended outcome. This would compound the advantages of time reversal focussing, since lower pulse repetition frequencies lead to a higher maximum response at the focus, and so the larger peak response is further aided by the 'down-shifting' in fundamental frequency provided by the pulse train.

5.2.4 Axial Coverage

Attention is now given to the spatial coverage of pressure down the pipe axis. Only the pressure in the fluid is considered, since inhibitory levels of sound have been shown to be more achievable than acceleration. Consider a length of pipe 500 m long which requires protection from fouling. To start, a harmonic excitation is tested. The maximum pressure calculated over all frequencies is shown in Figure 5.6, along with the pressure at the actuator resonance frequency of 30 Hz. Close to the source, the optimal excitation frequency is between 1-2 kHz and the maximum pressure is obtained via the low frequency flexural modes which cut on with high

radial motion. As previously shown, these modes are strongly attenuated and as a result the maximum pressure drops quickly with distance from the source. After approximately 100 m, the flexural modes have attenuated to the point that the maximum pressure is now induced by the actuator resonance at 30 Hz. From here, the pressure drops gradually as energy is carried mostly through the fundamental acoustic wave, which is relatively unattenuated.

The maximum pressure obtained at each distance through time reversal focussing is also shown in Figure 5.6a), where the target distance is set to 100 m. At the focus there is naturally a large peak in pressure as energy converges at this point. This is shown in the time domain in Figure 5.6b) along with the maximum harmonic pressure. The gain at the focus is approximately 22. Beyond the focal point, the peak transient pressure drops quickly as the energy begins to disperse once more along the waveguide axis, and by 130 m has dropped below the maximum harmonic pressure obtained at 30 Hz. This is also shown in the time domain at 200 m in Figure 5.6c). The time reversal waveform calculated here is broadened and highly attenuated due to dispersion.

The same calculation is now repeated in Figure 5.7 for a target of 300 m. As before, the transient pressure drops quickly beyond the focal point. However, at distances before the target, the transient pressure is comparable to that of the maximum harmonic. The corresponding time domain waveforms at 200 m are shown in Figure 5.7b). Since energy is still converging at this point as waves propagate to the target position, the dispersion is somewhat compensated for.

These results indicate that, where only the peak response is of concern, time reversal has relatively few drawbacks in this scenario. Focussing at long range can still induce moderately high pressures over a significant distance before the focus, and at the focus a very high peak amplitude is produced. In practice, the 500 m length of pipe could be adequately covered by high amplitude sound through a combination of harmonic and transient excitations. Near the source in particular, a steady state harmonic excitation might achieve inhibitory levels of sound over several dozen metres. At long range, where the pressure levels have dropped due to attenuation, the use of focussing can amplify the peak pressure whilst still maintaining a relatively high response amplitude at distances leading up to the focal point.

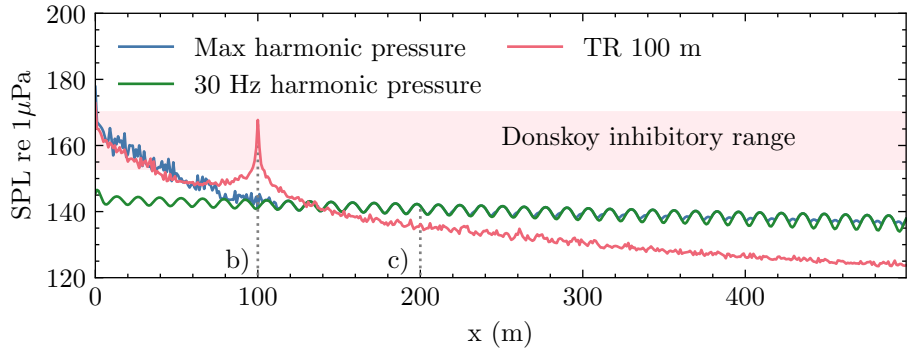

(a)

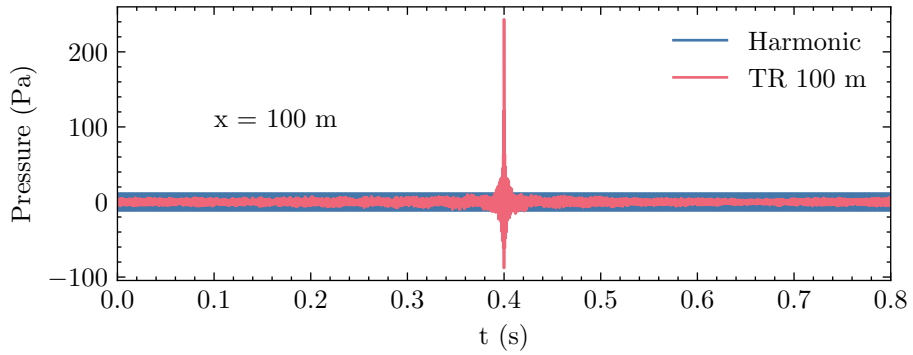

(b)

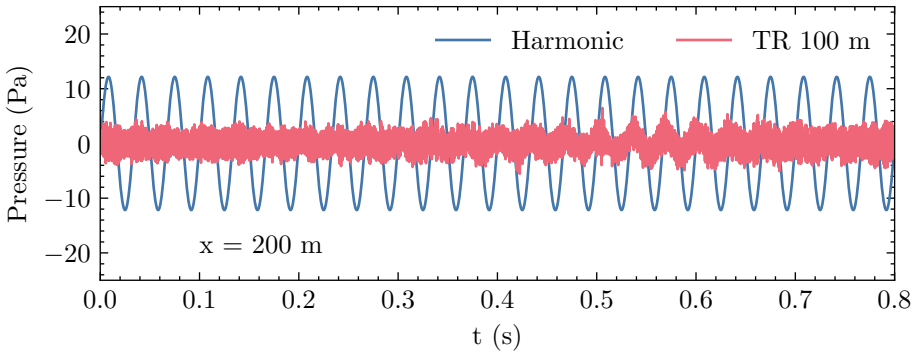

(c)

Figure 5.6: a) The maximum pressure obtained at each distance when exciting with the optimal harmonic excitation, a harmonic excitation at the actuator resonance frequency, and a time reversal waveform targeted at 100 m. b) The time domain response for the time reversal and harmonic pressures at the focus. c) The time domain response for the time reversal and harmonic pressure at 200 m, far beyond the focus.

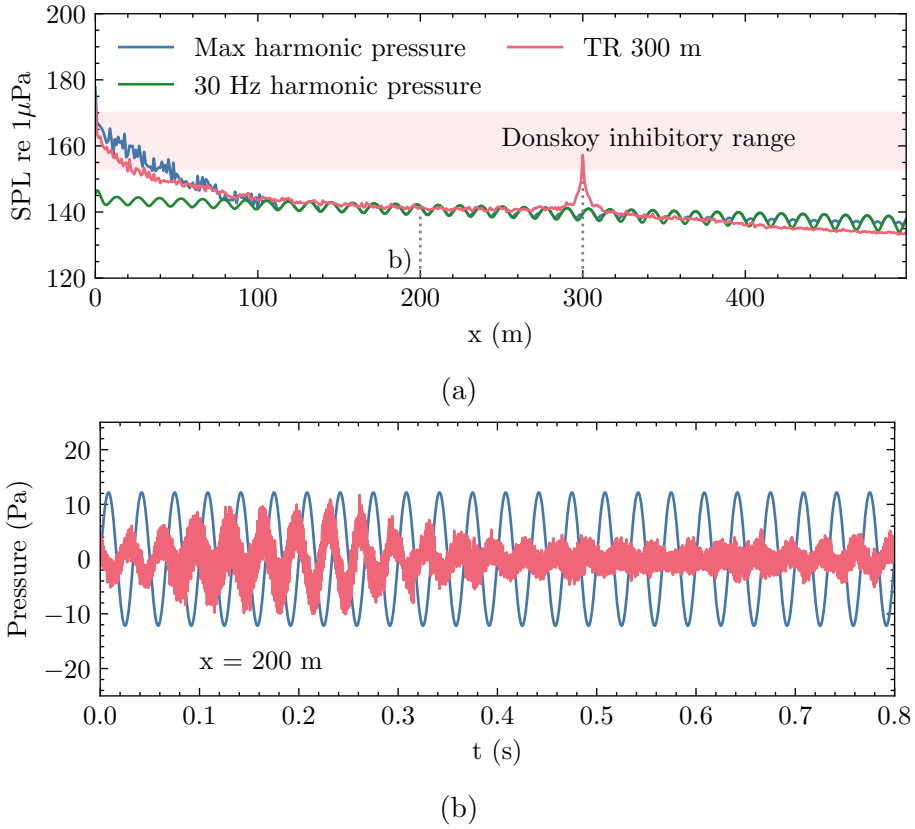

Figure 5.7: a) The maximum pressure obtained at each distance when exciting with the optimal harmonic excitation, a harmonic excitation at the actuator resonance frequency, and a time reversal waveform targeted at 300 m. b) The time domain response for the time reversal and harmonic pressure at 200 m, before the focus.

5.3 Conclusions

In this chapter, the problem of antifouling in water pipes was contextualised with a numerical experiment, coupling a commercial inertial actuator to the WFE model of a fluid-filled pipe. Antifouling studies were compiled and the levels of pressure and acceleration thought to inhibit mussel settlement were established. Both harmonic and transient time reversal excitations were assessed for their ability to reach the required response amplitudes at various distances from the source. It was shown that inhibitory levels of pressure, rather than acceleration, were more readily obtainable with both types of excitation applied to the structure. Close to the source, a low frequency (< 10 kHz) harmonic excitation was sufficient to reach antifouling levels of both pressure and acceleration. At long range, however, the harmonic response, particularly at higher frequencies, dropped significantly with distance due to energy dissipation in the structure. An exception to this was found at the actuator resonance of 30 Hz, which predominantly excited the lightly damped fundamental acoustic wave. This has promising implications for long range antifouling without the use of focussing. Although not tested in this chapter, a low frequency underwater transducer would likely be better suited to strongly excite the plane wave.

With time reversal focussing, energy was focussed at targeted points on the inner pipe wall. Instead of a sinusoid, pressure pulses were delivered at the focal point with a fundamental frequency equal to the reciprocal of the excitation waveform duration. The use of time reversal focussing was able to significantly increase the peak response amplitudes at all distances, but in particular far from the source. Various focal waveform durations were tested to show that pulse trains could be applied with a range of repetition frequencies between 1 - 1000 Hz. The optimal frequency to control mussels is currently unknown, but it is thought that lower frequencies are overall more effective.

With both types of excitation, the pressure reached in the fluid was well above that used by Kusku et al. in almost all cases. However, the pressure levels tested by Donskoy in his 12 hour study were only reached at long range (< 50 m) through the use of focussing. For the structural acceleration of the pipe wall, amplitudes which are lethal to mussel veligers could be achieved only at the source with a harmonic excitation. Again, focussing allowed these levels to be reached much farther from the source, up to 200 m away.

The spatial distribution of pressure was evaluated down the pipe axis to assess how a long stretch of pipe might be protected from fouling. A 500 m long section was considered and harmonic and time reversal excitations were applied. An SPL of > 130 was reached over the entire length by driving the system harmonically at the actuator resonance, which was well above the levels used in the Kusku study, but lower than the SPL range tested in the Donskoy translocation study. By contrast, time reversal allowed the Donskoy levels to be reached at targeted points over 300 m from the source. It was shown that when using time reversal, the pressure dropped quickly beyond the focal point due to dispersion. However, before the focal point, whilst energy was still converging along the axis, the pressure amplitude was comparable to that of the maximum harmonic response. In the example shown, an SPL of nearly 160 could be reached at a focal point 300 m away, whilst still maintaining an SPL > 140 over all distances before the target.

6. Conclusions

6.1 Summary of Present Work

In the introduction, the problem of invasive mussel fouling was outlined, in particular emphasising the physical impact on freshwater intake pipes and associated economic costs. Various existing control strategies have been reviewed, however as of yet, there exists no definitive solution that is effective, specific and can be continuously applied. At present, the most promising treatments appear to be BioBullets and Zequanox, but neither of these can be applied continuously.

Among the many control techniques detailed were those which used fluid-borne sound or structure-borne vibration to either prevent the settlement of mussels or kill them outright. A number of studies were reviewed which showed promise in treating mussel fouling. The exact antifouling mechanism is still unknown, but lower frequencies were shown to be more effective, and rather modest levels of sound were found to be inhibitory and even lethal over a long enough treatment time.

Given the specific problem of mussel fouling in water intake pipes, it was posited that guided waves could be used to protect large sections of pipe from fouling. Since energy is confined to propagate in mostly one direction, guided waves can travel long distances with low attenuation, a property which is exploited in the fields of non-destructive testing and leak detection. The theory of wave propagation in fluid-filled pipes was thus reviewed, from elementary analytical models up to the contemporary numerical methods.

After this, the means by which the sound or vibration levels could be maximised in the pipe were reviewed. In particular, dispersion compensation and/or time reversal have stood out as techniques which can significantly increase the peak response amplitude at a targeted position. Specifically, 1-bit/clipped time reversal was suggested as the most promising method of maximising the response. This technique exploits the dispersion in the pipe system to amplify, rather than attenuate a broadband excitation as energy propagates down the axis.

In Chapter 2, the problem was approached by considering only the fluid, and a simple analytical theory was used to model the system as a rigid duct driven by a monopole point source. After detailing the free wave propagation in the system, the harmonic response was assessed with the aim of maximising the pressure at the duct wall. It was shown that the interference of multiple dispersive modes makes it difficult to select an optimal excitation frequency to maximise the pressure over a long length of the waveguide. The time reversal method was then introduced, in particular the 1-bit/clipped time reversal method which was suggested as the means of maximising the peak pressure at any point. A broadband transient

excitation designed from the system's impulse response was used to focus energy at the target, resulting in a large amplitude pressure pulse. The peak pressure obtained through time reversal was many times higher than that which could be achieved through a steady state harmonic excitation, but the RMS pressure was reduced. The relative merits of time reversal focussing were discussed, and further modifications to the technique were explored, such as changing the length of the excitation waveform to change the pulse repetition frequency at the target.

In Chapter 3, the Wave Finite Element (WFE) method was used to model a fully-coupled fluid-filled pipe system in the axisymmetric mode of vibration only. First the WFE model of the system was introduced and validated. The free waves were analysed and idealised structural and acoustic excitations were used to investigate the forced response. Particular attention was given to the energy distribution between the fluid and structure and the attenuation of different propagating modes, with the aim of determining the optimal bandwidth and type of excitation for long range application of antifouling. The results showed that waves propagating in the fluid, rather than the structure, were best suited to propagation at long range. Waves with a high degree of radial motion in the structure were highly attenuated, particularly around the ring frequency. At higher frequencies the system was shown to increasingly behave like a rigid duct. Time reversal was applied to the pipe and showed similar performance to the duct system in Chapter 2. A parametric study on damping was also performed which showed time reversal could mitigate the unwanted effects of energy dissipation in the system.

After concluding the analysis of the axisymmetric system, Chapter 4 detailed a similar study, performed on the non-axisymmetric system with all higher-order propagating waves. Once again, waves in the fluid were less attenuated and could propagate much farther from the source than waves in the structure. The low frequency set of flexural waves in the pipe wall were shown to have potential for antifouling close to the source, but were otherwise strongly attenuated at long range. With the higher-order system, the response to one or more point sources was analysed in order to demonstrate the application of a phased array. The optimal bandwidth for focussing was assessed.

Finally, the preceding work was put into the context of antifouling in Chapter 5, by coupling the higher-order system to a model of a commercially available inertial actuator. Existing biofouling studies were compiled and the levels of sound and vibration shown to inhibit fouling were compared to those achievable in the coupled system. Inhibitory response levels were obtainable over significant distances with both harmonic and transient excitations, but use of time reversal extended the maximum range significantly, as well as the peak response at any given point. Further to this, the time reversal response amplitude at distances before the focus was comparable to the maximum harmonic response. This demonstrated that time reversal could be used to target a single point at long range without significantly compromising the spatial coverage before the focus.

6.2 Implications for Antifouling and Suggestions for Future Work

The work so far has shown some tentative but encouraging results for applying sound and vibration to control biofouling of zebra mussels. Close to the excitation point, antifouling levels of sound and vibration should be readily achievable with

either a structural or underwater actuator. The range at which these levels can be obtained from the source is still largely unknown and will depend strongly on the specifics of the system. It was shown in this work that, in an unburied pipe, the structural waves are most attenuated. In practice, this would be further compounded by surrounding media in a buried pipe or other constraints such as pipe flanges and supports. Use of the acoustic waves in the fluid would therefore offer the best approach to antifouling at long range. For this, the mostly non-dispersive fundamental acoustic wave could be used at low frequencies with a harmonic excitation. Otherwise, focussing could be applied with the higher-order acoustic modes above the ring frequency. In either case, strong coupling between the pipe wall and fluid is undesirable for long range power transfer.

For future work on this project, it is recommended that experiments are performed on water intake pipes which mirror the studies in this thesis. The following is suggested:

- Measurement of the long range frequency response in a real intake pipe system to provide insight into the optimal bandwidth to use for antifouling. If possible, both pressure and acceleration should be measured, however, the fluid pressure is likely to be of greater importance. It should be noted that only frequencies below 20 kHz have been widely tested for controlling zebra mussel fouling.

- Subsequent choice of actuator based on the pipe frequency response. The actuator should be either narrowband, to harmonically excite a particular frequency, or broadband, with which the time reversal focussing technique presented in this thesis can be used.

- Assessment of the response levels and range achieved with the chosen actuator in an intake pipe, with comparison to the biofouling studies outlined in this thesis.

- If inhibitory levels of sound and vibration are possible to achieve over a considerable range, a field trial should be conducted in a pipe heavily affected by mussel fouling to ultimately determine the feasibility of this antifouling strategy.

Bibliography

[1] B. J. Little and J. R. Depalma, "Marine Biofouling," in *Treatise on Materials Science & Technology*, vol. 28, pp. 89–119, Elsevier, 1988.

[2] Woods Hole Oceanographic Institution., United States., Department of the Navy., and Bureau of Ships., *Marine Fouling and Its Prevention*. Annapolis: United States Naval Institute, 1952.

[3] M. P. Schultz, "Effects of coating roughness and biofouling on ship resistance and powering," vol. 23, no. 5-6, pp. 331–341, 2007.

[4] T. Munk, D. Kane, and D. Yebra, "The effects of corrosion and fouling on the performance of ocean-going vessels: A naval architectural perspective," in *Advances in Marine Antifouling Coatings and Technologies*, pp. 148–176, Elsevier, 2009.

[5] L. E. Burlakova, A. Y. Karatayev, and D. K. Padilla, "Changes in the distribution and abundance of Dreissena polymorpha within lakes through time," *Hydrobiologia*, vol. 571, pp. 133–146, Nov. 2006.

[6] J. D. Ackerman, B. Sim, S. J. Nichols, and R. Claudi, "A review of the early life history of zebra mussels Dreissena polymorpha: Comparisons with marine bivalves," *Canadian Journal of Zoology*, vol. 72, pp. 1169–1179, July 1994.

[7] S. M. Bartell, Y. Wu, S. K. Nair, J. Orr, and J. Ragland, "Risk Assessment and Decision Analysis Support for Invasive Mussel Management for the St. Croix Basin and Adjacent Upper Mississippi River," tech. rep., E2 Consulting Engineers/URS Group, 2007.

[8] S. M. Peyer, A. J. McCarthy, and C. E. Lee, "Zebra mussels anchor byssal threads faster and tighter than quagga mussels in flow," *Journal of Experimental Biology*, vol. 212, pp. 2027–2036, July 2009.

[9] B. A. Stein, S. R. Flack, N. S. Rousmaniere, and M. G. Rollins, "Alien Species Invasions of U.S. Ecosystems," p. 36.

[10] P. A. Berkman, M. A. Haltuch, E. Tichich, D. W. Garton, G. W. Kennedy, J. E. Gannon, S. D. Mackey, J. A. Fuller, and D. L. Liebenthal, "Zebra mussels invade Lake Erie muds," *Nature*, vol. 393, pp. 27–28, May 1998.

[11] D. C. Aldridge, P. Elliott, and G. D. Moggridge, "The recent and rapid spread of the zebra mussel (Dreissena polymorpha) in Great Britain," *Biological Conservation*, vol. 119, pp. 253–261, Sept. 2004.

[12] P. Elliott, David. C. Aldridge, G. D. Moggridge, and M. Chipps, "The Increasing Effects of Zebra Mussels on Water Installations in England," *Water and Environment Journal*, vol. 19, pp. 367–375, Dec. 2005.

[13] C. Duigan, M. Dunbar, D. Gilvear, A. Gurnell, A. Jenkins, A. Large, B. Moss, J. Newman, A. Robertson, M. Ross, J. Rowan, M. Shepherd, A. Skinner, J. Thompson, I. Vaughan, and R. Ward, "Freshwaters – Openwaters, Wetlands and Floodplains," *Technical Report*, p. 67.

[14] "Invasive quagga mussel found at Rutland Water and River Trent," *BBC News*, Nov. 2020.

[15] S. Hallstan, U. Grandin, and W. Goedkoop, "Current and modeled potential distribution of the zebra mussel (Dreissena polymorpha) in Sweden," *Biological Invasions*, vol. 12, pp. 285–296, Jan. 2010.

[16] G. Van der Velde, A. Bij de Vaate, and S. Rajagopal, "The Zebra Mussel in Europe," *Annals of The Rheumatic Diseases*, 2010.

[17] I. A. N. S. Taskforce, "Estimated Potential Economic Impact of Zebra and Quagga Mussel Introduction into Idaho," tech. rep., Idaho Invasive Species Council, 2009.

[18] N. A. Connelly, C. R. O'Neill, B. A. Knuth, and T. L. Brown, "Economic Impacts of Zebra Mussels on Drinking Water Treatment and Electric Power Generation Facilities," *Environmental Management*, vol. 40, pp. 105–112, July 2007.

[19] Y. J. Passamaneck, "Literature Review and Synthesis of Invasive Mussel Control Techniques," tech. rep., U.S Department of the Interior, 2008.

[20] G. L. Mackie and Ontario, eds., *The Zebra Mussel, Dreissena Polymorpha: A Synthesis of European Experiences and a Preview for North America*. Ottawa: Ontario Environment, 1990.

[21] "Millbrook Quarry Zebra Mussel and Quagga Mussel Eradication," tech. rep., U.S Fish and Wildlife Service, 2005.

[22] *Microencapsulated BioBullets for the Control of Biofouling Zebra Mussels*.

[23] B. Murawski, "Zequanox: A Potential Solution to Zebra Mussels," vol. 7, p. 5, 2016.

[24] M. Legg, M. Yücel, I. Garcia de Carellan, V. Kappatos, C. Selcuk, and T. Gan, "Acoustic methods for biofouling control: A review," *Ocean Engineering*, vol. 103, pp. 237–247, July 2015.

[25] G. L. Mackie, P. Lowery, and C. Cooper, "Plasma Pulse Technology to Control Zebra Mussel Biofouling:," tech. rep., Defense Technical Information Center, Fort Belvoir, VA, Dec. 2000.

[26] R. Schaefer, R. Claudi, and M. Grapperhaus, "Control of zebramussels using sparker pressure pulses," *Journal - American Water Works Association*, vol. 102, pp. 113–122, Apr. 2010.

[27] R. B. Schaefer, "Pulsed Acoustic Sparker Bio-Fouling Control in Heat Transfer Equipment:," tech. rep., Defense Technical Information Center, Fort Belvoir, VA, Oct. 2002.

[28] ORD. US EPA, "Final Report | Nontoxic Sparker Control of Zebra Mussels | Research Project Database | Grantee Research Project | ORD | US EPA." https://cfpub.epa.gov/ncer_abstracts/index.cfm/fuseaction/display.abstractDetail/abstract_id 2001.

[29] D. M. Donskoy, M. Ludyanskiy, and D. A. Wright, "Effects of sound and ultrasound on Zebra Mussels.," *The Journal of the Acoustical Society of America*, vol. 99, pp. 2577–2603, Apr. 1996.

[30] L. Roberts, S. Cheesman, T. Breithaupt, and M. Elliott, "Sensitivity of the mussel Mytilus edulis to substrate-borne vibration in relation to anthropogenically generated noise," *Marine Ecology Progress Series*, vol. 538, pp. 185–195, Oct. 2015.

[31] J. D. Garrett, "Garrettj403/SciencePlots," Sept. 2021.

[32] S. C. Olisa, M. A. Khan, and A. Starr, "Review of Current Guided Wave Ultrasonic Testing (GWUT) Limitations and Future Directions," *Sensors*, vol. 21, p. 811, Jan. 2021.

[33] J. W. S. B. Rayleigh, *The Theory of Sound*. Macmillan, 1894.

[34] K. Graff, *Wave Motion in Elastic Solids*. Dover Books on Physics Series, Dover Publications, 1991.

[35] L. Cremer, M. Heckl, and B. A. T. Petersson, *Structure-Borne Sound: Structural Vibrations and Sound Radiation at Audio Frequencies*. Berlin Heidelberg: Springer-Verlag, 3 ed., 2005.

[36] M. C. Junger and D. Feit, "Sound structures and their interaction." http://hdl.handle.net/1721.1/1740, 2002.

[37] A. Love, *A Treatise on the Mathematical Theory of Elasticity*, vol. 1. 1892.

[38] C. A. Truesdell and L. Euler, *The Rational Mechanics of Flexible or Elastic Bodies: 1638-1788 : Introduction to Leonhardi Euleri Opera Omnia Vol. X et XI Seriei Secundae*. Turici; Zürich: Venditioni exponunt Orell Füssli(IS) Füssli., 1960.

[39] P. S. P. Timoshenko, "LXVI. On the correction for shear of the differential equation for transverse vibrations of prismatic bars," *The London, Edinburgh, and Dublin Philosophical Magazine and Journal of Science*, vol. 41, pp. 744–746, May 1921.

[40] F. J. Fahy and P. Gardonio, *Sound and Structural Vibration: Radiation, Transmission and Response*. Elsevier, Jan. 2007.

[41] H. Lamb, "On waves in an elastic plate," *Proceedings of the Royal Society*, vol. 93, pp. 114–128, 1917.

[42] A. W. Leissa, *Vibrations of Thin Shells*. 1973.

[43] L. H. Donnell, "Stability of Thin-Walled Tubes Under Torsion." https://digital.library.unt.edu/ark:/67531/metadc66136/m1/7/, May 1933.

[44] W. Flügge, *Stresses in Shells*. Berlin Heidelberg: Springer-Verlag, 2 ed., 1973.

[45] E. H. Kennard, "The new approach to shell theory-Circular cylinders," *JOURNAL OF APPLIED MECHANICS-TRANSACTIONS OF THE ASME*, vol. 20, no. 1, pp. 33–40, 1953.

[46] J. E. Greenspon, "Vibrations of a Thick-Walled Cylindrical Shell—Comparison of the Exact Theory with Approximate Theories," *The Journal of the Acoustical Society of America*, vol. 32, pp. 571–578, May 1960.

[47] P. W. Smith, "Phase Velocities and Displacement Characteristics of Free Waves in a Thin Cylindrical Shell," *The Journal of the Acoustical Society of America*, vol. 27, pp. 1065–1072, Nov. 1955.

[48] T. C. Lin and G. W. Morgan, "Wave Propagation through Fluid Contained in a Cylindrical, Elastic Shell," *The Journal of the Acoustical Society of America*, vol. 28, pp. 1165–1176, Nov. 1956.

[49] C. Fuller and F. J. Fahy, "Characteristics of Wave Propagation and Energy Distributions in Cylindrical Elastic Shells Filled With Fluid," *Journal of Sound and Vibration*, vol. 81, no. 4, pp. 501–508, 1981.

[50] D. Jong, "Analysis of pulsations and vibrations in fluid-filled pipe systems," 1994.

[51] B. J. Brevart, *Active Control of Coupled Wave Propagation in Fluid-Filled Elastic Cylindrical Shells*. PhD thesis, Virginia Polytechnic Institute and State University, 1994.

[52] C. R. Fuller, "The effects of wall discontinuities on the propagation of flexural waves in cylindrical shells," *Journal of Sound and Vibration*, vol. 75, pp. 207–228, Mar. 1981.

[53] C. R. Fuller, "The input mobility of an infinite circular cylindrical elastic shell filled with fluid," *Journal of Sound and Vibration*, vol. 87, pp. 409–427, Apr. 1983.

[54] C. R. Fuller, "Monopole excitation of vibrations in an infinite cylindrical elastic shell filled with fluid," *Journal of Sound and Vibration*, vol. 96, pp. 101–110, Sept. 1984.

[55] C. R. Fuller, "Radiation of sound from an infinite cylindrical elastic shell excited by an internal monopole source," *Journal of Sound and Vibration*, vol. 109, pp. 259–275, Sept. 1986.

[56] G. Pavić, "Vibrational energy flow in elastic circular cylindrical shells," *Journal of Sound and Vibration*, vol. 142, pp. 293–310, Oct. 1990.

[57] G. Pavić, "Vibroacoustical energy flow through straight pipes," *Journal of Sound and Vibration*, vol. 154, pp. 411–429, May 1992.

[58] L. Pochhammer, "Über die Fortpflanzungsgeschwindigkeiten kleiner Schwingungen in einem unbegrenzten isotropen Kreiscylinder.," *Journal für die reine und angewandte Mathematik*, vol. 81, pp. 324–336, 1876.

[59] C. Chree, "Longitudinal vibrations of a circular bar," *Quarterly Journal of Mathematics*, vol. 21, pp. 287–289, 1886.

[60] D. C. Gazis, "Three-Dimensional Investigation of the Propagation of Waves in Hollow Circular Cylinders. II. Numerical Results," *The Journal of the Acoustical Society of America*, vol. 31, pp. 573–578, May 1959.

[61] D. C. Gazis, "Three-Dimensional Investigation of the Propagation of Waves in Hollow Circular Cylinders. I. Analytical Foundation," *The Journal of the Acoustical Society of America*, vol. 31, pp. 568–573, May 1959.

[62] T. Meeker and A. Meitzler, "Guided Wave Propagation in Elongated Cylinders and Plates," in *Physical Acoustics*, pp. 111–167, Elsevier, 1964.

[63] H. D. McNiven, A. H. Shah, and J. L. Sackman, "Axially Symmetric Waves in Hollow, Elastic Rods: Part I," *The Journal of the Acoustical Society of America*, vol. 40, pp. 784–792, Oct. 1966.

[64] H. D. McNiven, A. H. Shah, and J. L. Sackman, "Axially Symmetric Waves in Hollow, Elastic Rods: Part I," *The Journal of the Acoustical Society of America*, vol. 40, pp. 784–792, Oct. 1966.

[65] R. Kumar, "Axially Symmetric Vibrations of a Thin Cylindrical Elastic Shell Filled with Nonviscous, Compressible Fluid," p. 5, 1966.

[66] R. Kumar, "Flexural Vibrations of Fluid-Filled Circular Cylindrical Shells," vol. 24, p. 10, 1971.

[67] R. Kumar, "Dispersion of Axially Symmetric Waves in Empty and Fluid-Filled Cylindrical Shells," vol. 27, p. 13, 1972.

[68] V. A. D. Grosso, "Analysis of Multimode Acoustic Propagation in Liquid Cylinders with Realistic Boundary Conditions- Application to Sound Speed and Absorption Measurements," vol. 24, p. 13, 1971.

[69] J. L. Rose, *Ultrasonic Guided Waves in Solid Media*. Cambridge: Cambridge University Press, 2014.

[70] W. T. Thomson, "Transmission of Elastic Waves through a Stratified Solid Medium," *Journal of Applied Physics*, vol. 21, pp. 89–93, Feb. 1950.

[71] N. A. Haskell, "The dispersion of surface waves on multilayered media," in *Vincit Veritas: A Portrait of the Life and Work of Norman Abraham Haskell, 1905–1970* (A. Ben-Menahem, ed.), pp. 86–103, Washington, D. C.: American Geophysical Union, 1990.

[72] L. Knopoff, "A matrix method for elastic wave problems," *Bulletin of the Seismological Society of America*, vol. 54, pp. 431–438, Feb. 1964.

[73] M. Lowe, "Matrix techniques for modeling ultrasonic waves in multilayered media," *IEEE Transactions on Ultrasonics, Ferroelectrics, and Frequency Control*, vol. 42, pp. 525–542, July 1995.

[74] J. Barshinger and J. Rose, "Guided wave propagation in an elastic hollow cylinder coated with a viscoelastic material," *IEEE Transactions on Ultrasonics, Ferroelectrics, and Frequency Control*, vol. 51, pp. 1547–1556, Nov. 2004.

[75] B. Pavlakovic, M. Lowe, D. Alleyne, and P. Cawley, "Disperse: A General Purpose Program for Creating Dispersion Curves," in *Review of Progress in Quantitative Nondestructive Evaluation: Volume 16A* (D. O. Thompson and D. E. Chimenti, eds.), Review of Progress in Quantitative Nondestructive Evaluation, pp. 185–192, Boston, MA: Springer US, 1997.

[76] B. N. Paviakovic, "Leaky Guided Ultrasonic Waves in NDT," p. 228.

[77] A. M. A. Huber, *Numerical Modeling of Guided Waves in Anisotropic Composites with Application to Air Coupled Ultrasonic Inspection*. PhD thesis, Universität Augsburg, 2020.

[78] L. Wang and S. Rokhlin, "Stable reformulation of transfer matrix method for wave propagation in layered anisotropic media," *Ultrasonics*, vol. 39, pp. 413–424, Oct. 2001.

[79] S. I. Rokhlin and L. Wang, "Stable recursive algorithm for elastic wave propagation in layered anisotropic media: Stiffness matrix method," *The Journal of the Acoustical Society of America*, vol. 112, pp. 822–834, Sept. 2002.

[80] J. He, C. Zhou, L. Yang, and X. Sun, "Research on Pipeline Damage Imaging Technology Based on Ultrasonic Guided Waves," *Shock and Vibration*, vol. 2019, pp. 1–18, July 2019.

[81] M.-f. Zheng, C. Lu, G.-z. Chen, and P. Men, "Modeling Three-dimensional Ultrasonic Guided Wave Propagation and Scattering in Circular Cylindrical Structures using Finite Element Approach," *Physics Procedia*, vol. 22, pp. 112–118, 2011.

[82] W. Luo and J. L. Rose, "Phased array focusing with guided waves in a viscoelastic coated hollow cylinder," *The Journal of the Acoustical Society of America*, vol. 121, pp. 1945–1955, Apr. 2007.

[83] W. Luo, J. L. Rose, J. K. V. Velsor, and J. Mu, "Phased-Array Focusing with Longitudinal Guided Waves in a Viscoelastic Coated Hollow Cylinder," p. 10, 2006.

[84] S. G. Johnson, "Notes on Perfectly Matched Layers (PMLs)," p. 18.

[85] P. E. Lagasse, "Higher-order finite-element analysis of topographic guides supporting elastic surface waves," *Journal of the Acoustical Society of America*, vol. 53, p. 1116, 1973.

[86] B. Aalami, "Waves in Prismatic Guides of Arbitrary Cross Section," *Journal of Applied Mechanics*, vol. 40, pp. 1067–1072, Dec. 1973.

[87] L. Gavrić, "Computation of propagative waves in free rail using a finite element technique," *Journal of Sound and Vibration*, vol. 185, pp. 531–543, Aug. 1995.

[88] I. Bartoli, A. Marzani, F. Lanza di Scalea, and E. Viola, "Modeling wave propagation in damped waveguides of arbitrary cross-section," *Journal of Sound and Vibration*, vol. 295, pp. 685–707, Aug. 2006.

[89] M. K. Kalkowski, J. M. Muggleton, and E. Rustighi, "Axisymmetric semi-analytical finite elements for modelling waves in buried/submerged fluid-filled waveguides," *Computers & Structures*, vol. 196, pp. 327–340, Feb. 2018.

[90] M. Castaings and M. Lowe, "Finite element model for waves guided along solid systems of arbitrary section coupled to infinite solid media," *The Journal of the Acoustical Society of America*, vol. 123, pp. 696–708, Feb. 2008.

[91] P. Zuo and Z. Fan, "SAFE-PML approach for modal study of waveguides with arbitrary cross sections immersed in inviscid fluid," *Journal of Sound and Vibration*, vol. 406, pp. 181–196, Oct. 2017.

[92] P. Wilcox, "Dispersion and excitability of guided acoustic waves in isotropic beams with arbitrary cross section," in *AIP Conference Proceedings*, vol. 615, (Brunswick, Maine (USA)), pp. 203–210, AIP, 2002.

[93] M. V. Predoi, M. Castaings, B. Hosten, and C. Bacon, "Wave propagation along transversely periodic structures," *The Journal of the Acoustical Society of America*, vol. 121, pp. 1935–1944, Apr. 2007.

[94] D. R. Thakare, A. Abid, D. Pereira, J. Fernandes, P. Belanger, and P. Rajagopal, "Semi-analytical finite-element modeling approach for guided wave assessment of mechanical degradation in bones," *International Biomechanics*, vol. 4, pp. 17–27, Jan. 2017.

[95] B. Ajit, "How to Use Dispersion Curves to Analyze Fluid-Filled Pipes," 2017.

[96] *Structural Mechanics Module User's Guide*. COMSOL, 2019.

[97] P. Bocchini, A. Marzani, and E. Viola, "Graphical User Interface for Guided Acoustic Waves," *Journal of Computing in Civil Engineering*, vol. 25, pp. 202–210, May 2011.

[98] D. Duhamel, B. Mace, and M. Brennan, "Finite element analysis of the vibrations of waveguides and periodic structures," *Journal of Sound and Vibration*, vol. 294, no. 1-2, pp. 205–220, 2003.

[99] B. R. Mace, D. Duhamel, M. J. Brennan, and L. Hinke, "Finite element prediction of wave motion in structural waveguides," *The Journal of the Acoustical Society of America*, vol. 117, pp. 2835–2843, May 2005.

[100] WJ. Zhou and MN. Ichchou, "Wave scattering by local defect in structural waveguide through wave finite element method," *Structural Health Monitoring*, vol. 10, pp. 335–349, July 2011.

[101] B. R. Mace and E. Manconi, "Modelling wave propagation in two-dimensional structures using finite element analysis," *Journal of Sound and Vibration*, vol. 318, pp. 884–902, Dec. 2008.

[102] W. J. Zhou, M. N. Ichchou, and O. Bareille, "Finite element techniques for calculations of wave modes in one-dimensional structural waveguides," *Structural Control and Health Monitoring*, vol. 18, no. 7, pp. 737–751, 2011.

[103] W. A. K. Deutsch, A. Cheng, and J. D. Achenbach, "Self-Focusing of Rayleigh Waves and Lamb Waves with a Linear Phased Array," *Research in Nondestructive Evaluation*, vol. 9, pp. 81–95, Jan. 1997.

[104] L. Yu and V. Giurgiutiu, "In situ 2-D piezoelectric wafer active sensors arrays for guided wave damage detection," *Ultrasonics*, vol. 48, pp. 117–134, Apr. 2008.

[105] V. T. Rathod, N. Chakraborty, and D. R. Mahapatra, "Linear phased array of piezoelectric transducers for delamination monitoring in a composite laminate using Lamb waves," p. 10.

[106] Ł. Ambroziński, T. Stepinski, and T. Uhl, "Efficient tool for designing 2D phased arrays in lamb waves imaging of isotropic structures," *Journal of Intelligent Material Systems and Structures*, vol. 26, pp. 2283–2294, Nov. 2015.

[107] J. O. Davies, "INSPECTION OF PIPES USING LOW FREQUENCY FOCUSED GUIDED WAVES," p. 206.

[108] J. Li and J. L. Rose, "Excitation and propagation of non-axisymmetric guided waves in a hollow cylinder," *The Journal of the Acoustical Society of America*, vol. 109, pp. 457–464, Feb. 2001.

[109] J. J. Ditri and J. L. Rose, "Excitation of guided elastic wave modes in hollow cylinders by applied surface tractions," *Journal of Applied Physics*, vol. 72, pp. 2589–2597, Oct. 1992.

[110] J. Li and J. L. Rose, "Angular-profile tuning of guided waves in hollow cylinders using a circumferential phased array," *IEEE Transactions on Ultrasonics, Ferroelectrics, and Frequency Control*, vol. 49, pp. 1720–1729, Dec. 2002.

[111] T. Hayashi, K. Kawashima, Z. Sun, and J. L. Rose, "Analysis of flexural mode focusing by a semianalytical finite element method," *The Journal of the Acoustical Society of America*, vol. 113, pp. 1241–1248, Mar. 2003.

[112] L. Zhang, W. Luo, and J. L. Rose, "Ultrasonic Guided Wave Focusing Beyond Welds in a Pipeline," in *AIP Conference Proceedings*, vol. 820, (Brunswick, Maine (USA)), pp. 877–884, AIP, 2006.

[113] J. Mu and J. L. Rose, "Long Range Ultrasonic Guided Wave Focusing in Pipe Using a Phased-Array System," in *AIP Conference Proceedings*, vol. 894, (Portland, Oregon (USA)), pp. 158–162, AIP, 2007.

[114] J. Mu, L. Zhang, and J. L. Rose, "Defect circumferential sizing by using long range ultrasonic guided wave focusing techniques in pipe," *Nondestructive Testing and Evaluation*, vol. 22, pp. 239–253, Dec. 2007.

[115] J. Wu, Z. Tang, F. Lü, and K. Yang, "Ultrasonic guided wave focusing in waveguides with constant irregular cross-sections," *Ultrasonics*, vol. 89, pp. 1–12, Sept. 2018.

[116] P. Wilcox, M. Lowe, and P. Cawley, "The effect of dispersion on long-range inspection using ultrasonic guided waves," *NDT & E International*, vol. 34, pp. 1–9, Jan. 2001.

[117] D. N. Alleyne, T. P. Pialucha, and P. Cawley, "A signal regeneration technique for long-range propagation of dispersive Lamb waves," *Ultrasonics*, vol. 31, pp. 201–204, May 1993.

[118] T. Yamasaki, S. Tamai, and M. Hirao, "Optimum excitation signal for long-range inspection of steel wires by longitudinal waves," *NDT & E International*, vol. 34, pp. 207–212, Apr. 2001.

[119] P. Wilcox, "A rapid signal processing technique to remove the effect of dispersion from guided wave signals," *IEEE Transactions on Ultrasonics, Ferroelectrics, and Frequency Control*, vol. 50, pp. 419–427, Apr. 2003.

[120] K. Xu, D. Ta, and W. Wang, "Dispersion compensation and modes separation of ultrasonic guided waves in long cortical bone," *Bone*, vol. 47, Oct. 2010.

[121] S. Dion, L. P. Riel, and M. Brouillette, "Shock Wave Generation through Constructive Wave Amplification," in *28th International Symposium on Shock Waves* (K. Kontis, ed.), pp. 827–832, Berlin, Heidelberg: Springer Berlin Heidelberg, 2012.

[122] M. Brouillette and S. Dion, "Mechanical wave generator and method thereof."

[123] L. Zeng, J. Lin, Y. Lei, and H. Xie, "Waveform design for high-resolution damage detection using lamb waves," *IEEE Transactions on Ultrasonics, Ferroelectrics, and Frequency Control*, vol. 60, pp. 1025–1029, May 2013.

[124] L. Zeng, J. Lin, L. Huang, and M. Zhao, "Amplitude Dispersion Compensation for Damage Detection Using Ultrasonic Guided Waves," *Sensors (Basel, Switzerland)*, vol. 16, Sept. 2016.

[125] M. K. Yucel, S. Fateri, M. Legg, A. Wilkinson, V. Kappatos, C. Selcuk, and T.-H. Gan, "Pulse-compression based iterative time-of-flight extraction of dispersed Ultrasonic Guided Waves," in *2015 IEEE 13th International Conference on Industrial Informatics (INDIN)*, (Cambridge, United Kingdom), pp. 809–815, IEEE, July 2015.

[126] J. Lin, H. Jiadong, L. Zeng, and L. Zhi, "Excitation Waveform Design for Lamb Wave Pulse Compression," *IEEE Transactions on Ultrasonics, Ferroelectrics, and Frequency Control*, vol. 63, pp. 165–177, Nov. 2015.

[127] T. P. Waters, "A chirp excitation for focussing flexural waves," *Journal of Sound and Vibration*, vol. 439, pp. 113–128, Jan. 2019.

[128] V. van Gemmeren, B. Zybach, and J. Dual, "Focusing Flexural Waves in Beams for Precisely Controlled Dynamic Fracture," *Physical Review Applied*, vol. 10, p. 044021, Oct. 2018.

[129] M. Fink, "Time reversal of ultrasonic fields. I. Basic principles," *IEEE Transactions on Ultrasonics, Ferroelectrics, and Frequency Control*, vol. 39, pp. 555–566, Sept. 1992.

[130] F. Wu, J.-L. Thomas, and M. Fink, "Time reversal of ultrasonic fields. Il. Experimental results," *IEEE Transactions on Ultrasonics, Ferroelectrics, and Frequency Control*, vol. 39, pp. 567–578, Sept. 1992.

[131] A. Derode, P. Roux, and M. Fink, "Robust Acoustic Time Reversal with High-Order Multiple Scattering," *Physical Review Letters*, vol. 75, pp. 4206–4209, Dec. 1995.

[132] A. Derode, A. Tourin, and M. Fink, "Ultrasonic pulse compression with one-bit time reversal through multiple scattering," *Journal of Applied Physics*, vol. 85, pp. 6343–6352, May 1999.

[133] G. Montaldo, P. Roux, A. Derode, C. Negreira, and M. Fink, "Generation of very high pressure pulses with 1-bit time reversal in a solid waveguide," *The Journal of the Acoustical Society of America*, vol. 110, pp. 2849–2857, Dec. 2001.

[134] G. Montaldo, P. Roux, A. Derode, C. Negreira, and M. Fink, "Ultrasound shock wave generator with one-bit time reversal in a dispersive medium, application to lithotripsy," *Applied Physics Letters*, vol. 80, pp. 897–899, Feb. 2002.

[135] C. Draeger, J.-C. Aime, and M. Fink, "One-channel time-reversal in chaotic cavities: Experimental results," *The Journal of the Acoustical Society of America*, vol. 105, pp. 618–625, Jan. 1999.

[136] C. Draeger, J.-C. Aime, and M. Fink, "One-channel time-reversal in chaotic cavities: Experimental results," *The Journal of the Acoustical Society of America*, vol. 105, pp. 618–625, Jan. 1999.

[137] N. Quieffin, S. Catheline, R. K. Ing, and M. Fink, "Real-time focusing using an ultrasonic one channel time-reversal mirror coupled to a solid cavity," *The Journal of the Acoustical Society of America*, vol. 115, pp. 1955–1960, May 2004.

[138] L. Fillinger, A. Sutin, and A. Sarvazyan, "Time Reversal Acoustic focusing with random reverberator," *The Journal of the Acoustical Society of America*, vol. 123, pp. 3338–3338, May 2008.

[139] A. P. Sarvazyan, L. Fillinger, and L. R. Gavrilov, "A comparative study of systems used for dynamic focusing of ultrasound," *Acoustical Physics*, vol. 55, pp. 630–637, Oct. 2009.

[140] B. ARNAL, M. Pernot, M. Fink, and M. Tanter, "Tunable time-reversal cavity for high-pressure ultrasonic pulses generation: A tradeoff between transmission and time compression," *Applied Physics Letters*, vol. 101, no. 6, p. 064104, 2012.

[141] M. L. Willardson, B. E. Anderson, S. M. Young, M. H. Denison, and B. D. Patchett, "Time reversal focusing of high amplitude sound in a reverberation chamber," *The Journal of the Acoustical Society of America*, vol. 143, pp. 696–705, Feb. 2018.

[142] C. Heaton, B. E. Anderson, and S. M. Young, "Time reversal focusing of elastic waves in plates for an educational demonstration," *The Journal of the Acoustical Society of America*, vol. 141, pp. 1084–1092, Feb. 2017.

[143] F. Deng, C. He, B. Wu, D. O. Thompson, and D. E. Chimenti, "TIME REVERSAL METHOD FOR PIPE INSPECTION WITH GUIDED WAVE," in *AIP Conference Proceedings*, vol. 975, (Golden (Colorado)), pp. 131–138, AIP, 2008.

[144] N. O'Donoughue, J. Harley, J. Moura, Y. Jin, I. Oppenheim, Y. Ying, J. States, J. Garrett, and L. Soibelman, "Single Antenna Time Reversal of Guided Waves in Pipelines," in *Proceedings of Meetings on Acoustics*, vol. 6, pp. 065001–065011, May 2009.

[145] Y. Ying, J. Harley, J. H. G. Jr, Y. Jin, J. M. F. Moura, N. O'Donoughue, I. J. Oppenheim, and L. Soibelman, "Time reversal for damage detection in pipes," in *Sensors and Smart Structures Technologies for Civil, Mechanical, and Aerospace Systems 2010*, vol. 7647, p. 76473S, International Society for Optics and Photonics, Apr. 2010.

[146] N. O'Donoughue, J. Harley, and J. M. Moura, "Time reversal beamforming of guided waves in pipes with a single defect," in *2010 Conference Record of the Forty Fourth Asilomar Conference on Signals, Systems and Computers*, pp. 1786–1790, Nov. 2010.

[147] Q. Ji, Q. Kong, and G. Song, "Study on energy focusing synthesis on pipe using time reversal technique," in *Proceedings of the 11th IEEE International Conference on Networking, Sensing and Control*, (Miami, FL, USA), pp. 625–630, IEEE, Apr. 2014.

[148] S. W. Rienstra, "Fundamentals of Duct Acoustics," p. 52.

[149] J. H. Ginsberg, *Acoustics-A Textbook for Engineers and Physicists*. Cham: Springer International Publishing, 2018.

[150] M. Abramowitz and I. A. Stegun, *Handbook of Mathematical Functions With Formulas, Graphs, and Mathematical Tables*. United States. Government Printing Office., Dec. 1972.

[151] G. Kirchhoff, "Über den Einfluss der Wärmeleitung in einem Gase auf die Schallbewegung," *Annalen der Physik*, vol. 210, no. 6, pp. 177–193, 1868.

[152] M. Bruneau, PH. Herzog, J. Kergomard, and J. Polack, "General formulation of the dispersion equation in bounded visco-thermal fluid, and application to some simple geometries," *Wave Motion*, vol. 11, pp. 441–451, Sept. 1989.

[153] E. Dokumaci, "On the effect of viscosity and thermal conductivity on sound propagation in ducts: A re-visit to the classical theory with extensions for higher order modes and presence of mean flow," *Journal of Sound and Vibration*, vol. 333, pp. 5583–5599, Oct. 2014.

[154] C. Weng and F. Bake, "An Analytical Model for Boundary Layer Attenuation of Acoustic Modes in Rigid Circular Ducts With Uniform Flow," *Acta Acustica united with Acustica*, vol. 102, pp. 1138–1141, Nov. 2016.

[155] R. E. Beatty, "Boundary Layer Attenuation of Higher Order Modes in Rectangular and Circular Tubes," *The Journal of the Acoustical Society of America*, vol. 22, pp. 850–854, Nov. 1950.

[156] A. M. Bruneau, M. Bruneau, PH. Herzog, and J. Kergomard, "Boundary layer attenuation of higher order modes in waveguides," *Journal of Sound and Vibration*, vol. 119, pp. 15–27, Nov. 1987.

[157] *Acoustics Module User's Guide*. COMSOL.

[158] "Acdecom - acoustic mode decomposition in flow ducts — acdecom 20/06/12 documentation." https://acdecom.readthedocs.io/en/latest/.

[159] W. Wagner and A. Pruß, "The IAPWS Formulation 1995 for the Thermodynamic Properties of Ordinary Water Substance for General and Scientific Use," *Journal of Physical and Chemical Reference Data*, vol. 31, pp. 387–535, June 2002.

[160] Augustus R. Okoyenta, H. Wu, and X. Liu, "A Short Survey on Green's Function for Acoustic Problems,"

[161] G. J. Bennett, C. J. O'Reilly, H. Liu, and U. Tapken, "Modelling Multi-Modal Sound Transmission From Point Sources in Ducts With Flow Using a Wave-Based Method," p. 9, 2009.

[162] F. J. Fahy, *Sound and Structural Vibration: Radiation, Transmission and Response*. Elsevier, Jan. 2007.

[163] B. Fraeijs de Veubeke, "Influence of internal damping on aircraft resonance," 1959.

[164] R. Badry, M. Kotti, and P. Ramancharla, "A Comparative Study of Absorbing Layer Methods to Model Radiating Boundary Conditions for the Wave Propagation in Infinite Medium," *International Journal of Engineering & Technology*, vol. 7, pp. 25–29, Dec. 2018.

[165] M. Drozdz, "Efficient Numerical Modelling of Absorbing Regions for Boundaries Of Guided Waves Problems," in *AIP Conference Proceedings*, vol. 820, (Brunswick, Maine (USA)), pp. 126–133, AIP, 2006.

[166] M. Pastor, M. Binda, and T. Harčarik, "Modal Assurance Criterion," *Procedia Engineering*, vol. 48, pp. 543–548, 2012.

[167] H. Kitamura, K. Takahashi, and D. Kanamaru, "Inhibitory Effect of Ultrasonic Waves on the Larval Settlement of the Barnacle, Balanus amphitrite in the Laboratory.," *Marine fouling*, vol. 12, no. 1, pp. 9–13, 1995.

[168] D. M. Donskoy, M. Ludyanskiy, and D. A. Wright, "Effects of sound and ultrasound on Zebra Mussels.," *The Journal of the Acoustical Society of America*, vol. 99, pp. 2577–2603, Apr. 1996.

[169] H. Kusku, M. Yigit, S. Yilmaz, Ü. Yigit, and S. Ergün, "Biofouling Control of Invasive Zebra Mussel(*Dreissena polymorpha*) Using Acoustic Energy," *Polish Journal of Environmental Studies*, vol. 31, pp. 3173–3179, June 2022.

[170] C. Choi, A. Scardino, P. Dylejko, L. Fletcher, and R. Juniper, "The effect of vibration frequency and amplitude on biofouling deterrence," *Biofouling*, vol. 29, pp. 195–202, Feb. 2013.

[171] D. W. S. edited by Thomas F. Nalepa, *Zebra Mussels : Biology, Impacts, and Control*. Boca Raton, Fla.: Lewis Publishers, [1993] ©1993.

[172] M. Dal Borgo, M. Ghandchi Tehrani, and S. J. Elliott, "Identification and analysis of nonlinear dynamics of inertial actuators," *Mechanical Systems and Signal Processing*, vol. 115, pp. 338–360, Jan. 2019.

[173] S. Camperi, M. Ghanchi-Tehrani, M. Zilletti, and S. J. Elliott, "Active vibration control of an inertial actuator subject to broadband excitation," *Journal of Physics: Conference Series*, vol. 744, p. 012038, Sept. 2016.

[174] J. R. Hutchinson and S. A. El-Azhari, "Vibrations of Free Hollow Circular Cylinders," *Journal of Applied Mechanics*, vol. 53, pp. 641–646, Sept. 1986.

[175] N. Stephen, "The second spectrum of Timoshenko beam theory—Further assessment," *Journal of Sound and Vibration*, vol. 292, pp. 372–389, Apr. 2006.

[176] D. S. Houghton and D. J. Johns, "A Comparison of the Characteristic Equations in the Theory of Circular Cylindrical Shells," *Aeronautical Quarterly*, vol. 12, pp. 228–236, Aug. 1961.

[177] K. Shirakawa, "Characteristic roots of cylindrical shells based on an improved theory," *Ingenieur-Archiv*, vol. 56, no. 3, pp. 201–208, 1986.

[178] D. G. Karczub, "Expressions for direct evaluation of wave number in cylindrical shell vibration studies using the Flügge equations of motion," *The Journal of the Acoustical Society of America*, vol. 119, pp. 3553–3557, June 2006.

Appendices

A. One Dimensional Theories

There are a number of approximate one-dimensional theories that are adequate to describe different motions of a pipe in the low frequency limit. In this appendix the equations of motion for these theories are presented and a harmonic wave solutions are applied to obtain the dispersion relations. In all cases, x refers to the axial coordinate of the waveguide and t denotes time.

A.1 Equations of Motion

A.1.1 Fluid Plane Wave

Assuming a fluid-filled pipe with rigid walls, there is a single propagating acoustic wave in the low frequency limit. This wave has a form identical to an acoustic plane wave in free space with the equation of motion given by

$$\frac{\partial^2 p}{\partial x^2} = \left(\frac{\rho_f}{B}\right) \frac{\partial^2 p}{\partial t^2}. \tag{A.1}$$

where p is the acoustic pressure, and B and ρ_f are the bulk modulus and density of the fluid respectively. The phase and group velocities are equal and given by $\sqrt{B/\rho_f}$.

The pressure is uniform over cross-section of the waveguide. As the acoustic wavelength approaches the pipe diameter with increasing frequency, higher-order modes will begin to propagate with a non-uniform pressure distribution. These are captured by higher-order duct theory using the Helmholtz equation. Still, the preceding equation still holds for the plane wave at all frequencies as long as the duct wall is rigid. Where the wall has finite impedance, the plane wave assumption no longer valid and instead there is a quasi-plane wave which is dispersive. Furthermore the plane/quasi-plane wave disappears entirely in the case of a duct with perfectly compliant walls.

A.1.2 Simple Rod

The quasi-longitudinal waves which travel a pipe wall can be described in the simplest case by elementary rod theory, governed by the 1D wave equation. By balancing forces using Hooke's Law for a uniform bar, the equation of motion is given in terms of the axial displacement u

$$\frac{\partial^2 u}{\partial x^2} = \left(\frac{\rho_s}{E}\right) \frac{\partial^2 u}{\partial t^2}. \tag{A.2}$$

where E and ρ_s are the Young's modulus and density of the material respectively. The phase and group velocities are given by $\sqrt{E/\rho_s}$, often known as the bar or rod velocity, approximately $5\text{km}\,\text{s}^{-1}$ in steel. This theory assumes there is no inertia to the transverse motion of the rod which arises out of the Poission coupling between the axial and transverse strains. The assumption breaks down at higher frequencies, which can be addressed in a rod, for example, with Love rod theory or yet higher-order theories. In a pipe, the behaviour will sharply diverge from a rod near the ring frequency, and the waves can no longer be adequately described with the rod assumption.

A.1.3 Simple Shaft

The derivation of the elementary theory for torsional waves is essentially the rotational counterpart of the simple rod theory. Using θ as the angular displacement variable, a similar governing equation of motion is given:

$$\frac{\partial^2\theta}{\partial x^2} = \left(\frac{\rho_s}{G}\right)\frac{\partial^2\theta}{\partial t^2}. \tag{A.3}$$

Another non-dispersive wave results with the phase and group velocities equal to the shear wavespeed in the material $\sqrt{G/\rho_s}$, approximately $3\text{km}\,\text{s}^{-1}$. The fundamental torsional wave in solid cylindrical waveguides is well described by this simple theory at all frequencies.

A.1.4 Euler-Bernoulli Beam

The Euler-Bernoulli beam theory (EBBT) provides the first elementary theory with a dispersive governing equation, derived by considering the bending moments about a section of the beam. It describes the transverse displacement w with

$$\frac{\partial^2}{\partial x^2}\left(EI\frac{\partial^2 w}{\partial x^2}\right) = -\rho A\frac{\partial^2 w}{\partial t^2} \tag{A.4}$$

Where ρA is the product of density and cross-sectional area, and gives the linear mass density of the beam. This term allows extra mass to be added, a simple way of incorporating basic fluid coupling in the model. If there is no internal fluid then $\rho = \rho_s$. The second moment of area, I, is given for a hollow cylinder of mean radius a and wall thickness h by

$$a^3h\pi + \frac{1}{4}ah^3\pi \tag{A.5}$$

This theory neglects shear deformation and rotary inertia of the cross-section and thus is only accurate at low frequencies.

A.1.5 Timoshenko Beam

Timoshenko beam theory addresses the deficiencies of the EBBT by including the effects of shear deformation and rotary inertia. The governing equations are typically derived considering the transverse displacement and slope of the beam, resulting in two coupled partial differential equations. These two second order

PDEs can be reduced into a single governing equation of fourth order, which is given only in terms of the transverse deflection

$$\frac{EI}{\rho A}\frac{\partial^4 w}{\partial x^4} - \frac{I}{A}\left(1+\frac{E}{G\kappa}\right)\frac{\partial^4 w}{\partial x^2 \partial t^2} + \frac{\partial w^2}{\partial t^2} + \frac{\rho I}{GA\kappa}\frac{\partial^4 w}{\partial t^4} = 0. \tag{A.6}$$

Here all variables have the same meaning as in the EBBT. The coefficient κ is required to bring the theory into agreement with results obtained from the exact equations of linear elasticity. For a thin hollow cylinder κ can be found with [174].

$$\kappa = \frac{2(1+\nu)}{4+3\nu}. \tag{A.7}$$

Which is approximately 0.53.

For solid beams, Timoshenko beam theory is accurate to high frequency and has good agreement with solutions obtained from exact equations of linear elasticity. In the case of the fundamental bending wave in a pipe, both beam theories will become inaccurate at and above the ring frequency. It is worth noting that the Timoshenko dispersion relation involves wavenumber terms of the fourth order. This implies that there are two branches (or 'modes') described by this theory. The meaning of this second branch is unclear however, and it is usually ignored [175].

A.2 Dispersion Relations

Considering the harmonic wave solution with arbitrary amplitude C,

$$Ce^{i(kx-\omega t)} \tag{A.8}$$

the governing equations yield the dispersion relation, between the wavenumber k and angular frequency ω. These are presented in Table A.1. From this the phase and group velocities can be obtained from the definitions $c_p = \omega/k$ and $c_g = d\omega/dk$.

Theory	Dispersion Relation $F(\omega, k) = 0$
Plane Acoustic	$\omega - k\sqrt{\frac{B}{\rho_f}} = 0$
Elementary Rod	$\omega - k\sqrt{\frac{E}{\rho_s}} = 0$
Elementary Shaft	$\omega - k\sqrt{\frac{G}{\rho_s}} = 0$
Euler-Bernoulli Beam	$k^2 - \omega\sqrt{\frac{\rho_s A}{EI}} = 0$
Timoshenko Beam	$(G\kappa Ak^2 - \rho A\omega^2)(GA\kappa + EIk^2 - \rho I\omega^2) - G^2\kappa^2 A^2 k^2 = 0$

Table A.1: Dispersion relations obtained from the one-dimensional theories

The phase velocity curves are shown in Figure A.1 for each of the elementary theories. Fluid loading is not included in the beam theories.. The ring frequency

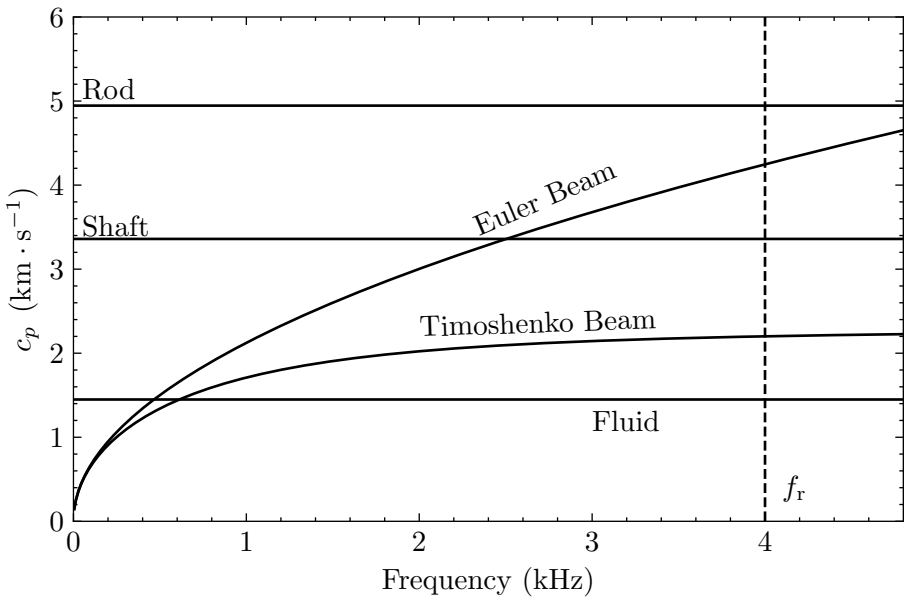

Figure A.1: Phase velocities for elementary theories describing a 20 cm radius steel water pipe.

f_{ring} denotes when the pipe begins to resonate radially as a ring. None of the modes, with exception of the torsional, are expected to hold beyond the ring frequency, where the pipe behaviour will rapidly diverge from any of these one-dimensional analogues.

B. Thin Cylindrical Shell Theory

There are a variety of different thin shell theories, most comprehensively covered by Leissa [42], each of which make slightly different kinematic assumptions in their respective derivation. All rely on the fundamental assumption that the through-thickness displacement field in the shell wall is linear, an assumption which is justified for a cylinder with a very small wall thickness to radius ratio [46]. The most rudimentary shell theory is the Love membrane theory, which entirely neglects bending effects. In this appendix the Flügge shell equations are presented, since they are generally considered to be the most accurate [176, 177]. The coordinate system used is shown in Figure B.1. The variables u, v, and w denote the displacement of the middle surface in the axial, tangential and radial directions.

B.1 In Vacuo

The governing equations of motion in the absence of forcing are given by

$$\begin{aligned}
&\left[a^2\frac{\partial^2}{\partial x^2}+\frac{(1-\nu)}{2}\frac{\partial^2}{\partial\theta^2}-\rho\frac{(1-\nu^2)}{E}a^2\frac{\partial^2}{\partial t^2}+\beta^2\frac{(1-\nu)}{2}\frac{\partial^2}{\partial\theta^2}\right]u\\
&+\left[\frac{(1+\nu)}{2}a\frac{\partial^2}{\partial x\partial\theta}\right]v+\left[\frac{\nu a\partial}{\partial x}-\beta^2a^3\frac{\partial^3}{\partial x^3}+\beta^2\frac{(1-\nu)}{2}a\frac{\partial^3}{\partial x\partial\theta^2}\right]w=0,\\
&\left[a\frac{(1+\nu)}{2}\frac{\partial^2}{\partial x\partial\theta}\right]u+\left[\frac{(1-\nu)}{2}a^2\frac{\partial^2}{\partial x^2}+\frac{\partial^2}{\partial\theta^2}-\rho\frac{(1-\nu^2)}{E}a^2\frac{\partial^2}{\partial t^2}\right.\\
&\left.+\beta^2 3a^2\frac{(1-\nu)}{2}\frac{\partial^2}{\partial x^2}\right]v+\left[\frac{\partial}{\partial\theta}-\beta^2\frac{(3-\nu)}{2}a^2\frac{\partial^3}{\partial x^2\partial t}\right]w=0\\
&\left[a\frac{\nu\partial}{\partial x}-\beta^2a^3\frac{\partial^3}{\partial x^3}+\beta^2\frac{(1-\nu)}{2}a\frac{\partial^3}{\partial x\partial\theta^2}\right]u+\left[\frac{\partial}{\partial\theta}-\beta^2\frac{(3-\nu)}{2}a^2\frac{\partial^3}{\partial x^2\partial\theta}\right]v\\
&+\left[1+\beta^2\nabla^4+\rho\frac{(1-\nu^2)}{E}a^2\frac{\partial^2}{\partial t^2}+\beta^2\left(1+2\frac{\partial^2}{\partial\theta^2}\right)\right]w=0
\end{aligned}\tag{B.1}$$

where non-dimensional thickness parameter has been introduced $\beta^2 = h^2/12a^2$. The solutions for a given mode are assumed to be of the form

$$u = U\cos(n\phi)e^{i\left(k_z z-\omega t+\frac{\pi}{2}\right)} \quad \text{or} \quad iUe^{i(k_z z+n\phi-\omega t)} \tag{B.2}$$

$$v = V\sin(n\phi)e^{i(k_z z-\omega t)} \quad \text{or} \quad iVe^{i(k_z z+n\phi-\omega t)} \tag{B.3}$$

$$w = W\cos(n\phi)e^{i(k_z z-\omega t)} \quad \text{or} \quad We^{i(k_z z+n\phi-\omega t)}. \tag{B.4}$$

The first set of solutions describe a standing circumferential wave and a propagating axial wave. The second set also satisfy B.1 and describe a wave propagating

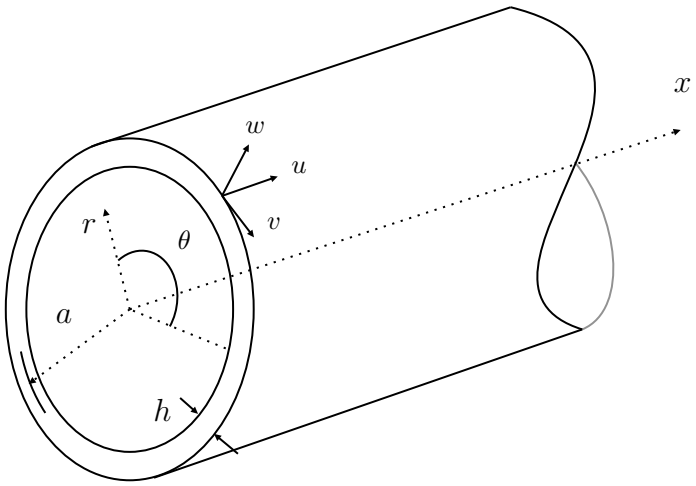

Figure B.1: Cylindrical coordinate system for the thin shell with displacement components shown.

both circumferentially and axially, with wavefronts which spiral down the pipe in a helical pattern.

The variable n is known as the circumferential mode order. Axisymmetric modes have $n = 0$ and these include all longitudinal modes and the fundamental torsional mode. The $n = 1$ modes include (but are not limited to) the beam bending mode, described in the low frequency limit by the beam theories covered in appendix A.

After substitution of the solutions into B.1, the governing equations are now represented conveniently in matrix form

$$\begin{bmatrix} L_{11} & L_{12} & L_{13} \\ L_{21} & L_{22} & L_{23} \\ L_{31} & L_{32} & L_{33} \end{bmatrix} \begin{bmatrix} U \\ V \\ W \end{bmatrix} = \begin{bmatrix} 0 \\ 0 \\ 0 \end{bmatrix} \tag{B.5}$$

$$L_{11} = (k_z a)^2 + [(1-\nu)/2]\,(1+\beta^2)\,n^2 - \Omega^2, \quad L_{12} = n[(1+\nu)/2]k_z a$$

$$L_{13} = -i\left\{(\nu - [(1-\nu)/2]\beta^2 n^2)\,(k_z a) + \beta^2 (k_z a)^3\right\} \quad L_{21} = L_{12},$$

$$L_{22} = [(1-\nu)/2]\,(1+3\beta^2)\,(k_z a)^2 + n^2 - \Omega^2, \quad L_{23} = -i\left\{n + n[(3-\nu)/2]\beta^2 (k_z a)^2\right\},$$

$$L_{31} = -L_{13}, \quad L_{32} = -L_{23},$$

$$L_{33} = [1 + \beta^2\,(1-2n^2)] + \beta^2\,((k_z a)^4 + 2n^2 (k_z a)^2 + n^4) - \Omega^2.$$

Here the non-dimensional frequency $\Omega = \omega a / c_l$, is used, which is helpful in simplifying the mathematics. Once solved, all quantities may be readily converted back to their dimensional form.

The non-trivial solutions to equation B.5 are found when the determinant of the coefficient matrix is equal to zero, giving the characteristic equation of the system. The dispersion relation is then given by an 8th order polynomial in either k_z or Ω, yielding four unique, generally complex branches for each circumferential mode order. This can either be solved analytically [178] or numerically.

B.2 Fluid Coupled

An internal fluid can be included in the theory by matching the radial velocity of the shell wall with the acoustic velocity of the internal fluid, as has been investigated in some detail by Fuller and Fahy [49]. The frequency equation is now expressed as

$$\begin{bmatrix} L_{11} & L_{12} & L_{13} \\ L_{21} & L_{22} & L_{23} \\ L_{31} & L_{32} & L_{33} - FL \end{bmatrix} \begin{bmatrix} U \\ V \\ W \end{bmatrix} = \begin{bmatrix} 0 \\ 0 \\ 0 \end{bmatrix} \tag{B.6}$$

The system is seen to differ in equation B.5 by the inclusion of a fluid loading term

$$FL = \Omega^2 \left(\frac{\rho_f}{\rho_s}\right) \left(\frac{1}{k_r h}\right) \frac{J_n(k_r a)}{J_n'(k_r a)} \tag{B.7}$$

where ρ_f and ρ_s are the densities of the fluid and structure respectively. The radial wavenumber k_r is given by

$$k_r = \pm\sqrt{\Omega^2 \left(\frac{c_l}{c_f}\right)^2 - (k_z a)^2}. \tag{B.8}$$

The inclusion of the Bessel functions in the characteristic equation add significant complexity when solving for the dispersion relation, and analytical solutions are no longer possible. Instead, a root-finding algorithm is typically used to solve the frequency equation.

C. The WFE Method

This appendix provides a basic description of the Wave Finite Element method. The formulation presented here was implemented in Python, and the code has since been packaged and is freely available to use (see Section C.4).

C.1 Formulation of Eigenproblem

Consider a short segment of a waveguide of axial length Δ meshed with finite elements, illustrated in Figure C.1. As is required by the WFE method, the degrees of freedom on the left and right faces of the segment are identical. The equation of motion for this segment relates the vectors of forces and displacements over each degree of freedom

$$\mathbf{D}\tilde{\mathbf{q}} = \tilde{\mathbf{f}} \tag{C.1}$$

where $\tilde{\cdot}$ denotes the quantity is time harmonic according to $e^{j\omega t}$. The dynamic stiffness matrix (DSM) is defined at each frequency

$$\mathbf{D} = \mathbf{K} - \omega^2\mathbf{M} \tag{C.2}$$

and comprised of the mass and stiffness matrices, $\mathbf{M}$ and $\mathbf{K}$ respectively. The elements of the DSM and the corresponding forces and displacements can be partitioned according to their location on the segment's left, right or internal faces. If present, internal degrees of freedom must be condensed. The partitioned DSM is expressed in it's uncondensed form (denoted with $\cdot'$) by

$$\begin{bmatrix} \mathbf{D}'_{LL} & \mathbf{D}'_{LI} & \mathbf{D}'_{LR} \\ \mathbf{D}'_{IL} & \mathbf{D}'_{II} & \mathbf{D}'_{IR} \\ \mathbf{D}'_{RL} & \mathbf{D}'_{RI} & \mathbf{D}'_{RR} \end{bmatrix} \begin{bmatrix} \tilde{\mathbf{q}}_L \\ \tilde{\mathbf{q}}_I \\ \tilde{\mathbf{q}}_R \end{bmatrix} = \begin{bmatrix} \tilde{\mathbf{f}}_L \\ \tilde{\mathbf{f}}_I \\ \tilde{\mathbf{f}}_R \end{bmatrix} \tag{C.3}$$

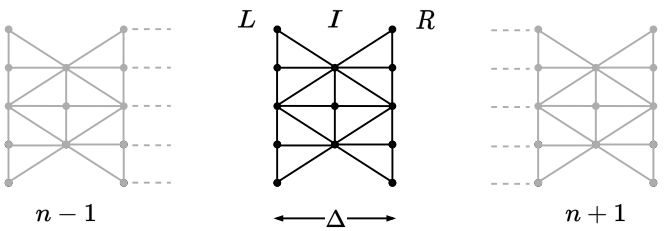

Figure C.1: Diagram of a mesh segment with nodes on the **L**eft, **R**ight and **I**nternal faces.

To eliminate the nodes internal to the segment, it is assumed that no external forces are applied at their corresponding degrees of freedom ($\tilde{\mathbf{f}}_I = 0$). The condensed DSM can then be found with the following

$$\begin{bmatrix} \mathbf{D}_{LL} & \mathbf{D}_{LR} \\ \mathbf{D}_{RL} & \mathbf{D}_{RR} \end{bmatrix} = \begin{bmatrix} \mathbf{D'}_{LL} & \mathbf{D'}_{LR} \\ \mathbf{D'}_{RL} & \mathbf{D'}_{RR} \end{bmatrix} - \begin{bmatrix} \mathbf{D'}_{LI} \\ \mathbf{D'}_{RI} \end{bmatrix} \mathbf{D'}_{II}^{-1} \begin{bmatrix} \mathbf{D'}_{IL} & \mathbf{D'}_{IR} \end{bmatrix} \tag{C.4}$$

leading to the equation of motion in terms of only the forces and displacement on the left and right face of the segment

$$\begin{bmatrix} \mathbf{D}_{LL} & \mathbf{D}_{LR} \\ \mathbf{D}_{RL} & \mathbf{D}_{RR} \end{bmatrix} \begin{bmatrix} \tilde{\mathbf{q}}_L \\ \tilde{\mathbf{q}}_R \end{bmatrix} = \begin{bmatrix} \tilde{\mathbf{f}}_L \\ \tilde{\mathbf{f}}_R \end{bmatrix}. \tag{C.5}$$

Considering the waveguide to be a periodic structure formed of repeated identical segments as in Figure C.1, the objective is to derive the transfer matrix $\mathbf{T}$ which relates the displacements and forces (sometimes known as 'state vectors') of one segment to the next, i.e

$$\mathbf{T} \begin{bmatrix} \tilde{\mathbf{q}}_L^{(n)} \\ \tilde{\mathbf{f}}_L^{(n)} \end{bmatrix} = \begin{bmatrix} \tilde{\mathbf{q}}_L^{(n+1)} \\ \tilde{\mathbf{f}}_L^{(n+1)} \end{bmatrix}. \tag{C.6}$$

To derive the transfer matrix, equation C.5 is expanded, with the first row giving

$$\begin{aligned} &\mathbf{D}_{LL}\tilde{\mathbf{q}}_L + \mathbf{D}_{LR}\tilde{\mathbf{q}}_R = \tilde{\mathbf{f}}_L \\ &\tilde{\mathbf{q}}_R = (-\mathbf{D}_{LR}^{-1}\mathbf{D}_{LL})\tilde{\mathbf{q}}_L + (\mathbf{D}_{LR}^{-1})\tilde{\mathbf{f}}_L \end{aligned}. \tag{C.7}$$

The second row, using the above expression for $\tilde{\mathbf{q}}_R$, now expands to

$$\begin{aligned} &\mathbf{D}_{RL}\tilde{\mathbf{q}}_L + \mathbf{D}_{RR}\tilde{\mathbf{q}}_R = \tilde{\mathbf{f}}_R \\ &\mathbf{D}_{RL}\tilde{\mathbf{q}}_L + \mathbf{D}_{RR}(-\mathbf{D}_{LR}^{-1}\mathbf{D}_{LL}\tilde{\mathbf{q}}_L + \mathbf{D}_{LR}^{-1}\tilde{\mathbf{f}}_L) = \tilde{\mathbf{f}}_R \\ &\tilde{\mathbf{f}}_R = (\mathbf{D}_{RL} - \mathbf{D}_{LR}^{-1}\mathbf{D}_{LL})\tilde{\mathbf{q}}_L + (\mathbf{D}_{RR}\mathbf{D}_{LR}^{-1})\tilde{\mathbf{f}}_L \end{aligned} \tag{C.8}$$

Finally, the displacements and forces are related between segments by continuity of displacement and force equilibrium

$$\begin{bmatrix} \tilde{\mathbf{q}}_L^{(n+1)} \\ \tilde{\mathbf{f}}_L^{(n+1)} \end{bmatrix} = \begin{bmatrix} \tilde{\mathbf{q}}_R^{(n)} \\ -\tilde{\mathbf{f}}_R^{(n)} \end{bmatrix}. \tag{C.9}$$

Which, upon substitution into equations C.7 and C.8 leads to the transfer matrix given by

$$\mathbf{T} = \begin{bmatrix} -\mathbf{D}_{LR}^{-1}\mathbf{D}_{LL} & \mathbf{D}_{LR}^{-1} \\ -\mathbf{D}_{RL} + \mathbf{D}_{RR}\mathbf{D}_{LR}^{-1}\mathbf{D}_{LL} & -\mathbf{D}_{RR}\mathbf{D}_{LR}^{-1} \end{bmatrix}. \tag{C.10}$$

With the transfer matrix derived, a harmonic wave propagating along the waveguide is considered. In such a case, the forces and displacements of adjacent segments are related by a constant phase factor $\lambda = \mathrm{e}^{-jk\Delta}$ such that

$$\lambda \begin{bmatrix} \tilde{\mathbf{q}}_L^{(n)} \\ \tilde{\mathbf{f}}_L^{(n)} \end{bmatrix} = \begin{bmatrix} \tilde{\mathbf{q}}_L^{(n+1)} \\ \tilde{\mathbf{f}}_L^{(n+1)} \end{bmatrix} \tag{C.11}$$

where k is the wavenumber. Equations C.6 & C.11 then lead to the well known standard eigenvalue problem

$$\mathbf{T} \begin{bmatrix} \tilde{\mathbf{q}}_L^{(n)} \\ \tilde{\mathbf{f}}_L^{(n)} \end{bmatrix} = \lambda \begin{bmatrix} \tilde{\mathbf{q}}_L^{(n)} \\ \tilde{\mathbf{f}}_L^{(n)} \end{bmatrix}. \tag{C.12}$$

C.2 Eigensolutions

With the mass and stiffness matrices extracted, partitioned, and condensed, the WFE method proceeds by calculating the eigenvalues and associated eigenvectors of the transfer matrix $\mathbf{T}$ at a specific frequency.

The solutions are given in the wave domain, where each eigenvalue λ_i is related to the wavenumber k_i and each eigenvector $\mathbf{\Phi}_i$ describes the displacement and force mode shapes

$$\mathbf{\Phi}_i = \begin{bmatrix} \tilde{\mathbf{q}} \\ \tilde{\mathbf{f}} \end{bmatrix}_i \tag{C.13}$$

If there are N degrees of freedom for both the displacements and forces in the system, the (2Nx2N) transfer matrix gives rise to 2N eigensolutions. These solutions, however, are not unique and are given in N pairs representing positive and negative-going waves, where the eigenvalue associated with a positive-going wave has its negative-going counterpart expressed as the reciprocal $\lambda^+ = 1/\lambda^-$, and correspondingly $k^+ = -k^-$.

Waves for which $|\lambda_i| < 1$ and $|\lambda_i| > 1$ are positive and negative-going respectively and both represent decaying or evanescent waves which do not propagate into the far-field or transfer energy. The case where $|\lambda_i|$ is equal to 1 (or very close within some threshold) represents propagating waves, and for these the direction is determined by evaluating the sign of the power flow, calculated with the eigenvectors $\mathrm{Re}(j\omega \mathbf{\Phi}_f^H \mathbf{\Phi}_q)$, where $\cdot^H$ denotes the complex conjugate transpose.

C.3 Forced Response

In the wave domain, the response at any point in the waveguide is constructed with a superposition of the free wave solutions scaled by their corresponding amplitudes. Given an external force vector $\mathbf{f}_e$, the directly excited wave amplitudes are calculated by considering continuity of displacement and force equilibrium [ref]. At a single frequency, these are calculated with

$$\begin{bmatrix} \mathbf{a}^+ \\ \mathbf{a}^- \end{bmatrix} = \begin{bmatrix} \mathbf{\Phi}_q^+ & -\mathbf{\Phi}_q^- \\ \mathbf{\Phi}_f^+ & -\mathbf{\Phi}_f^- \end{bmatrix}^{-1} \begin{bmatrix} 0 \\ \mathbf{f}_e \end{bmatrix} \tag{C.14}$$

where, for example, $\mathbf{\Phi}_q^+$ is the NxN matrix containing the set of positive-going displacement eigenvectors $\mathbf{\Phi}_q^+ = [\tilde{\mathbf{q}}_1^+, \tilde{\mathbf{q}}_2^+, ..., \tilde{\mathbf{q}}_N^+]$. The resulting column vectors $\mathbf{a}^\pm$ then contain the directly excited amplitudes for each of the N modes. With this, the displacements and forces can be calculated for each mode individually, or summed to find the total response, in this case at the input with

$$\begin{bmatrix} \tilde{\mathbf{q}} \\ \tilde{\mathbf{f}} \end{bmatrix} = \begin{bmatrix} \mathbf{\Phi}_q^+ & \mathbf{\Phi}_q^- \\ \mathbf{\Phi}_f^+ & \mathbf{\Phi}_f^- \end{bmatrix} \begin{bmatrix} \mathbf{a}^+ \\ \mathbf{a}^- \end{bmatrix} \tag{C.15}$$

The forcing is applied to a single face of the mesh, located at the axial coordinate x_e. For an infinite waveguide with no reflections, it is sufficient to consider only the positive-going waves to predict the response at any $x > x_e$. For simplicity, the excitation point is set as $x_e = 0$. The wave amplitudes at any distance x are calculated with

$$\mathbf{b}^+ = \boldsymbol{\tau}(x)\mathbf{a}^+ \tag{C.16}$$

where $\boldsymbol{\tau}$ is the propagation matrix defined as

$$\boldsymbol{\tau}(x) = \begin{bmatrix} e^{-jk_1^+ x} & & & \\ & e^{-jk_2^+ x} & & \\ & & \ddots & \\ & & & e^{-jk_N^+ x} \end{bmatrix} \tag{C.17}$$

The response at any aribitrary distance from the source can now be calculated with

$$\begin{bmatrix} \tilde{\mathbf{q}} \\ \tilde{\mathbf{f}} \end{bmatrix} = \begin{bmatrix} \boldsymbol{\Phi}_q^+ & \boldsymbol{\Phi}_q^- \\ \boldsymbol{\Phi}_f^+ & \boldsymbol{\Phi}_f^- \end{bmatrix} \mathbf{b}^+ \tag{C.18}$$

C.4 Python Implementation Code

The method as presented above was implemented in Python and used throughout this thesis for predicting wave propagation in fluid-filled pipes. The code is available for others to use and can be accessed with the following links:

- **Repository**
- **Documentation**

The package implements the WFE method in its basic transfer matrix form and thus may encounter numerical issues when applied to more complicated geometries. More robust formulations of the eigenproblem and forced response can be readily integrated into the code if needed.